CONTINUOUS AND DIGITAL APPROACHES TO MANIPULATION AND DETECTION OF ANALYTES ON MICROFLUIDIC DEVICES

by

Lili Mats

A thesis submitted to the Department of Chemistry

in conformity with the requirements

for the degree of Doctor of Philosophy

Queen's University

Kingston, Ontario, Canada

(April, 2016)

Abstract

Microfluidic devices are extremely popular in the area of analytical research as they reduce sample input requirements, have low operational cost, fast analysis time, high separation resolution and low detection limits. A multitude of analytical techniques has been adapted to the microdevice format, including pre-treatment, separation, and detection. Depending on how the fluid is addressed and manipulated, microfluidics can be sub-divided into the "continuous-flow" and digital microfluidics (DMF) approaches. This thesis aims to demonstrate the versatility of microfluidic field of research, where a number of actuation approaches, fabrication methods and materials, on-chip operations and applications were explored.

"Continuous-flow" microfluidics allows manipulating the bulk of the sample through the narrow channels under the applied force. Fabrication techniques unique to thermoplastics were utilized to fabricate a "continuous-flow" device capable of separating small drugs and large biological molecules, where a microstructured fibre served as an electrospray ionization mass spectrometry (ESI-MS) emitter.

Interest in DMF, where discrete droplets are addressed and manipulated independently, has grown rapidly due to the versatility that arises from non-linear control of fluids. The most common approaches to droplet manipulation are based on either electrowetting-on-dielectric (EWOD) or magnetic interactions. EWOD devices were fabricated with standard photolithography procedures, where coatings with varying degrees of hydrophobicity were explored for EWOD actuation – natural leaf surface, Teflon® AF, and a series of fluorinated silica nanoparticle-based materials.

The magnetic actuation approach is based on the interaction of an external magnetic field and magnetically susceptible material inside the droplet, which can be transported over a low-friction surface. Natural superhydrophobic leaf, hydrophobic Teflon, and a commercial superhydrophobic surface were compared for their suitability for the particle-based magnetic actuation. We demonstrated

that a commercial coating has excellent compatibility with magnetic actuation, where high actuation speed was reproducibly achieved.

We also developed a novel "particle-free" method of magnetic manipulation, where instead of magnetic particles, droplets contained paramagnetic salts with high magnetic susceptibilities were used. Droplets of five paramagnetic salts were efficiently actuated over the commercial superhydrophobic surface, where salts with higher magnetic susceptibility required lower concentrations and achieved higher actuation speed. The "particle-free" approach was used with online fluorescence detection of an anti-cancer drug.

Co-Authorship

The work presented in this thesis was mainly designed, analyzed and presented by the author in the Department of Chemistry of Queen's University under the supervision of Dr. Richard Oleschuk. Part of this work was co-authored by Dr. Graham Gibson, who assisted in conducting experiments and writing the manuscripts for Chapters 2 and 4. Dr. Guojun Liu, Ashley Bramwell and John Dupont assisted in conducting experiments for a part of Chapter 3. Work of the undergraduate students Rachel Young and Mandy Jor was used in preparing Chapter 4. Experiments conducted by the undergraduate student Fiona Lougue were included in Chapter 5. Portions of the thesis (Chapters 2, 3 and 4) have been published in the journals below, and Chapter 5 has been submitted:

1. **L. Mats**, G. T. T. Gibson and R. D. Oleschuk, *Microfluidics and Nanofluidics*, 2013, **16**, 73-81.

2. **L. Mats**, A. Bramwell, J. Dupont, G.J. Liu and R. D. Oleschuk, *Microelectronic Engineering*, 2015, **148**, 91-97.

3. **L. Mats**, R. Young, G. T. T. Gibson and R. D. Oleschuk, *Sensors and Actuators B: Chemical*, 2015, **220**, 5-12.

Acknowledgements

Statement of Originality

I hereby certify that all of the work described within this thesis is the original work of the author. Any published (or unpublished) ideas and/or techniques from the work of others are fully acknowledged in accordance with the standard referencing practices.

(Lili Mats)

(February, 2016)

Table of Contents

List of Figures

List of Tables

List of Abbreviations

ACN	acetonitrile
APCI	atmospheric pressure chemical ionization
APPI	atmospheric pressure photoionization
aq.	aqueous
CA	contact angle
CAD	computer-aided design
CCD	charge-coupled device
CE	capillary electrophoresis
COC	cyclic olefin copolymer
DESI	desorption electrospray ionization
DMF	digital microfluidics
DOX	doxorubicin
EDX	energy-dispersive X-ray
ESI	electrospray ionization
EWOD	electrowetting-on-dielectric
FWHM	full width at half maximum
FSNP	fluorinated silica nanoparticles
GC	gas chromatography
HF	hydrofluoric acid
HPCL	high performance liquid chromatography
I.D.	inner diameter
IR	infrared
ITO	indium tin oxide
KOH	potassium hydroxide
LC	liquid chromatography
LE	leucine encephalin
LOC	lab-on-a-chip
m/z	mass to charge ratio
MALDI	matrix assisted laser desorption ionization
MeOH	methanol

MS	mass spectrometry
MSF	microstructured fibre
O.D.	outer diameter
PC	polycarbonate
PCB	printed circuit board
PDMS	polydimethylsiloxane
PMMA	poly(methyl methacrylate)
PPM	porous polymer monolith
ROA	roll-off angle
RPM	revolutions per minute
RSD	relative standard deviation
S/N	signal-to-noise ratio
SEM	scanning electron microscopy
TFT	trifluorotoluene
T_g	glass transition temperature
TIC	total ion current
UED	Ultra-Ever Dry®
UV	ultraviolet
WCA	water contact angle
XIC	extracted ion current
XPS	X-ray photoelectron spectroscopy
µTAS	micro total analysis system

Chapter 1

Introduction

1.1 Introduction - Microfluidic Approach to Chemical Analysis

1.1.1 Overview and Advantages

Microfluidic devices, also known as a lab-on-a-chip (LOC) or micro total analysis systems (µTAS), are miniaturized platforms that integrate one or several steps of chemical analysis onto a single device.[1,2] A functioning miniaturized gas chromatography (GC) analytical device was first reported in 1979, however separation efficiency and limit of detection were very poor.[3] Miniaturization technology was initially lacking fast and efficient fabrication techniques, thus the analytical microchip format did not become popular at that time. New microfabrication methods have been developed over the years, especially in the field of microelectronics, and micro-devices in chemistry experienced a rebirth in the early 1990s,[4] and have been growing exponentially since then (Fig. 1.1).[5-8]
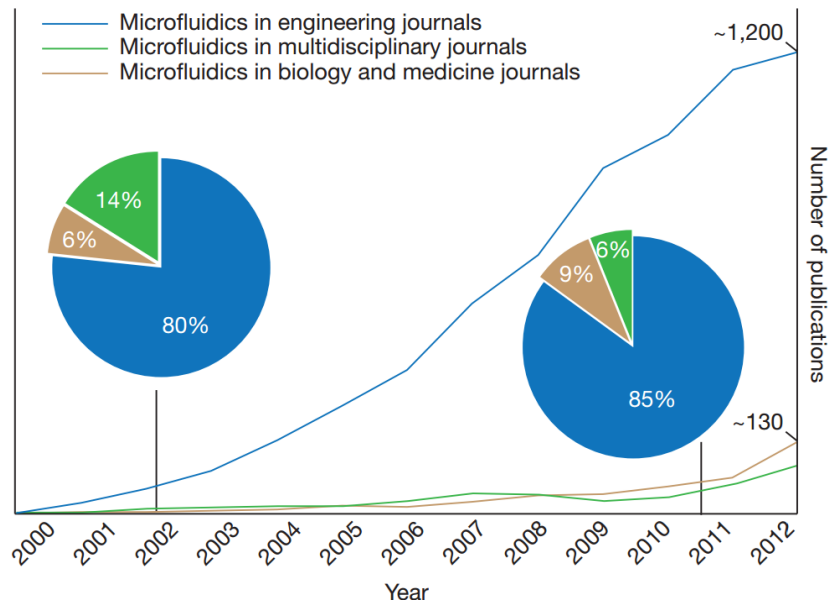
Figure 1.1: Increasing number of publications in the microfluidics area in various scientific journals.[8]

There are now several highly ranked specialized journals on the subject of microfluidics, including *Lab on a Chip*, *Journal of Microelectromechanical Systems*, *Journal of Micromechanics and Microengineering*, and *Microfluidics and Nanofluidics*. A significant number of standard chemical operations and techniques have been integrated onto a microfluidic platform, including purification/extraction, fluid manipulation, enzymatic digestion, separation (commonly based on either capillary electrophoresis (CE) or liquid chromatography (LC)), as well as a variety of detection methods, the most common of which include colourimetry, fluorescence, electrochemical detection and mass spectrometry (MS).[9] Significant research effort is being directed to the fabrication of complete systems, which consist of an integrated fluid manipulation system, including pumps and valves, where near zero dead-volume interconnections are desired.[10] The reduced size of these platforms allows one to work with smaller volumes (down to picolitres) of sample and solvent, which in turn leads to reduced cost of operation, faster analysis times, high separation resolution, and low detection limits.[5-7] Working on the microscale can also lead to other advantages, where diffusion-limited processes occur faster.[11] LOC devices can be completely isolated systems, thus making possible safer handling of toxic or otherwise dangerous materials.[12,13]

Due to a variety of newly developed materials and manufacturing techniques, microfluidic devices have become more popular as their cost has declined. Early prototypes were generally based upon costly glass or silicon substrates and labour-intensive fabrication methods.[14] With the need for a more cost-effective approach, polymers became widely popular in microfluidic research, as they offer a variety of properties suitable for most common applications and opened up the possibility of single-use devices.[15,16] Recently, paper-based devices have been receiving significant interest for point of care applications as they are widely available, inexpensive and easily fabricated.[17,18,19] Inexpensive mass production enables single-use μTAS which eliminates carry-over or contamination concerns, a sought-after trait in biological and clinical studies.[20] Microchips are also effectively used for high-throughput analysis, where multiple separation/detection steps are performed on the same device;[21]

this is an attractive feature in genomics, proteomics and drug discovery fields.[6,22-24] Depending on whether the sample is addressed in bulk or in small discrete quantities, microfluidics can be further subdivided into continuous flow or digital approaches.

1.1.2 Continuous Flow Microfluidics

Microfluidic approaches based on channels filled with analytes/reagents that are addressed in bulk are known as "continuous flow" or "in-channel" microfluidics. This approach was first envisioned as the miniaturization of already established "in-channel" techniques – separation and detection. A multitude of "microchannel" techniques have been realized on microdevices, as separation (e.g. LC and CE) and detection (e.g. optical and MS) are compatible with miniaturization. Continuous liquid flow through the narrow channels with a controllable speed and direction is the basis of continuous flow microfluidics. The external force is applied to the bulk of the fluid, moving it in a predetermined pathway. A variety of forces have been used to control and direct the flow, including pressure, electroosmotic, acoustic, magnetic, and centrifugal forces.[25,26] Pumps, valves, injectors, and power controls are required for sample manipulation, and extreme care must be taken when designing these components and connections to minimize dead volume, which becomes crucial at such small dimensions. Miniaturization of the separation column is advantageous for many applications, where smaller sample consumption and faster analysis are achievable. However, there are several technical and instrumental requirements for successful miniaturization. For example, LC separation requires channels to be able to withstand high pressures (>50 bar), therefore robust materials and high fidelity fabrication techniques are necessary. Detection methods should also be adjusted accordingly to accommodate the decrease in sample size; the reduced quantity of analyte demands increased sensitivity and lower detection limits. Some clever channel geometries and detector arrangements have been implemented in optical detection techniques.[27] Nano-electrospray ionization (ESI) has been specifically developed to accommodate the low volumetric flow rates provided by microfluidic devices.[28]

3

1.1.3 Digital Microfluidics

Independent control of small volumes of liquids is a fundamental advantage of microfluidic devices, however traditional "in-channel" microfluidics only allows addressing the bulk of the reagents/solvents, as they are confined to the microchannels. Digital microfluidics (DMF) is an alternative approach to channel-confined flow, where individual droplets can be addressed and manipulated in a precise and reproducible manner.[29,30] DMF offers advantages of the "in-channel" microfluidics, such as high processing speed, small sample size, limited waste production, precise control, and the variety of sample preparation/analysis strategies that can be implemented and multiplexed on a single device.[31-34] Furthermore, DMF devices often offer reduced fabrication complexity, as there is no need for flow control systems (e.g. pumps, injectors, valves etc.). DMF devices offer more spatial control, as the droplets are not confined to the channels. Moreover, due to the absence of channels, clogging is of no concern. DMF relies on the discrete and precise control of the individual droplets of various sizes, where droplets can be moved, split, merged and mixed and analyzed on a small platform.[35-38] There are various types of droplet manipulation mechanisms on DMF devices, including electrowetting-on-dielectric (EWOD),[32,35,39,40] dielectrophoresis,[41] acoustic wave,[42] and magnetic actuation.[43-45] The most common method for droplet actuation on DMF devices utilizes the electrowetting-on-dielectric phenomenon, where droplet movement results from the shift in the distribution of electrohydrodynamic forces due to an applied voltage.[46-48] Accurate control over droplet movement is provided through the application of voltage to a photolithographically patterned metallic electrode array (e.g. chromium or gold) coated with both a dielectric and a hydrophobic layer (Fig. 1.2).[33,35,49]
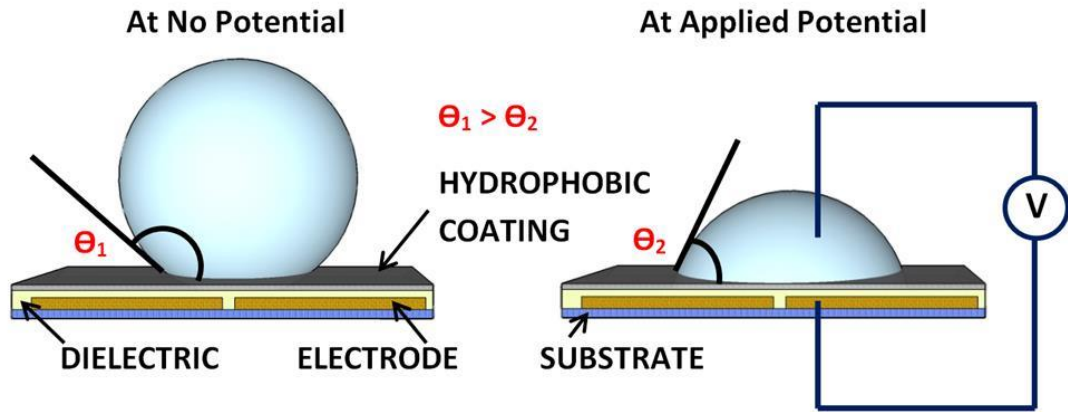
Figure 1.2: Schematic of the EWOD phenomena.

An alternative actuation method for the DMF platform is based on magnetic actuation, where a ferromagnetic fluid or an aqueous droplet containing particles with high magnetic susceptibility is manipulated by an external magnetic field.[44,50] Like EWOD devices, magnetically actuated LOCs require a hydrophobic layer to reduce the friction between the aqueous droplet and surface, enabling the droplet to slide over the surface with little resistance (Fig. 1.3).[51]
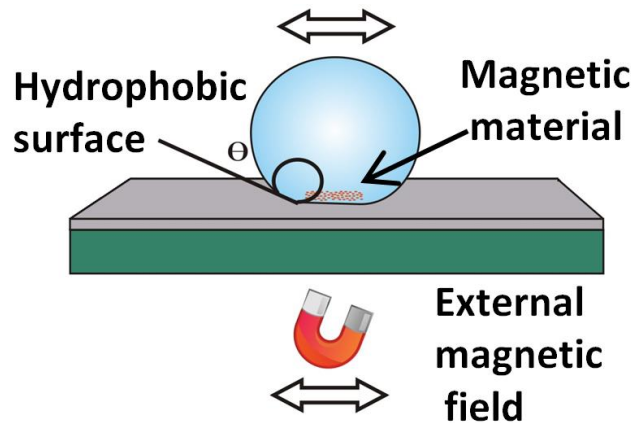
Figure 1.3: Schematic of magnetic actuation DMF approach and a typical device.

The addition of a magnetically susceptible material (e.g. superparamagnetic particles) to the droplet enables an actuation force to be easily applied to the droplet through an external magnetic field. Commercial "magnetic beads" for this purpose are based upon (super)paramagnetic particles, where an iron oxide core is surrounded by a layer of silica, which can be functionalized as desired for an intended application.[24,52,53]

5

A large portion of this thesis (Chapters 3 to 5) describes the investigation of the fundamental mechanisms of digital actuation techniques, thus a more extended introduction to each EWOD and magnetic manipulation is appropriate here. Surface properties, specifically interaction of aqueous droplets with the substrate, are of crucial importance for the actuation methods on the DMF platform, thus they are further discussed below.

1.2 Surface Interaction with Aqueous Droplets

An apparent advantage of the digital approach over "continuous flow" is the ability to precisely control a discrete quantity of the sample. The forces required to achieve that independent control are discussed further in sections 1.3 and 1.4, however the inherent properties of the surface determine the efficiency of droplet translation over the device. Surfaces with high surface friction do not allow for facile actuation, thus low-friction surfaces or coatings are extensively employed in DMF. Chapters 3, 4 and 5 examine the use of low-friction, i.e. hydrophobic and superhydrophobic, coatings in droplet based microfluidic devices using EWOD, particle-based and paramagnetic salt-based actuation. The theory behind superhydrophobicity and the fabrication methods for these surfaces are discussed below.

1.2.1 Superhydrophobic Surfaces

Surfaces can be differentiated and classified based on their wetting behavior, i.e. their interaction with aqueous droplets. Depending on the water contact angle (WCA) and the roll-off angle (ROA) between the surface and a water droplet, the surfaces can be classified as hydrophilic, hydrophobic and superhydrophobic (Fig. 1.4). Roll-off angle, also referred to as sliding or tilt angle measures the ability of the surface to retain water droplet. Large (>10°) ROA implies that the surface friction is high, i.e. surface strongly retains water; small (<10°) ROA signifies low surface friction.
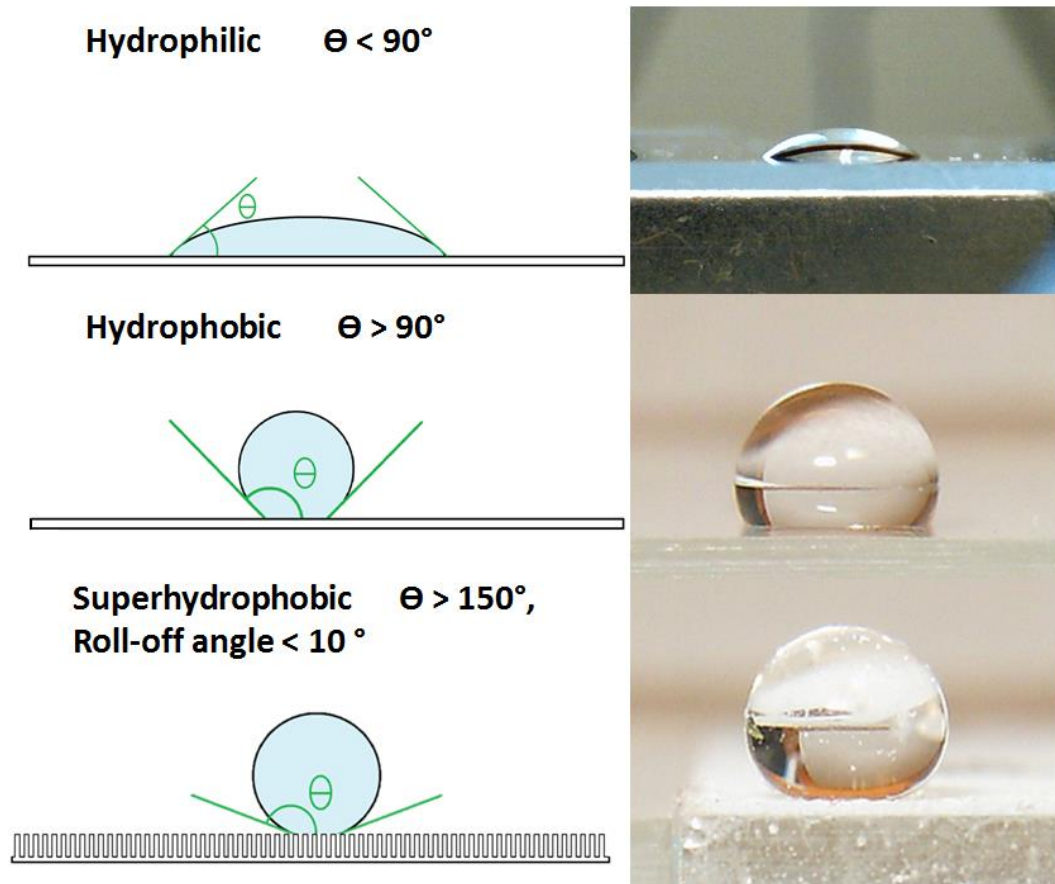
Figure 1.4: A schematic structure (left) and a photographic example (right) of an aqueous droplet on a hydrophilic, hydrophobic and superhydrophobic surface where θ is the WCA.

Hydrophilic, "water-loving", surfaces have a WCA of less than 90° where water spreads over the surface; e.g. clean glass, many metals and fused silica are hydrophilic. If the surface has a WCA above 90° but below 150° it is known as hydrophobic. Many polymer surfaces are hydrophobic; for example, Teflon® AF (θ ~ 120°) is a common commercial surface coating often applied to increase the WCA of the surface.[54] Superhydrophobic surfaces have a CA with water in excess of 150°, which is generally attributed to a combination of surface roughness and low surface energy. The superhydrophobicity is also defined by a ROA of less than 10°, where only small tilt is required to remove the droplet off the surface. It is postulated that the reason behind surface superhydrophobicity is small air pockets trapped between the droplet and the surface, which is energetically favorable as the water-surface contact is minimized.[55] Hierarchical surface structures provide micro- and nanometre

7

scale roughness and enable the entrapment of air between the surface and the droplet, thus specific surface geometries are required for the surface to be superhydrophobic (Fig. 1.5).[56,57]

$$\theta_{flat} < \theta_{nanostructure} \sim \theta_{microstructure} < \theta_{hierarchical}$$

Flat   Nanostructure   Microstructure   Hierarchical structure
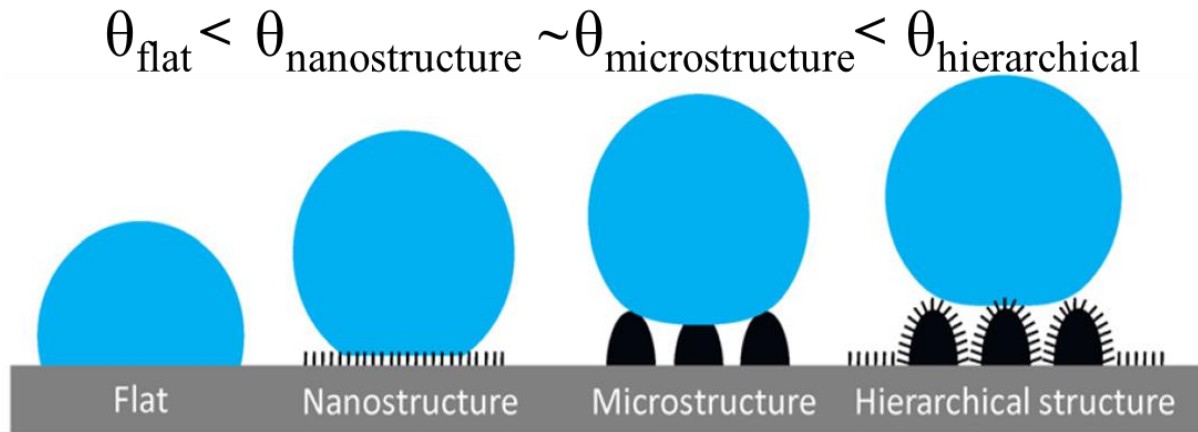
Figure 1.5: Schematic structure of the surfaces with increasing hydrophobicity, where WCA (θ) is the lowest for a flat surface and the highest for hierarchical, which exhibits the combination of both nano- and micro-structure (adapted from ref. 58).

The water droplet does not wet the hydrophobic surface between these features, leaving them filled with air and keeping contact between the liquid and surface to a minimum. This corresponds to the heterogeneous wetting regime and droplet behavior is described by the Cassie-Baxter model (Fig. 1.6).[59] The Cassie-Baxter model describes "true" superhydrophobicity, where the WCA is above 150° and the ROA of less than 10°. In a particular case, the droplet can still have a WCA of above 150°, however due to the specific microstructure regime the water becomes "trapped" in the surface, such that the ROA is greater than 10°, which is known as the Wenzel model (Fig. 1.6). As the result of this high ROA, the Wenzel model does not describe a truly superhydrophobic surface, even though the WCA exceeds 150°.

Wenzel Model   **Cassie-Baxter Model**
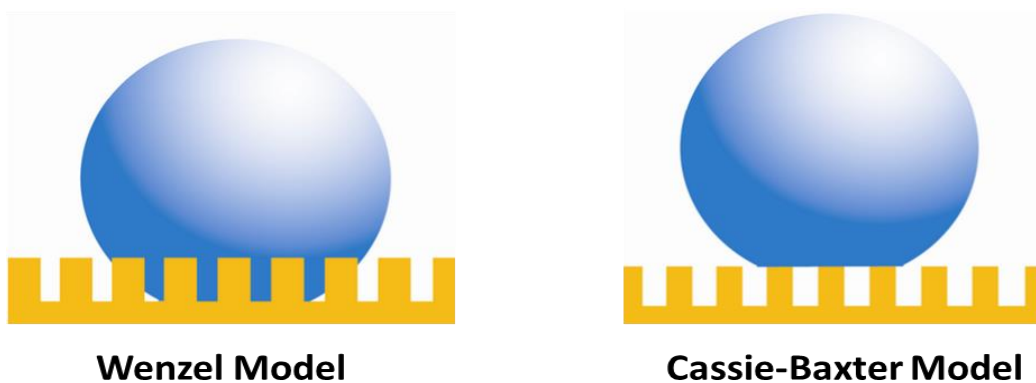
Figure 1.6: Schematic representation of wetting regimes: (left) Wenzel model, where surface features are filled with water; (right) Cassie-Baxter model, where surface features are filled with air, resulting in a true superhydrophobic surface.[60]

It is also important to mention the volume of the aqueous droplet when talking about superhydrophobicity. Ideally, a superhydrophobic surface minimizes the contact area between the surface and the droplet, where spherical shape of the droplet provides the minimum contact area possible, with the WCA approaching 180°. However, due to the gravitational effects the droplet shape is deformed, and the observed WCAs are in practice lower than 180°.[61] The larger the droplet, the greater its mass, and the more gravitational deformation it experiences. Commonly, aqueous droplets over 10 μL are not used in surface studies due to these reasons.

1.2.2 Fabrication Methods

Several plant species have evolved superhydrophobic "self-cleaning" leaves that shed water, dust and debris following a rain to maintain high photosynthetic efficiency.[62] Superhydrophobicity is achieved through a combination of leaf surface roughness and low surface energy provided by hydrophobic waxy compounds.[63,64] The roughness of the lotus leaf, for example, arises from a hierarchical structure with features on the micrometre and nanometre scales (Fig 1.7).
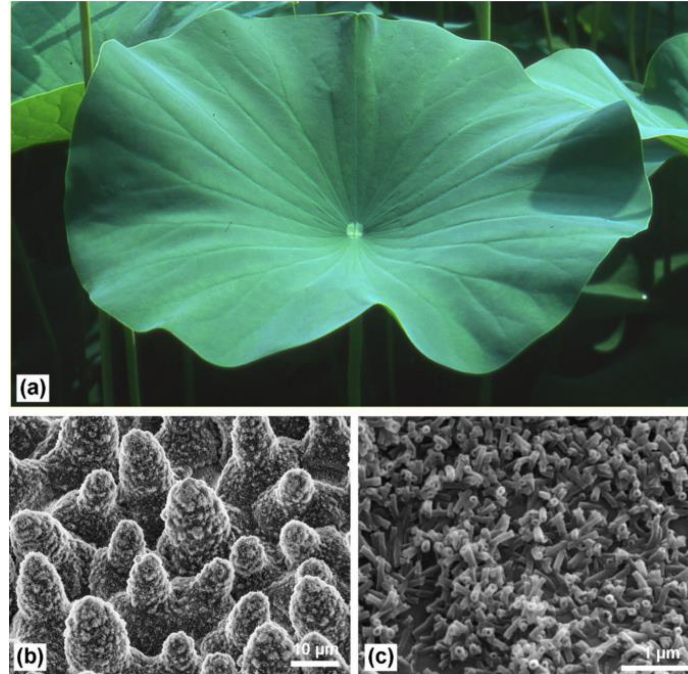
Figure 1.7: The superhydrophobic lotus leaf (a), where surface roughness on microscale (scale bar is 10 μm) (b) and nanoscale (scale bar is 1 μm) (c) is attributed to the waxy compounds.[64]

Inspired by nature, synthetic superhydrophobic materials are often referred to as "biomimetic".[65] Generally, there are two major approaches to creating a superhydrophobic surface: 1) processing a low surface energy material in order to increase its surface roughness; 2) coating a rough surface with a low energy material.[55,66]

Since the first artificial superhydrophobic surface was reported by Onda et al.[67] using fractal growth of alkylketene dimer (wax-like) to create a rough surface, many ways of synthesizing superhydrophobic surfaces have been described in the literature. Synthetic surfaces with both micrometre- and nanometre-scaled roughness have traditionally been produced in the laboratory using chemical vapour deposition, sol-gel processing, colloidal assembly, silicon nanowire growth, electrospinning, electrochemical etching and template-based techniques.[66,68-71] It is common to use inherently low-energy materials such as polymers (e.g. PDMS, PS etc.) to create surface roughness; otherwise, surfaces need to be further functionalized with nonpolar (e.g. perfluoroalkyl, long chain alkyl, etc.) substituents to produce fully superhydrophobic surfaces.[51,55,65,72] One of the common ways of creating superhydrophobic surfaces is using nanoparticles to create surface roughness on both

micro- and nano-scale. The degree of superhydrophobicity can be precisely controlled by varying the size and composition of the nanoparticle material, where other desired properties (opacity, surface chemistry, etc.) can also be introduced.[73] Nanoparticles can be easily functionalized in bulk, i.e. one-step process, thus creating rough material with low surface energy, which can be easily deposited over a desired surface.[74,75] It is also not uncommon to use a nanoparticle approach with polymer binders. This can often enhance surface adhesion of nanoparticles and even provide "self-healing" properties to the material.[71] Recently, several commercial silica nanoparticle-based coatings (e.g. NeverWet® and UltraEver Dry®) have been introduced to the market, which also include a polymer binder layer for enhanced coating stability.

Superhydrophobic surfaces possess many useful properties such as self-cleaning, anti-icing[76] and anti-fouling,[56] which have been adapted to numerous applications such as manufacturing stain-repellent textiles,[77] anti-biofouling coatings for marine applications,[58] water/ice-resistant paints,[78] etc. Superhydrophobic surfaces have been also employed as the inner coatings of closed channels to prevent non-specific adsorption, achieve high velocities and provide enhance control over droplet manipulation.[79] They are becoming very relevant in digital microfluidics applications (discussed below) as they provide reduced surface friction that facilitates droplet motion over the surface.[80-82]

1.3 Digital Microfluidics – Electrowetting-on-Dielectric

1.3.1 Electrowetting-on-Dielectric Theory

The term "electrowetting" refers to the electrically induced spreading of a droplet over a surface due to a reduction in contact angle.[83] EWOD requires an additional insulating layer of dielectric material, which serves to separate a working electrode from the liquid droplet. In this way a much higher electric field can be applied to the electrode without causing an electrical breakdown and droplet electrolysis. Higher electric field results in higher contact angle change and the effect of the applied potential can be defined by the Lippmann-Young relationship (eqn. 1.1): [46,84]

$$cos\theta_V = cos\theta_0 + \frac{1}{2}\frac{\varepsilon\varepsilon_0}{d\gamma_{LV}}V^2 \qquad\qquad \text{Equation 1.1}$$

where θ_0 is the initial contact angle of the surface, θ_V is the angle under applied potential, ε is the dielectric constant of the insulating layer, ε_0 is the dielectric constant of air, γ_{LV} is the surface tension of the liquid-vapour interface, d is the thickness of dielectric layer and V is the applied potential difference. It must be noted that the contact angle would not be further reduced past a certain applied potential, due to contact angle saturation, the phenomena which is not yet fully understood and is often attributed to material failure due to charging and electrical breakdown.[31,83-85]

The applied potential results in larger droplet spreading/contact angle change, which in turn leads to the droplet displacement due to the shift in electrohydrodynamic forces.[31,83] The analysis of force distribution is beyond the scope of this thesis, but the change is the result of charge accumulation in the electrode and the droplet, and charge separation in the dielectric layer (Fig. 1.8).
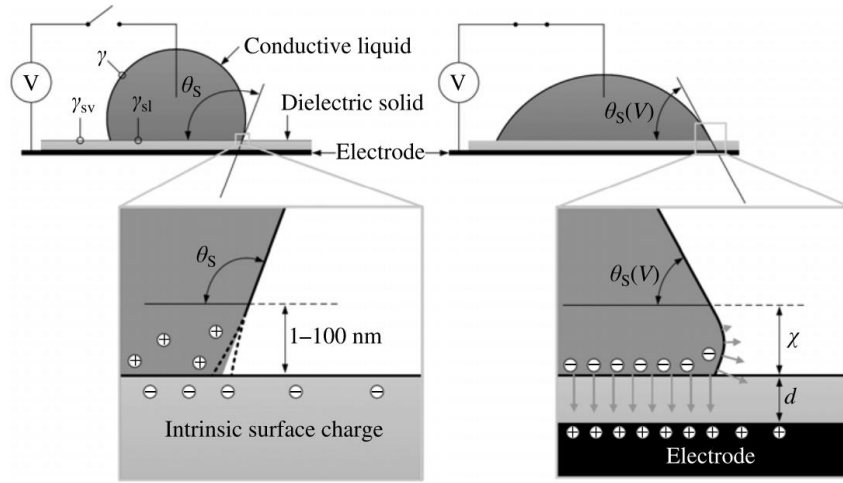
Figure 1.8: Schematic of EWOD process for a static contact angle, θ_s. Charge accumulation and separation is demonstrated in liquid-surface boundary (χ) and in the dielectric layer (d), and the change in charge distribution leads to droplet spreading, i.e. contact angle reduction ($\theta_s > \theta_s(V)$). The interfacial surface tension (γ) between solid-vapour (γ_{SV}) and solid-liquid (γ_{SL}) determine the shape of the droplet and the contact angle.[83]

1.3.2 Device Fabrication

There are several required design elements for EWOD-based devices including individual electrodes for droplet manipulation coated with a dielectric layer for charge accumulation and a

hydrophobic top layer. A surface with reduced friction is desired to facilitate droplet movement, thus highly hydrophobic surfaces are commonly employed in DMF devices.[86] The devices themselves can be "two-plate" or "open-top" systems, i.e. closed or open geometries (Fig 1.9).
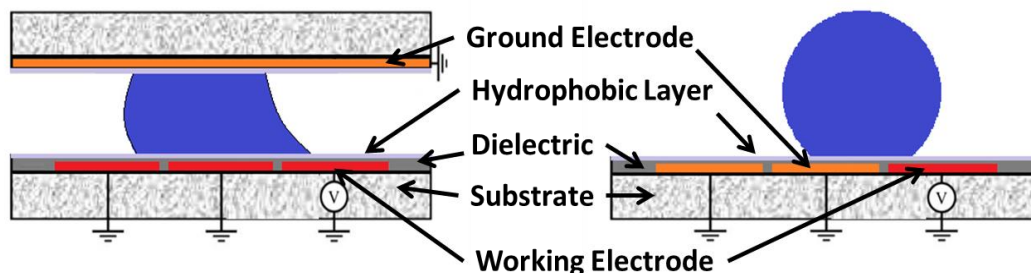
Figure 1.9: Two geometries commonly used in EWOD DMF approach: closed (left) and open (right) (adapted from ref. 36).

In the "two-plate" approach the array of working electrodes is patterned on the bottom layer, followed by a hydrophobic dielectric (or an additional hydrophobic layer), and the hydrophobic top layer serves as a counter electrode. The droplets sandwiched in between two substrates can be dispensed and split more easily; moreover they exhibit slower evaporation.[35] In the "open-top" format only the bottom plate is present, where the electrode array contains both working and counter electrodes. Open geometry does not permit droplet splitting, however it allows for faster mixing, the ability to move larger droplets, and easier access to the surface for a more facile integration with detection techniques.[29] Vertical and inverted actuation has been previously demonstrated on the "open-top" device.[87]

Electrodes (Cr, Au, Cu etc.) can be patterned on the surface using common cleanroom techniques, such as photolithography and wet-etching. The process is discussed in detail in section 1.5.1. The electrode array provides multi-functionality, and individual devices can be easily reconfigured for use in multiple applications.[29] A thin layer (micron thickness) of dielectric material can be deposited using chemical vapour deposition (parylene) or spin-coated (SU-8); other dielectric materials and deposition techniques have been reported, but are not as common.[88,89] The nature and properties of the dielectric layer often dictate the EWOD efficiency; eqn. 1.1 demonstrates that a

13

higher material dielectric constant, ε, and reduced thickness, d, result in higher contact angle change. The friction force between the surface and the leading droplet edge, i.e. de-pinning of the contact line, determines the onset of motion.[83] This friction interaction is reduced by using a hydrophobic coating, which enhances droplet motion over the surface. The most popular hydrophobic layer used is Teflon® AF, which although common, has several limitations. The WCA of Teflon is approximately 120°, which renders the surface sufficiently hydrophobic for droplet manipulation, however the surface coating is not very robust or durable, and Teflon can be removed from the surface of the device during normal use.[54,84] Teflon is also sensitive to other commonly used solvents, and has reported biofouling which limits the number of uses per device.[90,91]

Reduced surface friction is the driving mechanism behind robust EWOD actuation. The Lippmann-Young equation dictates that a higher initial WCA would require lower voltage to achieve a WCA reduction.[31] A superhydrophobic coating, which exhibits initial WCA of above 150°, should serve as an excellent substrate for electrowetting testing and EWOD actuation, although this is not entirely true. Indeed, the electrowetting process is enhanced, where the reduction of a static contact angle can be observed at significantly lower voltages. For example, Accardo et al. demonstrated WCA reduction of ~60° at 5V and almost 115° reduction at 30V for a silicon pillar-based superhydrophobic surface.[92] However, superhydrophobic surfaces are composed of highly structured roughness that promotes air entrapment (Section 1.2), where under applied voltage capillary wetting of these fine structures results in irreversible transition to Wenzel state (Fig. 1.10).[93]
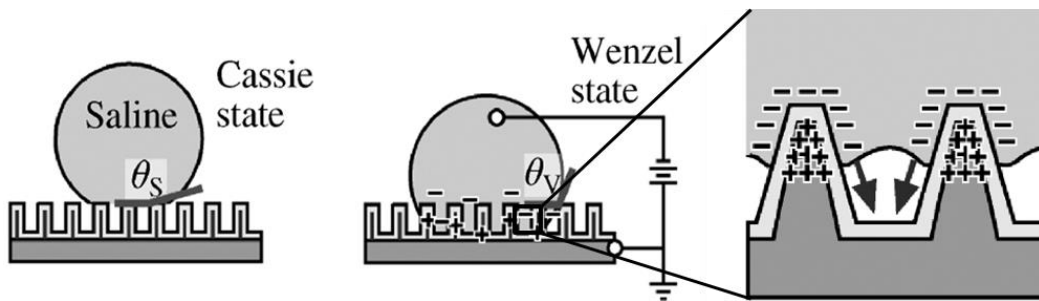
Figure 1.10: The transition of the water droplet in Cassie-Baxter state into irreversible Wenzel wetting state due to electrowetting on a superhydrophobic surface (adapted from ref. 93).

An excellent review by Heikenfeld[93] provides the reasoning behind this transition to the irreversible Wenzel state, where charge redistribution leads to this permanent change. An aqueous droplet becomes "entrapped" in the surface as it enters the Wenzel state, and droplet motion becomes impossible. This phenomena limits the applications of superhydrophobic surface to the EWOD actuation, however superhydrophobic surfaces serve as excellent substrates for an alternative digital approach – magnetic actuation.

1.4 Digital Microfluidics - Magnetic Actuation

Magnetic actuation is an alternative way of manipulating discrete droplets over hydrophobic surfaces, where magnetically susceptible materials are introduced into the droplet, in order to enable droplet actuation by an external magnetic field. This approach does not require any additional power supplies, pumps or light sources, where only a low friction surface and a reasonably strong magnet are needed. Magnetically susceptible materials (commonly superparamagnetic particles or ferrofluids) are added to the droplet so it can be controlled by a magnetic field. In order to achieve facile droplet movement, surface friction must be minimized, thus it is common to use either superhydrophobic surfaces or hydrophobic surfaces with an additional oil layer. Many devices using magnetic actuation have been reported, where basic operations such as transport, mixing and extraction have been demonstrated and evaluated.[51,94] As there is no need to create any predetermined "paths" for the droplet (channels, groves, electrode pads, etc.) the droplet has ultimate movement freedom over the entire hydrophobic surface, and droplet movement has been reported in three dimensions, including actuation of an inverted droplet.[69]

1.4.1 Magnetic Theory and Materials
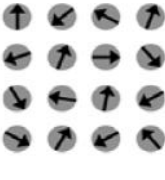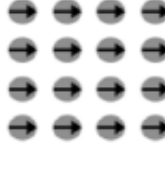
Before discussing the mechanism of magnetic actuation on DMF platform, it is important to discuss the basic concept of magnetism. A material's response to an applied magnetic field can be described by its magnetization, $\vec{M}$, which is a function of material's magnetic susceptibility, χ.[95] The magnetic susceptibility value is an inherent property of the material, determined by its atomic

magnetic momentum alignment, which describes the response of the material to external magnetic field ($\vec{H}$):

$$\vec{M} = \chi \cdot \vec{H}$$ Equation (1.2)

Magnetic properties of a material originate on an atomic level. Depending on the interaction with an external magnetic field, major types of materials can be identified as diamagnetic, ferromagnetic and paramagnetic (Table 1.1). Diamagnetic materials repel external magnetic field, where the repulsion can be highly variable depending on the material's magnetic susceptibility; most diamagnetic materials have very small negative susceptibilities ($\chi \sim -10^{-6}$). Paramagnetic materials are attracted to the external magnetic fields, as they form an induced internal magnetic field. Paramagnetic materials have a small positive magnetic susceptibility and do not retain magnetic alignment without an external magnetic field ($\chi \sim 10^{-6}-10^{-4}$). Their magnetization is proportional to the applied magnetic field, and paramagnetic materials can be controlled by an external magnet.[95] Ferromagnetic materials, including "permanent magnets", are materials that have an aligned magnetic momentum and maintain their magnetization even without an external magnetic field; they are described by large positive susceptibility ($\chi \sim 10^{4}-10^{6}$). Further subdivision of ferromagnetic materials is beyond the scope of this thesis.[96,97]

Table 1.1: Major types of magnetic materials characterized by their interaction with an external magnetic field.

Material Type	Magnetic Susceptibility (χ)	Magnetic Behaviour	Atomic Momentum
Diamagnetic	Small, negative	-No magnetic momentum in atoms -Repel permanent magnets	
Paramagnetic	Small, positive	-Randomly aligned magnetic momentum -Attracted to external magnetic field	
Ferromagnetic	Large, positive	-Parallel magnetic momentum - Maintain magnetic field	

An additional class of magnetic materials can be identified as "superparamagnetic", which can be regarded as a compromise between paramagnetic and ferromagnetic materials. Superparamagnetic materials have a large magnetic susceptibility, which arises from the coupling of many atomic spins, however they behave as a single paramagnetic atom, where magnetization is not maintained when the external magnetic field is removed.[98] This effect is observed for very small particle sizes (< 100 nm) of otherwise ferromagnetic materials (ferrite, magnetite etc.), and due to large thermal fluctuations the overall magnetic momentum is zero, however an applied external field induces parallel momenta alignment. These materials have relatively high magnetic susceptibility ($\chi \sim 10^{-2} - 10^{2}$) and are materials of choice for magnetic actuation in DMF.

1.4.2 Magnetic Particles

Depending on their size, superparamagnetic particles can be defined as "ferrofluids" or "magnetic beads". Small monodispersed superparamagnetic particles (<100 nm diameter) tend to form homogenous suspensions known as ferrofluids, which are not discussed here.[99] Large micrometre-

sized particles can maintain overall superparamagnetic properties with proper configuration (Fig. 1.11). Due to their relatively high mass (compared to particles < 100 nm), they tend to sink in droplets/solutions, but can be easily manipulated by an external magnetic field.
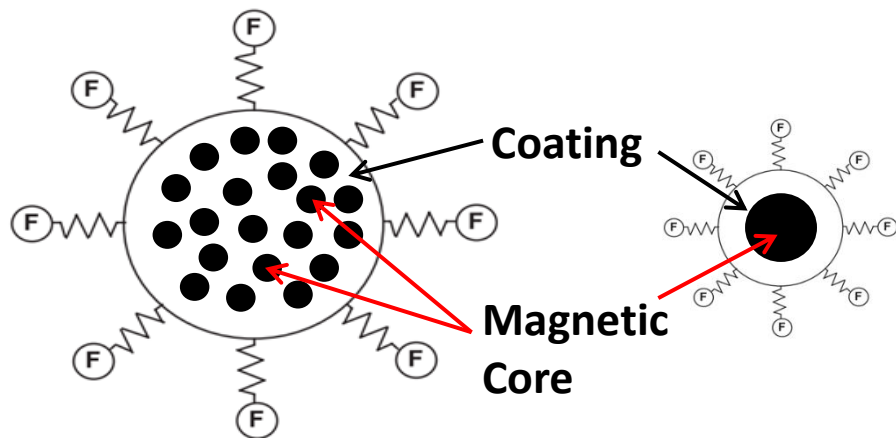
Figure 1.11: Schematic diagram of typical functionalized magnetic particles, where the core has high magnetic susceptibility. Small single-core particles (right) form suspensions known as ferrofluids, while large multi-core particles (left) are known as "magnetic beads". The surface coating (typically silica or polymer) is functionalized (F denotes possible surface functionalization) for a particular application (adapted from ref. 95).

Commercial "magnetic beads" for DMF applications are based upon large (~1 μm) superparamagnetic particles, where typically an iron oxide core (Fe_2O_3 or Fe_3O_4) is surrounded by a layer of silica, which can be functionalized as desired for a given application.[24,52,53] Standard applications utilize magnetic particles as a substrate for separation, extraction and detection, however recently they have been shown as a means of actuating discrete quantities of sample.[30,100] Surface functionalization is application dependent, but commonly the surface is modified with organic molecules to a) stabilize the nanoparticles in biological solutions;[98] b) derivatize the surface with specific groups for biological assays (protein tags, enzymes, etc.);[101] or c) modify the surface of the particles to have additional functionality (modifications for separation, fluorescent tags for detection etc.).[102] The large variety of available surface modifications and the ability to precisely control the position of magnetic particles makes them an indispensable tool in microfluidics.

1.4.3 Droplet Actuation Force Model

When an external magnetic force is applied to a droplet containing magnetic material, the initially suspended particles are pulled down to the bottom of the droplet, creating a layer of particles. As the magnet is moved horizontally, the particles form a magnetic cluster at the edge of the droplet, and as the cluster enters the droplet-air or droplet-oil boundary, the droplet shape is deformed and elongated. Depending on the force distribution, three distinct outcomes can be observed: the droplet-cluster system is translated along the motion of the magnet, the cluster is removed from the droplet, or the magnet is disengaged.[103] A simplified force distribution in the system, which determines the outcome of magnet-cluster-droplet interaction, is outlined below.

Three separate forces can be used to describe droplet-magnet interaction: magnetic force, $\overrightarrow{F_m}$, friction force, $\overrightarrow{F_f}$, and capillary force, $\overrightarrow{F_c}$.[44]

Magnetic force, which enables cluster movement following the magnet, is dependent on the magnetic material inside the droplet and the strength of the external magnetic field:

$$\overrightarrow{F_m} = V\chi\frac{B_m}{\mu_0}\nabla B_m \qquad\qquad \text{Equation 1.3}$$

where V is the volume of the magnetic cluster inside the droplet, χ is the magnetic susceptibility of the magnetic material, B_m is the strength of the applied external field, and μ_0 is permittivity of free space. It is important to note that the magnetic field is experienced as a gradient, which allows for the translational application of the force; a uniform magnetic field does not allow for actuation.[95]

Friction force, which resists droplet/cluster movement over the surface, is determined by the inherent surface properties and the size of the droplet:

$$\overrightarrow{F_f} \cong K_f R_{base}\vec{U} \qquad\qquad \text{Equation 1.4}$$

where K_f is a friction constant, R_{base} is the radius of the bottom contact area between droplet and the surface and $\vec{U}$ is the droplet velocity. As the magnet is moved underneath the substrate/surface the packet of paramagnetic particles is moved in the same direction due to magnetic force gradient, and

the droplet can be actuated over the surface when the particles remain in the droplet due to surface tension.

Capillary force determines if the magnetic bead cluster is held within the droplet as it follows the magnet (i.e. droplet containing magnetic cluster is actuated), or whether the magnetic cluster is selectively removed from the bulk of the droplet. The maximum F_c at which the cluster is contained within the droplet is determined by eqn. 1.5:

$$\overrightarrow{F_{c_{max}}} \cong 6^{\frac{1}{3}}\pi^{\frac{2}{3}}\gamma V^{\frac{1}{2}} \qquad\qquad \text{Equation 1.5}$$

where γ is the interfacial tension between the bulk of droplet and the outside medium, i.e. water-air or water-oil interfaces.

This simplified force model determines the outcome of magnet-droplet-cluster interaction, where various parameters can be varied to achieve a desired outcome. To achieve reproducible movement of the droplet-cluster system the magnetic force should be high enough, i.e. a strong magnet and high concentration of magnetic particle are required. On the other hand, from eqn. 1.5 it follows that in order to contain the magnetic cluster within the droplet, the volume of the particles must not be too high, otherwise the bead cluster is removed from the bulk of the droplet. Surface resistance must be minimized, thus superhydrophobic surfaces are often desired, as they allow for higher operational speed and larger droplet volumes (eqn. 1.4). It is also important to note that ultimately the continuous motion/extraction mechanism is determined by the size of the droplet and loading of the magnetic material in it, i.e. larger droplets and higher particle loading leads to easier extraction. The strength of the external magnetic field and the speed of magnet movement also affect the outcome of the actuation. A fundamental study by Long et al.[44] summarizes the observed operational mechanism depending on the magnet speed and the particle loading for their droplet-oil system (Fig. 1.12).
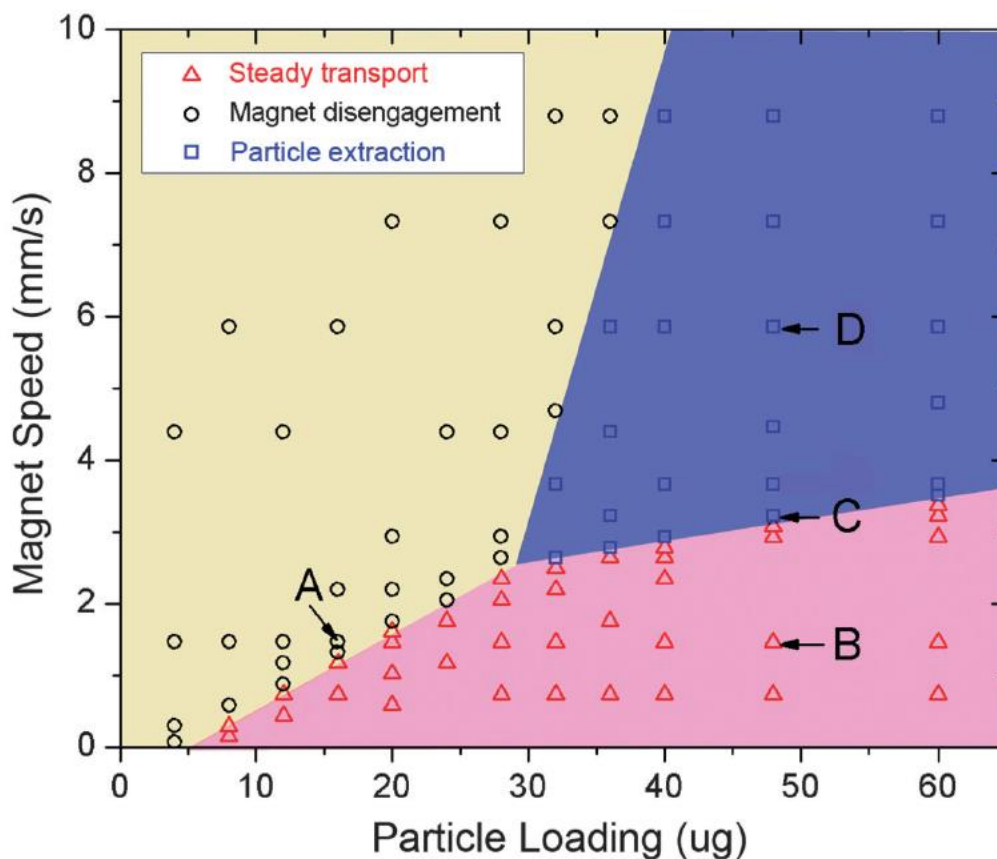
Figure 1.12: Operational diagram demonstrating possible actuation mechanisms for a 50 µL aqueous droplet with increasing concentration of magnetic beads and magnetic speed.[44]

It must be noted that if the concentration of the magnetic particles is too low and/or the magnet is moved too fast, the magnet can often disengage, leaving the particle-containing droplet behind. The disengagement is more common on surfaces with higher friction, i.e. not superhydrophobic. The addition of an oil layer to the system is a common way to enhance the sliding motion, but than in turn can make the operation more complex.[94] In order to facilitate particle cluster extraction from the bulk of the droplet it is common to modify surface topography or its energy to selectively anchor the aqueous droplet and remove the beads by magnetic force. Introducing surface topography to promote extraction usually includes creating obstacles or channels,[104] while surface energy modification creates alternating regions of hydrophilicity/hydrophobicity on the surface.[105] Surface obstacles require additional fabrication steps, which can significantly increase complexity of

21

manufacturing. The surface energy modification method is often preferred, as patterning can be done with high reproducibility and precision.

1.5 Device Fabrication

Traditionally, glass and silicon were the materials of choice for manufacturing miniaturized devices, taking its roots from the semiconductor industry.[106] Both materials can be patterned using similar techniques, have great feature reproducibility, high spatial resolution, and are compatible with most chemical applications. Glass/silicon patterning is mainly based upon photolithography, which requires microfabrication infrastructure (i.e. cleanroom) rendering the prototyping of a single microdevice an expensive and laborious process. Glass and silicon substrates are also brittle and expensive; moreover, silicon is also opaque in both the ultraviolet (UV) and visible range, which limits its use for many analytical applications. An alternative is found in polymeric materials, which are inherently more versatile, rugged, and can be patterned by less costly techniques.[107,108]

1.5.1 Glass and Silicon Photolithography

Silicon and glass remain popular substrates for microfluidic devices, and are highly utilized in DMF microchip fabrication.[109] Glass and silicon patterning for both semiconductor and microfluidic technologies is based on photolithography. Photolithography offers great versatility along with high resolution of fine features (down to tens of nanometres), however to obtain the best results it must be performed in a cleanroom environment.[110,111]

Mask design is the first step of photolithography, which defines the position of channels, electrodes or other microfeatures on the substrate. A thin metal layer (Cr, Au) is deposited onto the substrate to facilitate the adhesion of photoresist to the substrate and/or eventually serve as the actuation electrodes for the EWOD device. Photoresist is then applied by spin coating on the substrate at a desired thickness dictated by both the viscosity and spin rate during deposition. The photomask is placed onto the photoresist surface to block pre-determined areas of the photoresist layer. The mask is exposed to a light beam (typically UV) in order to transfer the mask pattern to the substrate; the

feature resolution is determined by the light source. For a typical UV source (~250 nm), features below half that wavelength are not well resolved and often merge together.[14] Alternative masking techniques (i.e. near-field, deep UV, etc.) can offer feature resolution to sub-20 nm.[112,113] Upon exposure to UV radiation, the photoresist can either harden (negative) or soften (positive) thus becoming resistant or susceptible to certain developing solvents, respectively. As the photoresist is being selectively removed, the underlying metal layer/substrate becomes exposed, which can then be etched away with an appropriate etchant as desired. For EWOD devices, the metal layer must be etched to create an array of well separated electrodes; the choice of etchant is dictated by the initial choice of metal. For the "continuous-flow" devices, channels and other features are created by directly etching away glass/silicon (*vide infra*). Fig. 1.13 summarizes the basic photolithographic scheme used to pattern a glass substrate, which includes photoresist deposition and development, and feature etching.
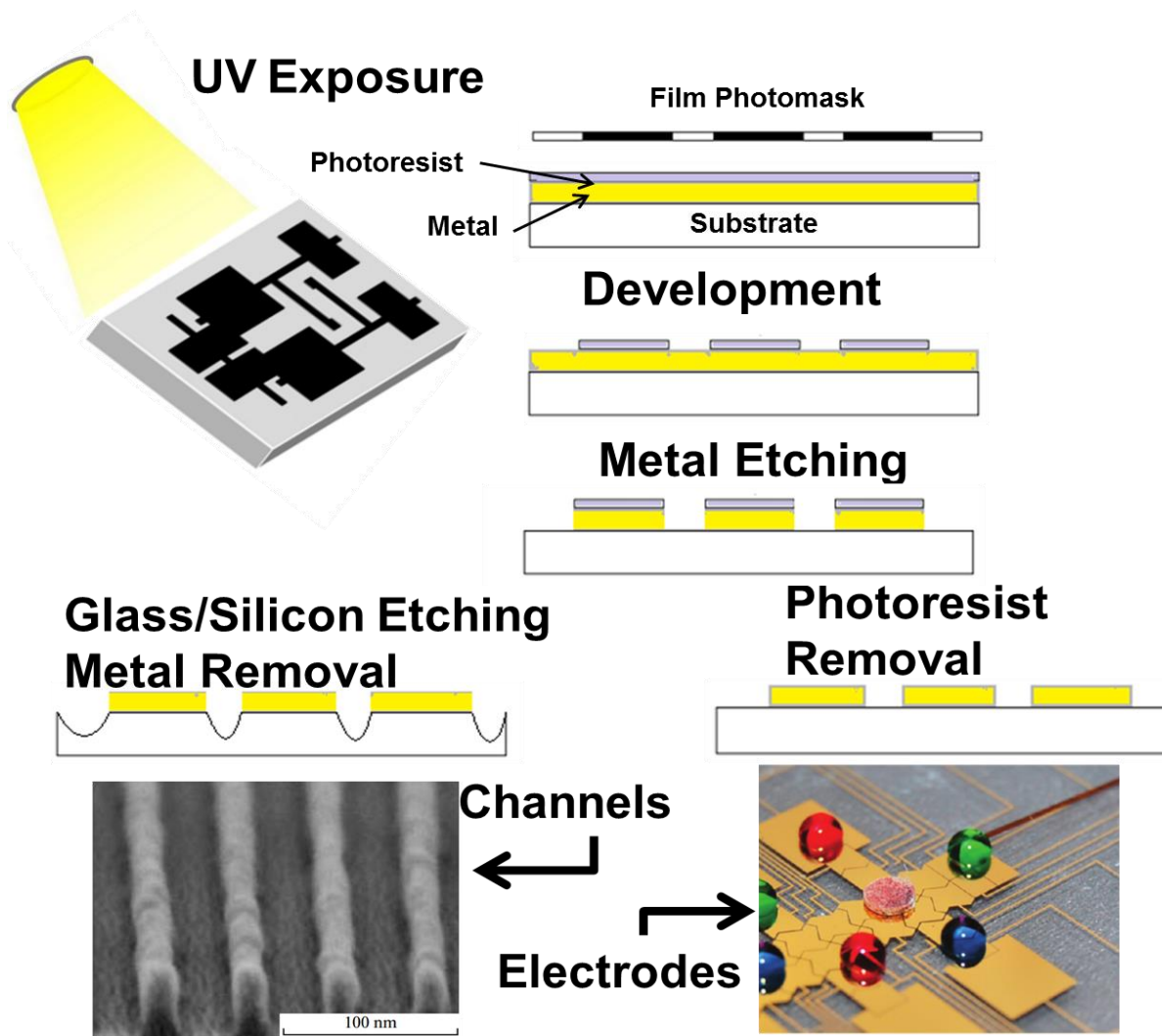
Figure 1.13: Basic steps involved in photolithography to produce etched glass grooves (left) or metal electrodes (right) (adapted from ref. 40,110,113).

For a "closed" conformation DMF EWOD device the top plate is required, however it does not have to be bound. The top plate simply rests on top of a separator, which is often comprised of multiple layers of adhesive tape; it can be removed at any time allowing for direct access to the platform during the experiment. The most common top-plate material is indium tin oxide (ITO)-coated glass, as it is both conductive and transparent. ITO-coated glass is available commercially in a variety of sizes, however for EWOD applications it is spin-coated with hydrophobic material, so the droplets have minimized friction with both top and bottom plates.

24

A micron-sized channel is often the central feature of a "continuous-flow" microfluidic device. Wet-chemical etching methods are most commonly used to fabricate these channels, where potassium hydroxide (KOH) is used for silicon and hydrofluoric acid (HF) for glass. The glass etching process is isotropic, i.e. the etch rate is equal in all directions. Isotropically etching channels often produces undercutting, making it more difficult to obtain features with high aspect ratio.[114] Conversely, silicon etches anisotropically, i.e. preferential etching in one direction over another, which can produce a non-circular channel shape, e.g. rectangular, trapezoidal or V-shaped, which limits separation efficiency during CE or LC.[115] Finally, a cover plate is bonded to the substrate to seal the device; the seal needs to be leak-free and must be able to withstand high pressures (e.g. LC separations). For most methods bonding requires high temperatures (400˚C and above) or extremely long bonding time (over 100 hours), or high voltages for anodic bonding.[116] Photolithography is a popular method of fabrication for both "continuous-flow" and DMF devices, however polymers have become widely popular in recent years.

1.5.2 Polymer Materials

The low cost and variety of materials available have driven microchip manufacturing towards polymer substrates. The material cost is considerably lower for most polymers compared to either glass or silicon. Most polymers (i.e. thin sheets) are priced in the range of 0.2-2 cents USD/cm^2 while glass can range from 15 to 40 cents USD/cm^2.[16] Polymeric materials are available with vastly different properties i.e. optical transmission, stress resistance, surface chemistry, and heat and solvent stability. Two of the most commonly used material types are elastomers and thermoplastics. Elastomers are dominated almost entirely by polydimethylsiloxane (PDMS); these materials are weakly cross-linked and can easily deform under an applied stress and reform after the stress is removed.[106] Thermoplastics are also weakly cross-linked materials, but are rigid at room temperature.[107] Elastomers and thermoplastic materials are becoming more popular, and their share in microchip manufacturing has significantly increased in the past decade as seen in Fig. 1.14.

25
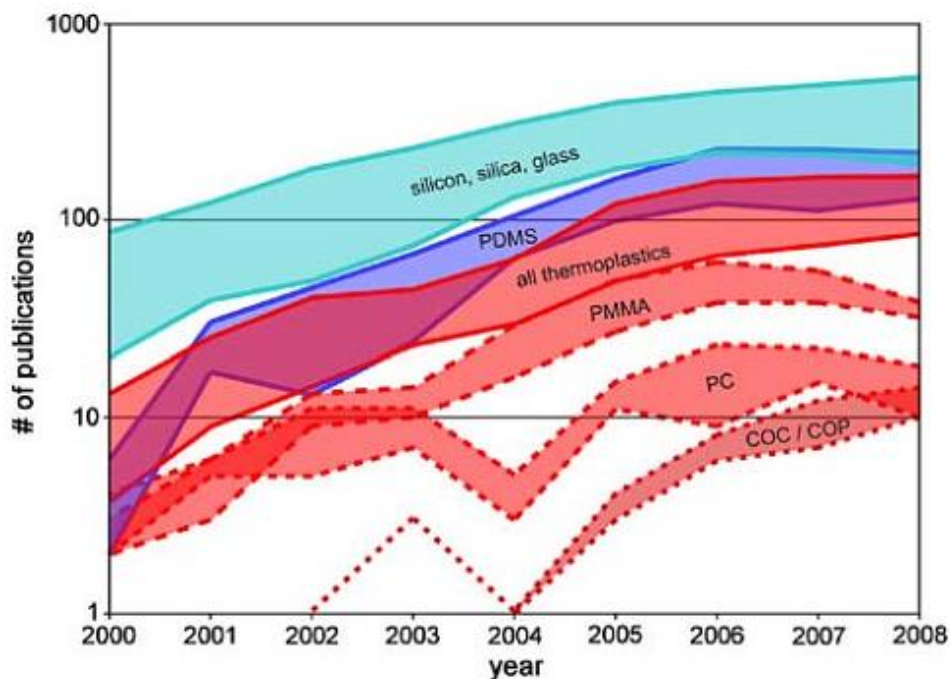
Figure 1.14: Number of publications for academic and commercial applications of microfluidics for the last decade, showing the choice of substrate material.[117]

Commonly used thermoplastics include polystyrene (PS), polyethylene (PE), polycarbonate (PC), cyclic olefin copolymer (COC) and poly(methylmethacrylate) (PMMA). The ultimate choice of material is determined by the intended application of the device. For example, spectroscopic detection methods often dictate which polymer is to be used, as most polymers have a high UV cutoff. Many polymers are also associated with significant autofluorescence, which increases the detection limit by increasing the background noise.[118] For other applications, such as liquid chromatography (LC) or capillary electrophoresis (CE), solvent stability and zeta potential of the surface are very important. For example, PC is unstable in acetonitrile, thus it is not compatible with reversed-phase LC. On the other hand, PMMA and COC are unstable in non-polar solvents, making them incompatible with normal phase LC. Zeta potentials of most polymers are much smaller than that of glass, thus CE is not as readily implemented onto polymeric devices.[119] Hydrophobicity of most polymeric materials causes problems in filling the channels with aqueous solutions, often requiring higher pressures for fluid flow or a surface treatment to be performed in order to lower hydrophobicity.[120]

26

1.5.3 Thermoplastic Fabrication

Thermoplastics are rigid materials, usually gas impermeable, which makes them appropriate for high-pressure applications. All thermoplastics have a characteristic temperature, referred to as a glass transition temperature (T_g), at which the polymer becomes soft and elastomeric, and can be deformed by applying high pressure.[117] Only pressure-affected regions are deformed, thus selective patterning can be done. Upon cooling, the substrate becomes rigid again, and as the mold is released the patterned surface is revealed. This property is commonly used by replication techniques, which require high temperature, pressure and a mold; however the surface can be also patterned directly.[121,122]

1.5.3.1 Replication

Replication refers to a process that produces multiple identical structures with complementary "negative" features, based on a single mold or a stamp with a "positive" relief. Common replication techniques used to fabricate polymeric microfluidic devices include injection molding and hot embossing. A variety of materials can serve as molds, where metals, silicon, quartz and other hard materials are the most popular. The choice of a mold is dictated by the number of desired use cycles and micro-feature resolution required. Metallic molds have superior mechanical stability and robustness, and can withstand multiple heating/cooling cycles, and thus can be used to fabricate hundreds of polymeric devices. Metallic molds are expensive, however, and more difficult to fabricate. Conversely, silicon molds can be susceptible to fracture and breakage if used with hard plastics, however exceptional resolution can be achieved with silicon molds (down to nanometres).[16,123]

1.5.3.1.1 Injection Molding

Injection molding is a very common procedure in the plastics industry, where a hot, liquid polymer is injected into a chamber containing a mold, and as the temperature is lowered the polymer takes the form of the desired shape.[107,124,125] A mold can be implemented on both the top and bottom of the chamber simultaneously, thus a "middle" layer can be easily manufactured in a single step.

27

Fabrication of an entire device often takes less than 10 minutes, and submicron features can be successfully replicated.[124] This method is, however, relatively expensive and cumbersome. Significant temperature optimization trials are required to achieve high fidelity.[107]

1.5.3.1.2 Hot Embossing

Hot embossing is often the technique of choice in microfabrication, as it is cost efficient and operates on rigid sheet substrates. A substrate can be softened and patterned under sufficient temperature and pressure. A mold with a positive relief is pressed into a polymeric substrate to create a negative pattern (channels, chambers etc.) as shown in Fig. 1.15.[108,126]
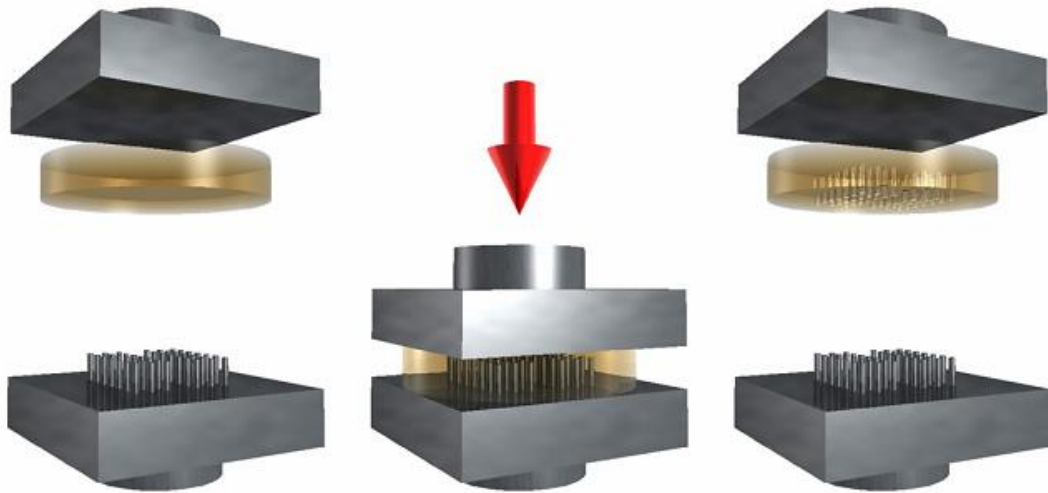
Figure 1.15: Schematic diagram of the hot embossing process using high pressure and temperature to create structures in a plastic substrate.[126]

Upon cooling, the material becomes rigid and the mold can be easily released and the patterned substrate can be further processed as desired.[107] Hot embossing is relatively inexpensive and fast; a single mold structure can be used hundreds of times.

The required temperature and pressure are determined by both the substrate material, and by the resolution of the features being reproduced. Each of the materials (PC, COC, PMMA) have a specific hardness and T_g. Thermal expansion of the material can negatively affect the feature reproducibility and induce stress, thus care must be taken to not overheat the substrate/polymer.[127]

However, with properly selected mold and embossing conditions some spectacular results have been achieved, where sub-micrometre features are accurately reproduced.[108] Another reason for the popularity of hot embossing is that a single instrument can be used as a complete station for polymeric microchip manufacturing, i.e. hot embossing can be used for both substrate patterning and bonding, where various parts of the devices are sealed together to create a complete device.

1.5.3.2 Bonding

There are a few common approaches to the bonding of thermoplastic devices where thermal, solvent, and adhesive bonding or any combination of these can be employed; each method has its benefits and drawbacks. During thermal bonding, the substrates are heated close to their T_g, and under high pressure the polymer chains in conformal contact interdiffuse and bond.[122] This is the simplest method but care must be taken when selecting the temperature and pressure conditions, as at extreme conditions the micro feature shape and resolution can be affected or channels can collapse (Fig. 1.16).
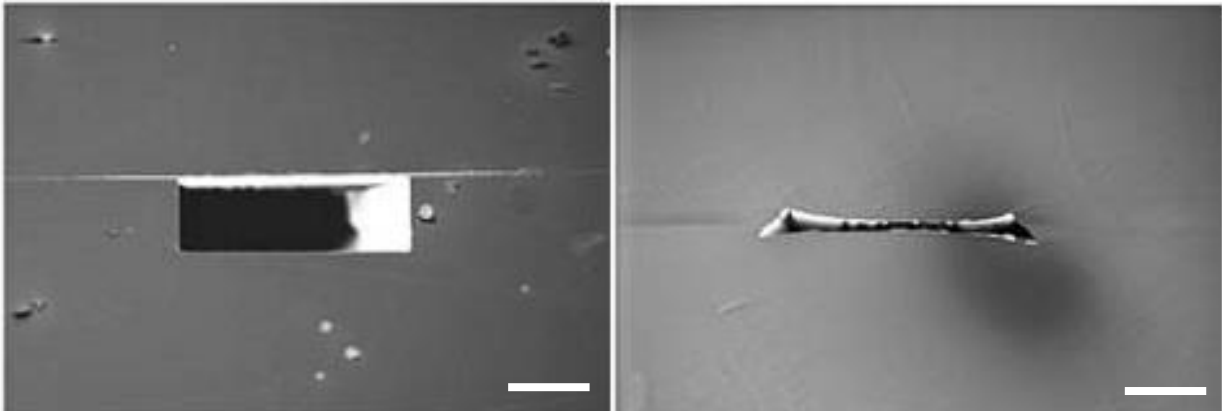
Figure 1.16: (left) Bonding under optimized conditions with no observable channel deformation; (right) extreme heat/pressure leading to channel collapse (scale bar = 200 μm).[122]

Some clever methods have been introduced to provide better bonding strength and limit the deformation of the micro-features. Some materials (notably COC) can have a variety of different T_g's associated with them, depending on the manufacturer and the grade of material.[108] In one example, the top and bottom substrates are made from the same material (COC), where different grades were employed for each plate, (e.g. T_g was lower for the top plate). During the bonding step the temperature

is selected to be lower than the T_g of the bottom plate and higher than that of the top plate.[128] Less

channel deformation is observed for this method (Fig. 1.17).
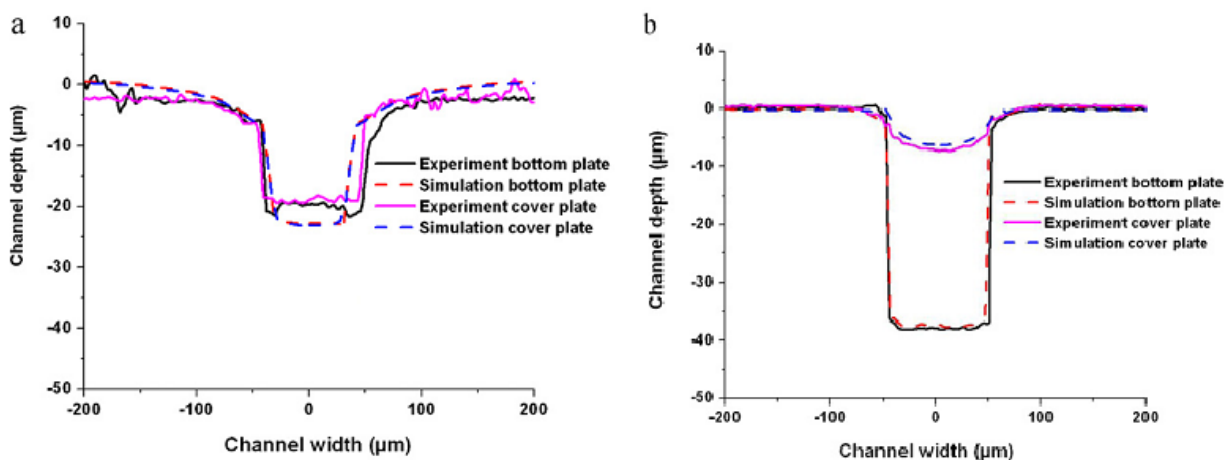
Figure 1.17: Comparison between channel profiles for thermally bonded COC microchips (experimental and numerical simulation-based design model). a) Top and bottom plates are made from the same material (T_g = 78°C) and embossed at 80°C. It can be observed that channel is completely closed; b) Top plate is as above; bottom plate has T_g of 158°C. The top plate is slightly deformed, however the channel is fully functional.[128]

In some cases, the low energy surfaces need to be activated before thermal bonding. In this

case cleaning with plasma (air, oxygen, ozone) can be performed, or exposure to UV radiation (254

nm) has been shown to improve bonding strength.[122] This surface pre-activation can also result in

shorter bonding time or lower temperature, which can be beneficial for heat-sensitive applications.

Instability of thermoplastics in certain solvents can be used to one's advantage, as the solvent-

softened surface is prone to diffusion and stronger bond formation. Solvent bonding usually provides

the strongest substrate-cover plate bonding, and can be used in bio-compatible applications as little or

no heat is required.[129] On the other hand, solvents can leach into the channels and block them, and may

even modify the surface properties of the microchip. A solvent must be carefully chosen, as if it

softens the polymer too strongly, surface deformation is inevitable (Fig. 1.18); while less effective

solvents often do not create a strong bond.[130]
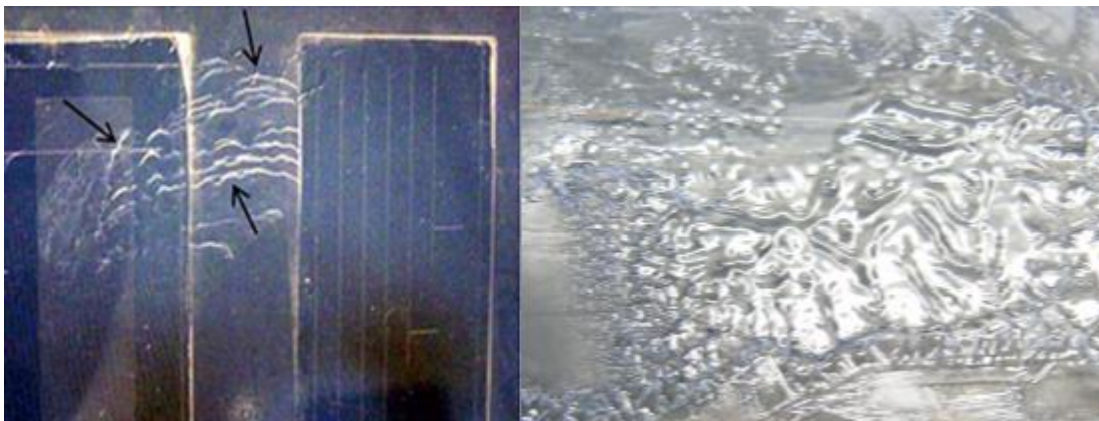
Figure 1.18: (left) Surface deformation of a polymer due to prolonged exposure to a solvent, which results in "wrinkling";[130] (right) Deformation of COC sheet as a result of the application of toluene.

It can also be hard to expose a surface sufficiently for bonding without compromising channel integrity, thus exposure to solvent vapour has become more popular recently.[108,128] Upon vapour exposure the surface is softened significantly without affecting channel shape; as there is no excess solvent, no additional drying is required.

In some cases, despite optimization, bonding can lead to channel deformation, or even complete blockage.[117,128] In these cases a sacrificial layer technique was developed, where channel shape is maintained, while bonding is performed using harsher conditions. The channel is filled with a sacrificial layer that is resistant to the solvent or heat used. After the bonding is complete, the sacrificial material is removed.[131] The sacrificial layer materials are based upon waxes, and under harsh bonding conditions the channel shape is less distorted.

Bond strength is especially important for on-chip separations, where operations are pressure demanding. For LC, another important consideration is the channel shape, which ideally should be round or semi-circular for the best separation performance. It has been previously noted that most molds are made from silicon or metal, which can produce non-circular geometry. The most common way to achieve a round channel shape is to make both top and bottom substrate containing a semi-circular channel, and then bond them with precise alignment. Dummy aligned channels were

demonstrated to improve fit precision, where channels were filled with a solid spacer during the bonding step (Fig. 1.19).[132]
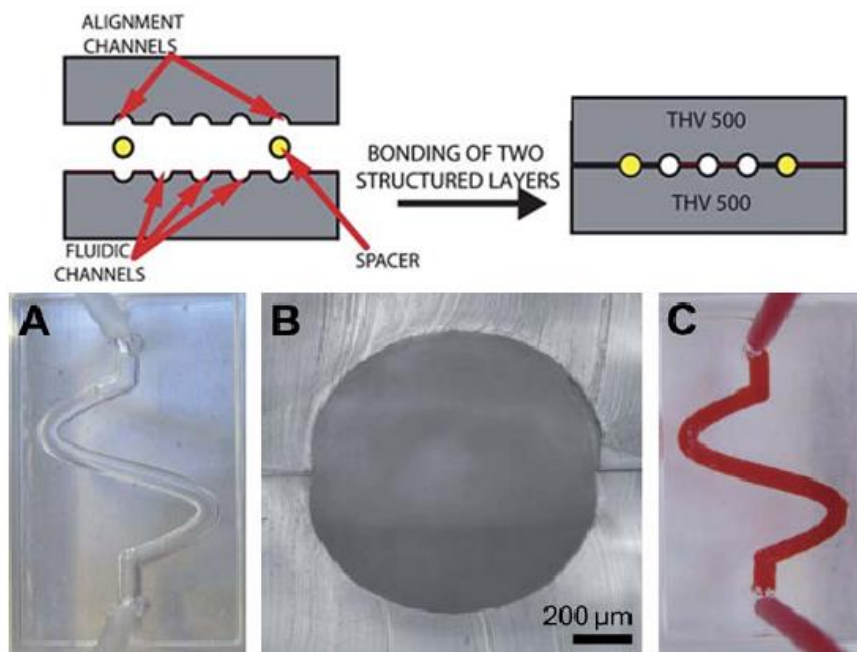
Figure 1.19: (top) Schematic set-up of using dummy channels to align semi-circular channels together; (bottom) the resulting channel cross-section that is still not perfectly circular.[132]

Another type of bonding is based on applying a thin layer of an adhesive, usually epoxy, to one or both substrates. This way is fast, does not require external heat, and is the most universal as it has least material considerations.[117] The layer must be kept thin to prevent epoxy leaching into the channels and clogging.[133] Unfortunately, many adhesives are also sensitive to commonly used solvents in LC or MS. Another drawback of using adhesives is that by applying this extra layer the surface properties of the channel are modified, which is relevant to some electrochemical applications. Bond strength is also low, limiting the devices to low pressure applications (< 10 bar).[133]

1.5.3.3 Direct Manufacturing: Micro-milling and Ablation

Thermoplastics are hard materials that are stable under mechanical stress, so they can also be directly patterned with mills and drills. Generally the desired design is first developed in a specific computer-aided design (CAD) program (e.g. Solid Edge, L-Edit, AutoCAD, etc.). An image-based design can be converted into a series of commands later performed by a computer, thus making micro-

milling fast, reproducible and not prone to human error.[134] The individual processing time for each substrate is determined by the complexity of the end-device. The drilling/milling process often leads to rough channel surfaces and the size of some fine structures is limited. Some hard plastics require multiple mills to complete a single substrate, thus the cost can be relatively high.

Ablation has been used to produce microchips from a variety of materials, including PC, PS, COC, and PMMA.[16] A variety of different wavelengths have been employed in micro-manufacturing processes, including IR, UV and x-ray. The most common source of focused radiation is a laser, which has sufficient power to heat up and ablate material from the polymeric surface. An infrared CO_2 laser is often used to ablate materials such as PC, PMMA and PDMS.[135] CO_2 lasers can create deep channels (>1 mm), but the channel profile often has a Gaussian shape due to defocusing effects.[16,136] Ablated material can be deposited onto the edges of the channel, which may later lead to problems during bonding (Fig. 1.20).[137]
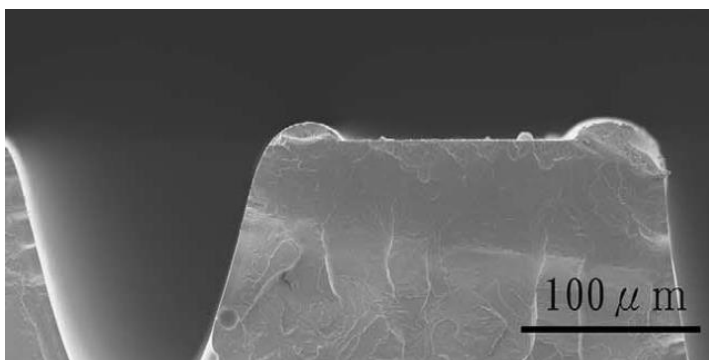
Figure 1.20: Laser-ablated surface showing material deposited on the sides; Gaussian shaped channel.[136]

1.6 Microfluidic Analytical Techniques

1.6.1 Separations

Analytical separation, in the form of gas chromatography, was the first operation ever reported on a µTAS device, where a mixture of simple compounds was resolved on a 1.5 m long column in just a few seconds.[3] Miniaturization in analytical separations leads to reduced analysis time and increased

performance,[4] where both electroosmotic and pressure-driven flow approaches are widely represented.[9,138]

Electrophoresis on a microchip was first reported in 1992, and since then has become one of the dominant separation approaches in a microchip format.[139] Initially, electroosmotic pumping was the technique of choice, as this approach does not require mechanical moving parts or connectors that add complexity to device fabrication.[9] Both the injection and the separation flow are controlled by applying appropriate voltages to specific locations along the channels or reservoirs. A variety of different classes of compounds have been separated using electroosmotic approaches.[140-143] Dyes, amino acids, small drug molecules, proteins, DNA, and whole cells have been separated on a microchip where high-resolution separations have been demonstrated on sub-centimetre columns in just a few seconds.[144-147] Regardless of its popularity, the electroosmotic approach is not without its flaws and challenges; the analyte charge, buffer pH, and channel material must be carefully selected for compatibility. High applied voltage and the resulting Joule heating can further limit the performance of μTAS, and often contributes to fabrication challenges. As an alternative, microchip LC is explored in Chapter 2 and is discussed in further detail below.

1.6.2 Liquid Chromatography

LC is a more established technique in analytical chemistry, where virtually any class of compound can be efficiently separated under appropriate conditions. However, due to more sophisticated fluid control and fabrication limitations, LC is not as easily implemented onto a microchip format. Fluid flow in microchannels requires high pressures, where specific infrastructure (i.e. pumps, injectors) and fabrication considerations (i.e. device robustness) must be accounted for. Smaller microchannels offer the advantages of faster diffusion and more efficient separation; however, that in turn requires even higher pressures to efficiently move the mobile phase and analytes through the channels.[148] There are reports of miniaturized pumps and injectors implemented directly onto the

microchip,[10,149,150] however for LC separations it is common to have external pumps, which can limit portability of such a device.

The first miniaturized LC column was demonstrated in 1967 by Horvath,[151] prior to the introduction of microchip format, and was popularized in late 1970s by Ishii.[152,153] The main advantages of miniaturized LC include low sample requirements, fast analysis time arising from small volumetric flow rates and enhanced detection sensitivity due to low dilution factors. It is no surprise that this high-demand technique, first demonstrated in a microfluidic device by Manz et al. in 1995,[154] has been further implemented/developed for over two decades. Various stationary phase approaches have been implemented in microchannels, where standard bead packing, porous polymer monolith (PPM) and open tubular are the most popular (Fig. 1.21).
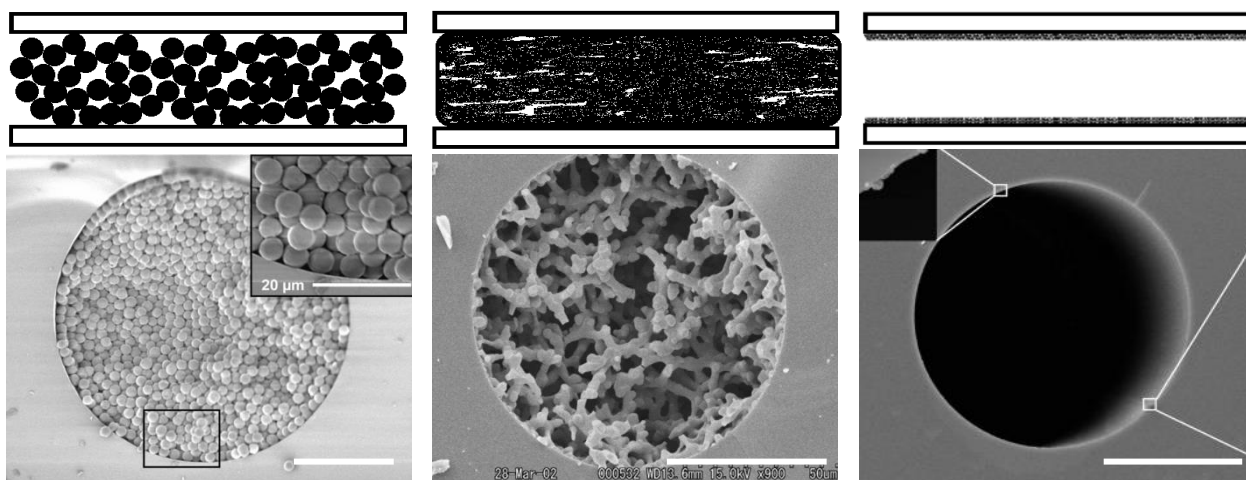
Figure 1.21: Schematics (top) and examples (bottom) of stationary phases commonly used in microfluidic LC. (left) 180 µm I.D. column packed with 5 µm C18-modified particles;[155] (centre) monolith column inside a 100 µm I.D. fused-silica capillary;[156] (right) 75 µm I.D. fused-silica capillary modified with two layers of graphene oxide.[157] The scale bar is 50 µm for each of the electron micrographs.

Short channels allow for fast separations, while narrow channels lower diffusion distances and increase resolution. Reduced dimensions of the particles in the stationary phase allows for better packing leading to superior performance; 3.0 and 1.5 µm particles are now considered the standard, and submicron particles are not uncommon.[158,159] The adaptation of micro-chromatography was not without challenges, where smaller channel dimensions and micron-sized stationary phases require

ultra-high pressures to enable the liquid flow through the channels. High-resolution separations depend on tight, void-free packing, which in turn requires even higher pressures. Therefore, efficient separations require pumping systems capable of delivering such high pressures, as well as devices capable of withstanding pressures in excess of 70 MPa.[159] The high-pressure demands can limit the choice of the microchip material, e.g. many polymeric devices tend to deform under applied higher pressures (i.e. elastomers) or split open in the weakest spot (i.e. thermoplastics). Significant effort has been dedicated to researching and developing new microchip materials and fabrication methods that can improve device robustness and allow them to withstand high and ultra-high pressures.

Another way around minimizing pressure requirements is the introduction of highly permeable alternative packing materials, like porous polymeric stationary phase and/or open tubular methods.[160,161] PPM can be easily introduced inside channels as a liquid solution, which will polymerize with a proper trigger (light or heat initiation).[162] Due to the high porosity of these materials, longer columns can be efficiently filled and operated under relatively low backpressures and/or high flow rates.[163] It is also possible to control both the exact length and position of the PPM material with the photo-initiation approach, which can be beneficial for certain applications.[164] Combinations of solvents and monomers dictate the porosity and functionalization of the monolith produced, which can be tailored for specific applications.[164-167] The porous nature of PPM is, however, irreproducible from device to device even under the same polymerization conditions. Furthermore, the presence of the irregular voids in the material can lead to reduced separation performance.[156]

Open tubular approaches, adapted from GC, are based upon modifying the channel walls with appropriate functional groups and flowing the reagents through the unpacked channel.[157,168] Effective separation is possible as the reduced channel diameter increases the surface-to-volume ratio and allows for increased wall interaction.[169] However, to compete with packed columns, channel dimensions of 10 μm or less are required, which is challenging from both fabrication (high precision) and operational (high pressures) stand points.[170] The open-tubular approach is more popular with electroosmotic

36

separations, which requires no pressure-induced flow to operate.[171,172] Open-tubular approaches offer low column loading capacity, limiting the volumes of the analytes that can be analyzed. A major concern for micro-chromatography is the dead volume arising due to the presence of pumps, valves, interconnections, frits and emitters. A dead volume of several microlitres can go unnoticed in standard chromatography columns, but a few nanolitres of dead-volume can have devastating effects on resolution of microcolumns.[148,173]

Packing frits, small obstacles in a channel that allow for liquid flow but retain stationary phases, can significantly contribute to dead volume, thus they often pose a significant design challenge. Frits can be microfabricated into glass channels by standard photolithography and wet etching techniques, however they tend to be unstable under high pressures or add significant complexity to the design.[7] Channel obstructions (e.g. weir) can also be introduced, but particle size and packing density must be reproducible from device to device.[158,174,175] The keystone effect,[176,177] where a narrow opening blocks particles causing particle accumulation, also known as "fritless" approach, and is often used to minimize dead volume (Fig. 1.22).
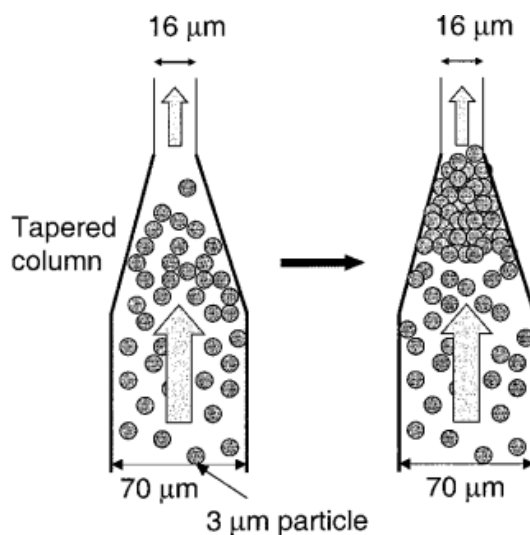
Figure 1.22: An example of the "keystone" phenomenon, where smaller particles accumulate and block the microfluidic channel as a means of retaining the stationary phase in the column.[176]

Short sections of PPM can also serve as frits for high resolution silica bead-based packing, but it can also further contribute to dead-volume by adding post-column space.[7] Integration of emitters for

37

online ESI-MS detection (discussed in 1.6.4) can lead to similar dead-volume concerns, and must be addressed accordingly.

1.6.3 Detection

Limited quantities of the analytes and their inherent properties dictate the choice of the detection technique, which should be compact, versatile and sensitive. A variety of detection methods and techniques have been realized on a microchip format, where optical detection, electrochemical sensing and mass spectrometry are the most common. Fluorescence is common for µTAS devices, as it can be easily adapted to the reduced dimensions.[178] Low divergence excitation sources (laser-induced fluorescence, light-emitting diodes) can be precisely focused on minute amounts of analyte, and result in unmatched sensitivity.[27] Standard UV-vis absorbance is more versatile in terms of analytes and wavelength selection, however due to reduced optical path length its sensitivity is reduced significantly. Multiple designs have been introduced to counter the problem of short path length, but not without an increase in fabrication complexity.[179,180] Electrochemical detection, i.e. potentiometry and amperometry, is based on changes in electrical properties of analytes as a result of redox reactions.[180] These approaches are cost effective and have low resource demand, thus they are very popular on single-use devices, and especially paper-based LOCs.[181] Electrochemical detection can be easily implemented into microfluidic devices,[182] however it is analyte specific and strongly dependent on the properties of the bulk solution (e.g. pH, ionic strength etc.).[183] Mass spectrometers are not easily miniaturized, however they offer sensitivity, selectivity and compound identification, making them popular choices for µTAS devices.[23,184] Various mass spectrometry methods have been successfully implemented with lab-of-a-chip devices (both digital and continuous flow approaches) and these coupling strategies are discussed in detail below.

1.6.4 Coupling Mass Spectrometry with Microfluidic Devices

MS separates gas-phase ionized molecules based on their mass-to-charge ratio, and can be used to identify and quantify virtually any class of chemical compound – organic and inorganic

molecules, small drug entities, catalysts, large biological molecules and even whole organisms have been analyzed. MS is a well-established technique that is routinely used in various areas of modern analytical chemistry. In fact, thousands of scientific publications on MS research are produced each year and there are specialized journals dedicated to the methods, techniques and instrumentation of mass spectrometry (e.g. *Journal of Mass Spectrometry*, *International Journal of Mass Spectrometry*, *Journal of American Society of Mass Spectrometry*, etc.). Different MS ionization techniques are compatible with miniaturization, making MS a popular choice in microdevices. Two of the most common ways of interfacing microchips with MS are done through electrospray ionization (ESI)[23,28,185] or matrix-assisted laser desorption ionization (MALDI),[186,187] but alternative methods such as atmospheric pressure photoionization (APPI),[188] atmospheric pressure chemical ionization (APCI),[189,190] and desorption electrospray ionization (DESI)[191] are also utilized.

"Continuous flow" μTAS, i.e. electroosmotic and pressure-driven chromatography-based devices, are readily coupled with nano-ESI because both operate at similar flow rates (nanolitres to few microlitres per minute) and analyte ionization happens under atmospheric pressure.[192] The nano-ESI process is very similar to the standard ESI, where a fine droplet aerosol is produced under applied high voltage.[193] As the droplets move into vacuum the solvent is evaporated, and in a series of Coulombic explosions gas-phase ions are produced, which can be detected and identified (Fig. 1.23).[194,195] Due to the smaller initial droplets produced under low flow rates, solvent evaporation and the resulting ion formation is enhanced, thus increased sensitivity through better desolvation is often observed with nano-ESI.[196]
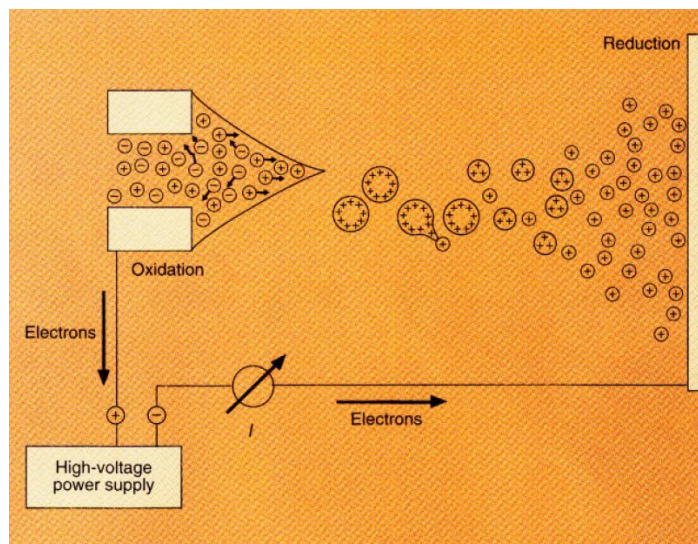
Figure 1.23: Schematic of the positive-mode ESI process to generate gas-phase ions.[194]

ESI is a "soft" ionization technique; it does not result in significant analyte fragmentation and decomposition, and produces single and/or multiple charge(s) on an ion, making it suitable for large-molecule analysis. Combined with microchip technology, ESI-MS has become a powerful tool for proteomics, metabolomics, pharmacokinetics, glycomics, etc.[146,185,197] An important consideration for the ESI process is the formation of the ions under applied potential, typically realized with an electrospray emitter, which is coupled to the liquid sample delivery system on one end, and the mass analyzer at the other end. Introducing these emitters onto the microdevices is one of the major challenges of microchip-ESI integration, mainly due to fabrication limitations. There are three common ways to couple microchips with ESI-MS: directly from the edge, attached emitters, and integrated emitters (Fig. 1.24).
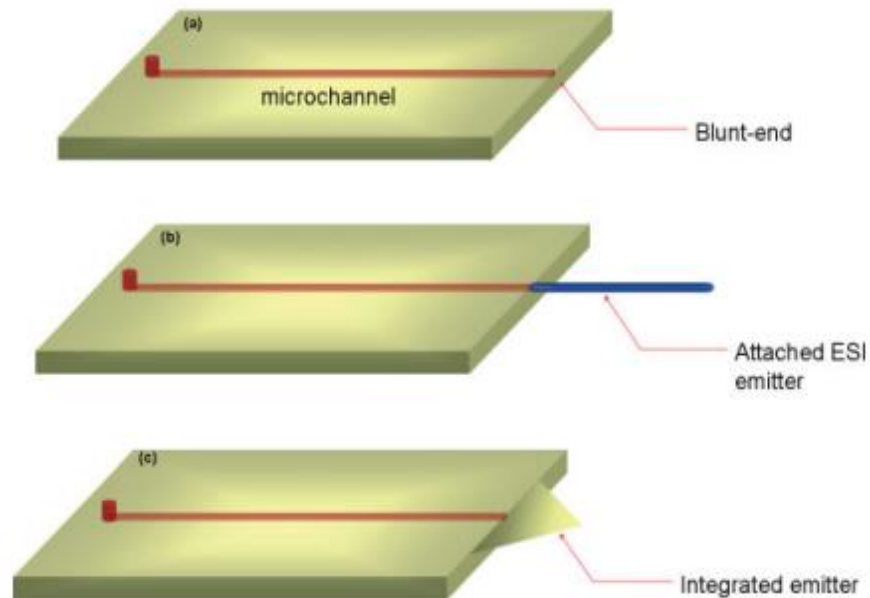
Figure 1.24: Schematic diagram showing three common ways of coupling an ESI-MS emitter to a microchip: a) from the edge; b) attached emitter; c) integrated emitter.[197]

Due to its simplicity, the edge-spraying, was the first microchip-ESI coupling method introduced in the 1990s, where the electrospray is generated directly from the microchannel opening at the edge of the chip.[198] Due to the hydrophilic nature of the materials and flat-end geometry of the edge, the cone tends to spread over the edge of the chip, leading to surface wetting and spray instability. The wetted surface volume can be high enough to produce significant dead volume, which lowers the sensitivity and causes band broadening.[199] The formation of large droplets on the microchip edge can lead to unstable electrospray, and can sometimes lead to cone repositioning.[23] To minimize these effects, several techniques can be implemented; however, they tend to be non-permanent (e.g. hydrophobic coatings), or can further complicate the device fabrication/operation (e.g. aerodynamic interfacing).[197,200] Along with these standard approaches, monolithic emitters have been integrated successfully to aid spraying from the edge.[201,202]

An improved coupling method is achieved by separately connecting commercial fused silica emitters to the channel exit, where the potential is applied to the emitter tip. The electrospray produced tends to be stable and reproducible, however the difference in inner diameter of the microchannel and

the emitter introduces significant dead volume, which can cause band broadening and lowers resolution significantly.[203]

The most efficient way of coupling microchips with ESI is by using integrated microfabricated emitters. The general design is similar to attached emitters, where a stable electrospray is generated from a protruding tapered hollow tube, where multiple geometries, materials and manufacturing methods have been successfully utilized (Fig. 1.25). As these emitters are integrated into the device, they are usually not associated with significant dead volume, and produce stable and reproducible electrospray.[23,184,197,204] The only drawback of these emitters is their production, where most designs require costly, time-consuming and elaborated cleanroom fabrication, limiting their widespread use.[205]
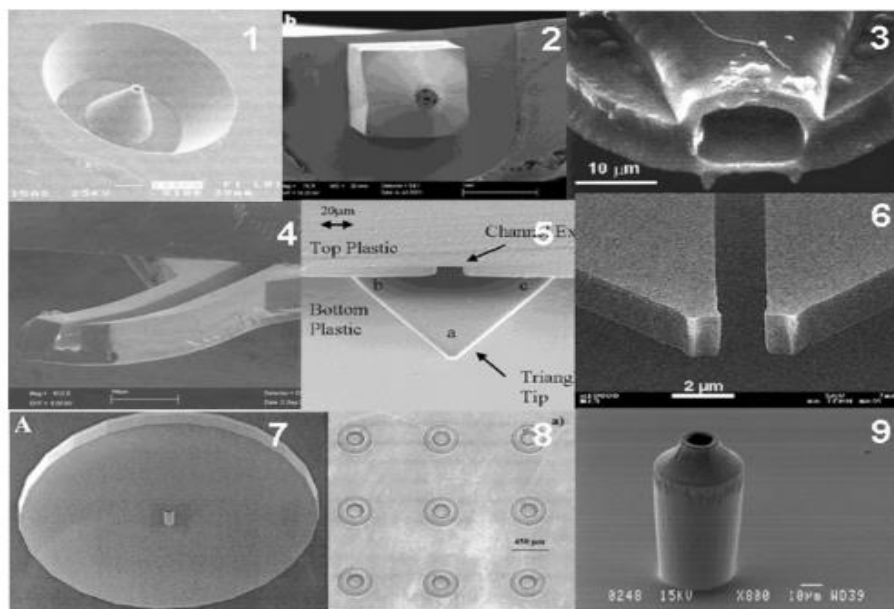
Figure 1.25: Several examples of microfabricated emitters integrated into microchips.[23]

Overall, the coupling of "continuous flow" microdevices with ESI-MS, while challenging, has been successfully realized. A much more interesting challenge lies in coupling digital microfluidics with ESI, as there is a need for converting the digital format into a compatible continuous flow format. Several coupling approaches have been proposed by the Wheeler[40,206] and Roper[207] groups, where a connecting capillary or an emitter is attached to the edge of the device, and the emitter/capillary can be filled with an actuated droplet using capillary action and/or pneumatic assistance. Kirby et al.

developed a more direct "origami" approach, where the DMF device itself serves as a nano-ESI emitter. The device is folded on itself to produce a cone with a fine orifice (Fig. 1.26).[208]
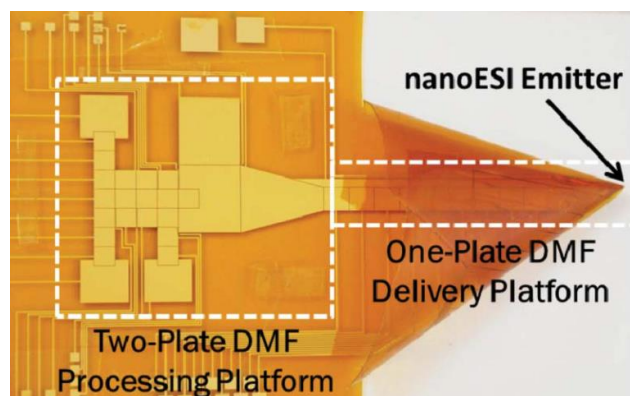
Figure 1.26: Microfluidic "origami" device, where a part of the DMF device can be folded to produce a cone with a narrow opening which can be used for direct ESI analysis.[208]

Another common method of microchip-MS coupling is done through MALDI which has been demonstrated in both continuous and digital formats. MALDI employs a laser to ablate and desorb a sample co-crystalized with matrix, the mechanism of which is still highly debated.[209] Due to a co-crystallization requirement, MALDI is normally used for offline analysis. Offline methods allow for the microdevice-processed samples to be further enhanced or optimized before the MS analysis – by using filtration, pre-concentration or enzymatic digestion.[187] Co-crystalized samples can be re-analyzed using different conditions or with different instrumentation, which can be advantageous for forensics or biomedical applications.[186,210] Parallel detection is better suited for offline MALDI, where multiple samples can be analyzed on the same target, even though the actual analysis is done in a sequential fashion.[211,212] Nevertheless, ways of coupling microchips with online MALDI have also been developed.

Musyimi proposed a design containing a rotating ball, where the analyte is being continuously eluted on the rotating surface, followed by matrix deposition onto the ball.[213] The sample and matrix deposition steps are done under atmospheric pressure, but as the wheel rotates it enters into a vacuum, where laser-induced ionization occurs. Online reaction monitoring was demonstrated with MALDI directly through the channels, where a transparent portion of the channel allows for laser ionization,

and the ions can travel into the MS through a sub-micron hole.[214] Microdevices themselves can be used as a target; in some cases, as the sample is eluted, the matrix is applied simultaneously and, following the co-crystallization, the microchip can be directly subjected to the laser pulses.[187,197] This is a common method of analysis in commercially available CD microchips.[215] In another approach the sample and the matrix are both injected into a microchip, and co-crystallization occurs in the open capillaries of the chip. The solvent is then vapourized, and the mixture of sample and matrix are analyzed directly in the sample channels. A similar principle is commonly used in coupling DMF devices with MALDI, where individual droplets containing analyte can be easily merged with matrix-containing droplets. These combined droplets can then be actuated to the desired locations on the microchip surface to be co-crystalized by evaporation.[53,216,217]

1.7 Project Objectives

The main aim of this thesis is to demonstrate the versatility and the merits of the microfluidic field of research, where a number of microfluidic approaches, fabrication methods and materials, on-chip operations and applications are explored and demonstrated.

A "continuous flow" COC-based microchip for LC separation with online ESI-MS detection is demonstrated in Chapter 2. Part of this chapter has been published in *Microfluidics and Nanofluidics*. Fabrication techniques unique to thermoplastics were utilized to fabricate a robust device capable of separating small drugs and large biological molecules, where a microstructured fibre (MSF) was used as a nano-ESI-MS emitter.

Chapters 3 to 5 exploit the merits and challenges of the DMF format, where discrete droplets are addressed as opposed to bulk flow. Two droplet actuation approaches, EWOD and magnetic actuation, are demonstrated on custom and commercial superhydrophobic surfaces. The EWOD approach is explored on a variety of natural and synthetic (super)hydrophobic surfaces, where systematic analysis demonstrates feasibility of this approach on a custom fluorinated silica

nanoparticle (FSNP)-based surface (Chapter 3). The main body of Chapter 3 has been published in the *Microelectronic Engineering* special issue on micro/nano emerging technologies.

Chapter 4 examines particle-based magnetic actuation on DMF devices, where water contact angles, roll-off angles and adhesion forces are used to characterize the surfaces suitable for this approach. We looked at a natural superhydrophobic surface, commercial hydrophobic surface (Teflon) and a commercial superhydrophobic FSNP-based surface, and determined that FSNP-based surface is best suited for magnetic actuation, due to its high robustness and low surface friction. Parts of chapter 4 have been published in *Sensors and Actuators B: Chemical*.

The first report of particle-free magnetic actuation is presented in Chapter 5, where droplets of various paramagnetic salts have been successfully actuated over a superhydrophobic surface. In this case we look at the magnetic susceptibility properties of each salt, and determine the minimum concentration required to actuate droplets of each salt. We demonstrate that salts with higher magnetic susceptibility can be actuated at lower concentrations and with higher speed; we also calculate magnetic force for each of the five salts tested. Online fluorescence detection of the anti-cancer drug in a salt containing droplet is also reported.

1.8 References

1.   D. R. Reyes, D. Iossifidis, P. A. Auroux and A. Manz, *Anal. Chem.*, 2002, **74**, 2623-36.

2.   C. T. Culbertson, T. G. Mickleburgh, S. A. Stewart-James, K. A. Sellens and M. Pressnall, *Anal. Chem.*, 2014, **86**, 95-118.

3.   S. C. Terry, J. H. Jerman and J. B. Angell, *Ieee Transactions on Electron Devices*, 1979, **26**, 1880-6.

4.   A. Manz, N. Graber and H. M. Widmer, *Sensor. Actuat. B-Chem.*, 1990, **1**, 244-8.

5.   G. M. Whitesides, *Nature*, 2006, **442**, 368-73.

6.   T. Sikanen, S. Franssila, T. J. Kauppila, R. Kostiainen, T. Kotiaho and R. A. Ketola, *Mass Spectrom. Rev.*, 2010, **29**, 351-91.

7.   X. C. Wang, X. H. Yang and X. M. Zrang, *Anal. Sci.*, 2006, **22**, 1099-104.

8.   E. K. Sackmann, A. L. Fulton and D. J. Beebe, *Nature*, 2014, **507**, 181-9.

9.   P. A. Auroux, D. Iossifidis, D. R. Reyes and A. Manz, *Anal. Chem.*, 2002, **74**, 2637-52.

10.   P. Woias, *Sensor. Actuat. B-Chem.*, 2005, **105**, 28-38.

11.   T. Nissila, L. Sainiemi, S. Franssila and R. A. Ketola, *Sensor. Actuat. B-Chem.*, 2009, **143**, 414-20.

12.   G. Deng and G. E. Collins, *J. Chromatogr., A*, 2003, **989**, 311-6.

13.   J. M. Gillies, C. Prenant, G. N. Chimon, G. J. Smethurst, B. A. Dekker and J. Zweit, *Appl. Radiat. Isot.*, 2006, **64**, 333-6.

14.   D. Mijatovic, J. C. Eijkel and A. van den Berg, *Lab Chip*, 2005, **5**, 492-500.

15.   G. S. Fiorini and D. T. Chiu, *BioTechniques*, 2005, **38**, 429-46.

16.   H. Becker and L. E. Locascio, *Talanta*, 2002, **56**, 267-87.

17.   D. M. Cate, J. A. Adkins, J. Mettakoonpitak and C. S. Henry, *Anal. Chem.*, 2015, **87**, 19-41.

18.   W. K. Coltro, D. P. de Jesus, J. A. da Silva, C. L. do Lago and E. Carrilho, *Electrophoresis*, 2010, **31**, 2487-98.

19.   T. Songjaroen, W. Dungchai, O. Chailapakul, C. S. Henry and W. Laiwattanapaisal, *Lab Chip*, 2012, **12**, 3392-8.

20.   X. Yang, N. Z. Piety, S. M. Vignes, M. S. Benton, J. Kanter and S. S. Shevkoplyas, *Clin. Chem.*, 2013, **59**, 1506-13.

21.   R. Ehrnstrom, *Lab Chip*, 2002, **2**, 26-30.

22.   B. Teste, A. Ali-Cherif, J. L. Viovy and L. Malaquin, *Lab Chip*, 2013, **13**, 2344-9.

23.   S. Koster and E. Verpoorte, *Lab Chip*, 2007, **7**, 1394-412.

24.   H. Chen, A. Abolmatty and M. Faghri, *Microfluid. Nanofluid.*, 2011, **10**, 593-605.

25.   N. Pamme, *Lab Chip*, 2007, **7**, 1644-59.

26. O. Strohmeier, M. Keller, F. Schwemmer, S. Zehnle, D. Mark, F. von Stetten, R. Zengerle and N. Paust, *Chem. Soc. Rev.*, 2015, **44**, 6187-229.

27. S. Gotz and U. Karst, *Anal. Bioanal. Chem.*, 2007, **387**, 183-92.

28. M. Karas, U. Bahr and T. Dulcks, *Fresen. J. Ana.l Chem.*, 2000, **366**, 669-76.

29. M. Abdelgawad and A. R. Wheeler, *Adv. Mater.*, 2009, **21**, 920-5.

30. R. Sista, Z. S. Hua, P. Thwar, A. Sudarsan, V. Srinivasan, A. Eckhardt, M. Pollack and V. Pamula, *Lab Chip*, 2008, **8**, 2091-104.

31. F. Mugele and J.-C. Baret, *J. Phys.: Condens. Matter*, 2005, **17**, 705-74.

32. D. Chatterjee, B. Hetayothin, A. R. Wheeler, D. J. King and R. L. Garrell, *Lab Chip*, 2006, **6**, 199-206.

33. I. Moon and J. Kim, *Sens. Actuators A: Phys.*, 2006, **130-131**, 537-44.

34. M. Abdelgawad and A. R. Wheeler, *Microfluid. Nanofluid.*, 2007, **4**, 349-55.

35. S. K. Cho, H. J. Moon and C. J. Kim, *J. Microelectromech. Syst.*, 2003, **12**, 70-80.

36. D. Brassard, L. Malic, F. Normandin, M. Tabrizian and T. Veres, *Lab Chip*, 2008, **8**, 1342-9.

37. A. Banerjee, Y. Liu, J. Heikenfeld and I. Papautsky, *Lab Chip*, 2012, **12**, 5138-41.

38. A. Accardo, F. Mecarini, M. Leoncini, F. Brandi, E. Di Cola, M. Burghammer, C. Riekel and E. Di Fabrizio, *Lab Chip*, 2013, **13**, 332-5.

39. S. K. Cho, S. K. Fan, H. J. Moon and C. J. Kim, *Fifteenth Ieee International Conference on Micro Electro Mechanical Systems, Technical Digest*, 2002, 32-5.

40. S. C. Shih, H. Yang, M. J. Jebrail, R. Fobel, N. McIntosh, O. Y. Al-Dirbashi, P. Chakraborty and A. R. Wheeler, *Anal. Chem.*, 2012, **84**, 3731-8.

41. Y. J. Zhao, U. C. Yi and S. K. Cho, *J. Microelectromech. Syst.*, 2007, **16**, 1472-81.

42. D. Beyssen, L. Le Brizoual, O. Elmazria and P. Alnot, *Sensor. Actuat. B-Chem.*, 2006, **118**, 380-5.

43. N. Pamme, *Lab Chip*, 2006, **6**, 24-38.

44.   Z. Long, A. M. Shetty, M. J. Solomon and R. G. Larson, *Lab Chip*, 2009, **9**, 1567-75.

45.   L. Mats, R. Young, G. T. T. Gibson and R. D. Oleschuk, *Sensor. Actuat. B-Chem.*, 2015, **220**, 5-12.

46.   K. H. Kang, *Langmuir*, 2002, **18**, 10318-22.

47.   J. Zeng and T. Korsmeyer, *Lab Chip*, 2004, **4**, 265-77.

48.   R. Bavière, J. Boutet and Y. Fouillet, *Microfluid. Nanofluid.*, 2007, **4**, 287-94.

49.   H. Moon, S. K. Cho, R. L. Garrell and C.-J. C. Kim, *J. Appl. Phys.*, 2002, **92**, 4080-7.

50.   A. Egatz-Gomez, S. Melle, A. A. Garcia, S. A. Lindsay, M. Marquez, P. Dominguez-Garcia, M. A. Rubio, S. T. Picraux, J. L. Taraci, T. Clement, D. Yang, M. A. Hayes and D. Gust, *Appl. Phys. Lett.*, 2006, **89**, 034106.

51.   A. A. García, A. Egatz-Gómez, S. A. Lindsay, P. Domínguez-García, S. Melle, M. Marquez, M. A. Rubio, S. T. Picraux, D. Yang, P. Aella, M. A. Hayes, D. Gust, S. Loyprasert, T. Vazquez-Alvarez and J. Wang, *J. Magn. Magn. Mater.*, 2007, **311**, 238-43.

52.   J. F. Nie, Y. Zhang, H. Wang, S. P. Wang and G. L. Shen, *Biosens. Bioelectron.*, 2012, **33**, 23-8.

53.   N. S. Mei, B. Seale, A. H. C. Ng, A. R. Wheeler and R. Oleschuk, *Anal. Chem.*, 2014, **86**, 8466-72.

54.   H. Zhang and S. G. Weber, *Top. Curr. Chem.*, 2012, **308**, 307-37.

55.   M. Ma and R. M. Hill, *Curr. Opin. Colloid Interface Sci.*, 2006, **11**, 193-202.

56.   J. Genzer and K. Efimenko, *Biofouling*, 2006, **22**, 339-60.

57.   B. Bhushan and Y. C. Jung, *Nanotechnology*, 2006, **17**, 2758-72.

58.   B. Bhushan and Y. C. Jung, *Prog. Mater. Sci.*, 2011, **56**, 1-108.

59.   A. B. D. Cassie and S. Baxter, *T. Faraday Soc.*, 1944, **40**, 0546-50.

60.   J. A. Watson, H.-M. Hu, B. W. Cribb and G. S. Watson, *Anti-wetting on insect cuticle–structuring to minimise adhesion and weight*, InTech Publishing, 2011.

61. L. Afferrante and G. Carbone, *Soft Matter*, 2014, **10**, 3906-14.

62. Y. T. Cheng, D. E. Rodak, C. A. Wong and C. A. Hayden, *Nanotechnology*, 2006, **17**, 1359-62.

63. K. Koch, A. Dommisse and W. Barthlott, *Cryst. Growth Des.*, 2006, **6**, 2571-8.

64. H. J. Ensikat, P. Ditsche-Kuru, C. Neinhuis and W. Barthlott, *Beilstein J. Nanotechnol.*, 2011, **2**, 152-61.

65. J. Lin, Y. Cai, X. Wang, B. Ding, J. Yu and M. Wang, *Nanoscale*, 2011, **3**, 1258-62.

66. X. Zhang, F. Shi, J. Niu, Y. Jiang and Z. Wang, *J. Mater. Chem.*, 2008, **18**, 621-33.

67. T. Onda, S. Shibuichi, N. Satoh and K. Tsujii, *Langmuir*, 1996, **12**, 2125-7.

68. Z. J. Cheng, H. Lai, N. Q. Zhang, K. N. Sun and L. Jiang, *J. Phys. Chem. C*, 2012, **116**, 18796-802.

69. A. Egatz-Gómez, J. Schneider, P. Aella, D. Yang, P. Domínguez-García, S. Lindsay, S. T. Picraux, M. A. Rubio, S. Melle, M. Marquez and A. A. García, *Appl. Surf. Sci.*, 2007, **254**, 330-4.

70. M. S. Dhindsa, N. R. Smith, J. Heikenfeld, P. D. Rack, J. D. Fowlkes, M. J. Doktycz, A. V. Melechko and M. L. Simpson, *Langmuir*, 2006, **22**, 9030-4.

71. X. Men, Z. Zhang, J. Yang, X. Zhu, K. Wang and W. Jiang, *New J. Chem.*, 2011, **35**, 881-6.

72. J. Schneider, A. Egatz-Gómez, S. Melle, S. Lindsay, P. Domínguez-García, M. A. Rubio, M. Márquez and A. A. García, *Colloids Surf., A*, 2008, **323**, 19-27.

73. H. M. Shang, Y. Wang, S. J. Limmer, T. P. Chou, K. Takahashi and G. Z. Cao, *Thin Solid Films*, 2005, **472**, 37-43.

74. H. Wang, J. Fang, T. Cheng, J. Ding, L. Qu, L. Dai, X. Wang and T. Lin, *Chem. Commun.*, 2008, 877-9.

75. N. Gao and Y. Y. Yan, *Nanoscale*, 2012, **4**, 2202-18.

76. L. Cao, A. K. Jones, V. K. Sikka, J. Wu and D. Gao, *Langmuir*, 2009, **25**, 12444-8.

77.   D. Xiong, G. Liu and E. J. Duncan, *Langmuir*, 2012, **28**, 6911-8.

78.   X. M. Li, D. Reinhoudt and M. Crego-Calama, *Chem. Soc. Rev.*, 2007, **36**, 1350-68.

79.   M. C. Draper, C. R. Crick, V. Orlickaite, V. A. Turek, I. P. Parkin and J. B. Edel, *Anal. Chem.*, 2013, **85**, 5405-10.

80.   Z. G. Guo, F. Zhou, J. C. Hao, Y. M. Liang, W. M. Liu and W. T. S. Huck, *Appl. Phys. Lett.*, 2006, **89**, 081911.

81.   X. Hong, X. F. Gao and L. Jiang, *J. Am. Chem. Soc.*, 2007, **129**, 1478-9.

82.   E. Bormashenko, R. Pogreb, Y. Bormashenko, A. Musin and T. Stein, *Langmuir*, 2008, **24**, 12119-22.

83.   W. C. Nelson and C. J. Kim, *J. Adhes. Sci. Technol.*, 2012, **26**, 1747-71.

84.   F. Saeki, J. Baum, H. Moon, J. Y. Yoon, C. J. Kim and R. L. Garrell, *Abstr. Pap. Am. Chem. S.*, 2001, **222**, 341-2.

85.   A. G. Papathanasiou, A. T. Papaioannou and A. G. Boudouvis, *J. Appl. Phys.*, 2008, **103**, 034901.

86.   M. Jonsson-Niedziolka, F. Lapierre, Y. Coffinier, S. J. Parry, F. Zoueshtiagh, T. Foat, V. Thomy and R. Boukherroub, *Lab Chip*, 2011, **11**, 490-6.

87.   M. Abdelgawad, S. L. S. Freire, H. Yang and A. R. Wheeler, *Lab Chip*, 2008, **8**, 672-7.

88.   M. Dhindsa, S. Kuiper and J. Heikenfeld, *Thin Solid Films*, 2011, **519**, 3346-51.

89.   H. Liu, S. Dharmatilleke, D. K. Maurya and A. A. O. Tay, *Microsyst. Technol.*, 2010, **16**, 449-60.

90.   V. N. Luk, G. C. H. Mo and A. R. Wheeler, *Langmuir*, 2008, **24**, 6382-9.

91.   S. H. Au, P. Kumar and A. R. Wheeler, *Langmuir*, 2011, **27**, 8586-94.

92.   A. Accardo, F. Gentile, M. L. Coluccio, F. Mecarini, F. De Angelis and E. Di Fabrizio, *Microelectron. Eng.*, 2012, **98**, 651-4.

93.   J. Heikenfeld and M. Dhindsa, *J. Adhes. Sci. Technol.*, 2008, **22**, 319-34.

94.   U. Lehmann, S. Hadjidj, V. K. Parashar, C. Vandevyver, A. Rida and M. A. M. Gijs, *Sensor. Actuat. B-Chem.*, 2006, **117**, 457-63.

95.   Q. A. Pankhurst, J. Connolly, S. K. Jones and J. Dobson, *J. Phys. D.: Appl. Phys.*, 2003, **36**, 167-81.

96.   M. C. Weston, M. D. Gerner and I. Fritsch, *Anal. Chem.*, 2010, **82**, 3411-8.

97.   R. E. Rosensweig, *Ferrohydrodynamics*, Cambridge University Press, Cambridge ; New York, 1985.

98.   T. Neuberger, B. Schopf, H. Hofmann, M. Hofmann and B. von Rechenberg, *J. Magn. Magn. Mater.*, 2005, **293**, 483-96.

99.   A. K. Gupta and M. Gupta, *Biomaterials*, 2005, **26**, 3995-4021.

100.   A. Egatz-Gómez, S. Melle, A. A. García, S. A. Lindsay, M. Márquez, P. Domínguez-García, M. A. Rubio, S. T. Picraux, J. L. Taraci, T. Clement, D. Yang, M. A. Hayes and D. Gust, *Appl. Phys. Lett.*, 2006, **89**, 034106.

101.   A. H. C. Ng, K. Choi, R. P. Luoma, J. M. Robinson and A. R. Wheeler, *Anal. Chem.*, 2012, **84**, 8805-12.

102.   Q. A. Pankhurst, N. T. K. Thanh, S. K. Jones and J. Dobson, *J. Phys. D: Appl. Phys.*, 2009, **42**, 224001.

103.   N. Vergauwe, S. Vermeir, J. B. Wacker, F. Ceyssens, M. Cornaglia, R. Puers, M. A. M. Gijs, J. Lammertyn and D. Wittersaabios, *Sensor. Actuat. B-Chem.*, 2014, **196**, 282-91.

104.   M. Shikida, K. Takayanagi, K. Inouchi, H. Honda and K. Sato, *Sensor. Actuat. B-Chem.*, 2006, **113**, 563-9.

105.   Y. Zhang and T. H. Wang, *Adv. Mater.*, 2013, **25**, 2903-8.

106.   Y. N. Xia and G. M. Whitesides, *Annu. Rev. Mater. Sci.*, 1998, **28**, 153-84.

107.   H. Becker and C. Gartner, *Electrophoresis*, 2000, **21**, 12-26.

108.   P. S. Nunes, P. D. Ohlsson, O. Ordeig and J. P. Kutter, *Microfluid. Nanofluid.*, 2010, **9**, 145-61.

109.   J. T. Santini, Jr., M. J. Cima and R. Langer, *Nature*, 1999, **397**, 335-8.

110.   J. M. K. Ng, I. Gitlin, A. D. Stroock and G. M. Whitesides, *Electrophoresis*, 2002, **23**, 3461-73.

111.   S. E. Chung, W. Park, H. Park, K. Yu, N. Park and S. Kwon, *Appl. Phys. Lett.*, 2007, **91**.

112.   R. J. Blaikie, D. O. S. Melville and M. M. Alkaisi, *Microelectron. Eng.*, 2006, **83**, 723-9.

113.   R. P. Seisyan, *Tech. Phys.+*, 2011, **56**, 1061-73.

114.   C. Iliescu, B. T. Chen and J. Miao, *Sens. Actuators A: Phys.*, 2008, **143**, 154-61.

115.   L. Ceriotti, K. Weible, N. F. de Rooij and E. Verpoorte, *Microelectron. Eng.*, 2003, **67-8**, 865-71.

116.   X. X. Zhang and J. P. Raskin, *J. Microelectromech. Syst.*, 2005, **14**, 368-82.

117.   C. W. Tsao and D. L. DeVoe, *Microfluid. Nanofluid.*, 2009, **6**, 1-16.

118.   M. Vijay, E. Ghandehari, M. Goedert and S. J. J. Lee, *International Mechanical Engineering Congress and Exposition 2007, Vol 11 Pt a and Pt B: Micro and Nano Systems*, 2008, 351-6.

119.   H. J. Jacobasch, F. Simon and P. Weidenhammer, *Colloid Polym. Sci.*, 1998, **276**, 434-42.

120.   S. M. Mitrovski and R. G. Nuzzo, *Lab Chip*, 2005, **5**, 634-45.

121.   F. Bundgaard, T. Nielsen, D. Nilsson, P. X. Shi, G. Perozziello, A. Kristensen and O. Geschke, *Micro Total Analysis Systems 2004, Vol 2*, 2005, 372-4.

122.   C. W. Tsao, L. Hromada, J. Liu, P. Kumar and D. L. DeVoe, *Lab Chip*, 2007, **7**, 499-505.

123.   J. C. McDonald, D. C. Duffy, J. R. Anderson, D. T. Chiu, H. Wu, O. J. Schueller and G. M. Whitesides, *Electrophoresis*, 2000, **21**, 27-40.

124.   M. Nakao, K. Tsuchiya, T. Sadamitsu, Y. Ichikohara, T. Ohba and T. Ooi, *Int. J. Adv. Manuf. Tech.*, 2008, **38**, 426-32.

125.   V. Studer, A. Pepin and Y. Chen, *Appl. Phys. Lett.*, 2002, **80**, 3614-6.

126. M. Schelb, C. Vannahme, A. Kolew and T. Mappes, *J. Micromech. Microeng.*, 2011, **21**, 025017.

127. H. Becker and U. Heim, *Sens. Actuators A: Phys.*, 2000, **83**, 130-5.

128. R. K. Jena, S. A. Chester, V. Srivastava, C. Y. Yue, L. Anand and Y. C. Lam, *Sensor. Actuat. B-Chem.*, 2011, **155**, 93-105.

129. M. D. Douma, L. Brown, T. Koerner, J. H. Horton and R. D. Oleschuk, *Microfluid. Nanofluid.*, 2013, **14**, 133-43.

130. C. K. Fredrickson, Z. Xia, C. Das, R. Ferguson, F. T. Tavares and Z. H. Fan, *J. Microelectromech. S.*, 2006, **15**, 1060-8.

131. R. T. Kelly, T. Pan and A. T. Woolley, *Anal. Chem.*, 2005, **77**, 3536-41.

132. M. E. Wilson, N. Kota, Y. Kim, Y. D. Wang, D. B. Stolz, P. R. LeDuc and O. B. Ozdoganlar, *Lab Chip*, 2011, **11**, 1550-5.

133. C. S. Goh, S. C. Tan, K. T. May, C. Z. Chan and S. H. Ng, *2009 11th Electronics Packaging Technology Conference (Eptc 2009)*, 2009, 737-40.

134. C. Friedrich, B. Kikkeri and T. Nagarajan, *Proceedings of the Tenth Annual Meeting - the American Society for Precision Engineering*, 1995, 284-7.

135. B. A. Fogarty, K. E. Heppert, T. J. Cory, K. R. Hulbutta, R. S. Martin and S. M. Lunte, *The Analyst*, 2005, **130**, 924-30.

136. J. Y. Cheng, C. W. Wei, K. H. Hsu and T. H. Young, *Sensor. Actuat. B-Chem.*, 2004, **99**, 186-96.

137. H. Klank, J. P. Kutter and O. Geschke, *Lab Chip*, 2002, **2**, 242-6.

138. D. Erickson and D. Q. Li, *Anal. Chim. Acta*, 2004, **507**, 11-26.

139. A. Manz, D. J. Harrison, E. M. J. Verpoorte, J. C. Fettinger, A. Paulus, H. Ludi and H. M. Widmer, *J. Chromatogr.*, 1992, **593**, 253-8.

140. R. L. StClaire, *Anal. Chem.*, 1996, **68**, 569-86.

141.   M. C. Breadmore, *Electrophoresis*, 2007, **28**, 254-81.

142.   M. C. Breadmore, J. R. Thabano, M. Dawod, A. A. Kazarian, J. P. Quirino and R. M. Guijt, *Electrophoresis*, 2009, **30**, 230-48.

143.   P. Schulze and D. Belder, *Anal. Bioanal. Chem.*, 2009, **393**, 515-25.

144.   S. Terabe, M. R. N. Monton, T. Le Saux and K. Imami, *Pure Appl. Chem.*, 2006, **78**, 1057-67.

145.   P. Schulze, M. Schuttpelz, M. Sauer and D. Belder, *Lab Chip*, 2007, **7**, 1841-4.

146.   I. Ali, H. Y. Aboul-Enein and V. K. Gupta, *Chromatographia*, 2008, **69**, 13-22.

147.   P. Hommerson, A. M. Khan, T. Bristow, M. W. Harrison, G. J. de Jong and G. W. Somsen, *Rapid Commun. Mass Spectrom.*, 2009, **23**, 2878-84.

148.   J. P. C. Vissers, *J. Chromatogr., A*, 1999, **856**, 117-43.

149.   J. W. Munyan, H. V. Fuentes, M. Draper, R. T. Kelly and A. T. Woolley, *Lab Chip*, 2003, **3**, 217-20.

150.   H. Suzuki and R. Yoneyama, *Sensor. Actuat. B-Chem.*, 2003, **96**, 38-45.

151.   C. G. Horvath, B. A. Preiss and S. R. Lipsky, *Anal. Chem.*, 1967, **39**, 1422-8.

152.   D. Ishii, K. Asai, K. Hibi, T. Jonokuchi and M. Nagaya, *J. Chromatogr.*, 1977, **144**, 157-68.

153.   T. Takeuchi and D. Ishii, *J. Chromatogr.*, 1981, **213**, 25-32.

154.   G. Ocvirk, E. Verpoorte, A. Manz, M. Grasserbauer and H. M. Widmer, *Anal. Method. Instrum.*, 1995, **2**, 74-82.

155.   S. Ehlert, T. Rosler and U. Tallarek, *J. Sep. Sci.*, 2008, **31**, 1719-28.

156.   K. K. Unger, R. Skudas and M. M. Schulte, *J. Chromatogr., A*, 2008, **1184**, 393-415.

157.   Q. S. Qu, C. H. Gu and X. Y. Hu, *Anal. Chem.*, 2012, **84**, 8880-90.

158.   Q. Lu and G. E. Collins, *J. Chromatogr., A*, 2010, **1217**, 7153-7.

159.   K. K. Unger, D. Kumar, M. Grun, G. Buchel, S. Ludtke, T. Adam, K. Schumacher and S. Renker, *J. Chromatogr., A*, 2000, **892**, 47-55.

160.   I. Gusev, X. Huang and C. Horvath, *J. Chromatogr., A*, 1999, **855**, 273-90.

161.   G. Guiochon, *J. Chromatogr., A*, 2007, **1168**, 101-68.

162.   E. C. Peters, M. Petro, F. Svec and J. M. J. Frechet, *Anal. Chem.*, 1998, **70**, 2288-95.

163.   K. W. Ro, R. Nayak and D. R. Knapp, *Electrophoresis*, 2006, **27**, 3547-58.

164.   Z. P. Xu, G. T. T. Gibson and R. D. Oleschuk, *The Analyst*, 2013, **138**, 611-9.

165.   J. Křvenková, Z. Bilková and F. Foret, *J. Sep. Sci.*, 2005, **28**, 1675-84.

166.   M. Bedair and R. D. Oleschuk, *The Analyst*, 2006, **131**, 1316-21.

167.   K. J. Bachus, K. J. Langille, Y. Q. Fu, G. T. T. Gibson and R. D. Oleschuk, *Polymer*, 2015, **58**, 113-20.

168.   Y. Saito, K. Jinno and T. Greibrokk, *J. Sep. Sci.*, 2004, **27**, 1379-90.

169.   A. Manz, Y. Miyahara, J. Miura, Y. Watanabe, H. Miyagi and K. Sato, *Sensor. Actuat. B-Chem.*, 1990, **1**, 249-55.

170.   J. H. Knox and M. T. Gilbert, *J. Chromatogr.*, 1979, **186**, 405-18.

171.   G. Zhang, C. Qian, Y. Xu, X. Feng, W. Du and B. F. Liu, *J. Sep. Sci.*, 2009, **32**, 374-80.

172.   E. Guihen and J. D. Glennon, *J. Chromatogr., A*, 2004, **1044**, 67-81.

173.   S. Ehlert, K. Kraiczek, J. A. Mora, M. Dittmann, G. P. Rozing and U. Tallarek, *Anal. Chem.*, 2008, **80**, 5945-50.

174.   G. A. Lord, D. B. Gordon, P. Myers and B. W. King, *J. Chromatogr., A*, 1997, **768**, 9-16.

175.   R. D. Oleschuk, L. L. Shultz-Lockyear, Y. B. Ning and D. J. Harrison, *Anal. Chem.*, 2000, **72**, 585-90.

176.   L. Ceriotti, N. F. de Rooij and E. Verpoorte, *Anal. Chem.*, 2002, **74**, 639-47.

177.   M. Pumera, *Talanta*, 2005, **66**, 1048-62.

178.   D. Witters, K. Knez, F. Ceyssens, R. Puers and J. Lammertyn, *Lab Chip*, 2013, **13**, 2047-54.

179.   K. B. Mogensen and J. P. Kutter, *Electrophoresis*, 2009, **30**, 92-100.

180.   J. Wu and M. Gu, *J. Biomed. Opt.*, 2011, **16**, 080901.

181.   Z. Nie, C. A. Nijhuis, J. Gong, X. Chen, A. Kumachev, A. W. Martinez, M. Narovlyansky and G. M. Whitesides, *Lab Chip*, 2010, **10**, 477-83.

182.   J. Wang, *Talanta*, 2002, **56**, 223-31.

183.   A. Schuchert-Shi and P. C. Hauser, *Anal. Biochem.*, 2009, **387**, 202-7.

184.   W. C. Sung, H. Makamba and S. H. Chen, *Electrophoresis*, 2005, **26**, 1783-91.

185.   J. Srbek, J. Eickhoff, U. Effelsberg, K. Kraiczek, T. van de Goor and P. Coufal, *J. Sep. Sci.*, 2007, **30**, 2046-52.

186.   D. L. DeVoe and C. S. Lee, *Electrophoresis*, 2006, **27**, 3559-68.

187.   J. Lee, S. A. Soper and K. K. Murray, *Anal. Chim. Acta*, 2009, **649**, 180-90.

188.   T. J. Kauppila, P. Ostman, S. Marttila, R. A. Ketola, T. Kotiaho, S. Franssila and R. Kostiainen, *Anal. Chem.*, 2004, **76**, 6797-801.

189.   P. Ostman, S. Jantti, K. Grigoras, V. Saarela, R. A. Ketola, S. Franssila, T. Kotiaho and R. Kostiainen, *Lab Chip*, 2006, **6**, 948-53.

190.   L. Luosujarvi, M. M. Karikko, M. Haapala, V. Saarela, S. Huhtala, S. Franssila, R. Kostiainen, T. Kotiaho and T. J. Kauppila, *Rapid Commun. Mass Spectrom.*, 2008, **22**, 425-31.

191.   A. K. Sen, J. Darabi and D. R. Knapp, *Sensor. Actuat. B-Chem.*, 2009, **137**, 789-96.

192.   Q. F. Xue, F. Foret, Y. M. Dunayevskiy, P. M. Zavracky, N. E. McGruer and B. L. Karger, *Anal. Chem.*, 1997, **69**, 426-30.

193.   J. B. Fenn, M. Mann, C. K. Meng, S. F. Wong and C. M. Whitehouse, *Science*, 1989, **246**, 64-71.

194.   P. Kebarle and L. Tang, *Anal. Chem.*, 1993, **65**, 972-86.

195.   P. Kebarle and U. H. Verkerk, *Mass Spectrom. Rev.*, 2009, **28**, 898-917.

196.   M. Wilm and M. Mann, *Anal. Chem.*, 1996, **68**, 1-8.

197.   J. Lee, S. A. Soper and K. K. Murray, *J. Mass Spectrom.*, 2009, **44**, 579-93.

198. R. S. Ramsey and J. M. Ramsey, *Anal. Chem.*, 1997, **69**, 1174-8.

199. J. J. Li, P. Thibault, N. H. Bings, C. D. Skinner, C. Wang, C. Colyer and J. Harrison, *Anal. Chem.*, 1999, **71**, 3036-45.

200. J. Grym, M. Otevrel and F. Foret, *Lab Chip*, 2006, **6**, 1306-14.

201. T. Koerner, K. Turck, L. Brown and R. D. Oleschuk, *Anal. Chem.*, 2004, **76**, 6456-60.

202. X. Sun, R. T. Kelly, K. Tang and R. D. Smith, *The Analyst*, 2010, **135**, 2296-302.

203. D. E. Lee, S. Soper and W. Wang, *Microsyst. Technol.*, 2008, **14**, 1751-6.

204. G. T. Gibson, S. M. Mugo and R. D. Oleschuk, *Mass Spectrom. Rev.*, 2009, **28**, 918-36.

205. S. L. Freire, H. Yang and A. R. Wheeler, *Electrophoresis*, 2008, **29**, 1836-43.

206. M. J. Jebrail, H. Yang, J. M. Mudrik, N. M. Lafreniere, C. McRoberts, O. Y. Al-Dirbashi, L. Fisher, P. Chakraborty and A. R. Wheeler, *Lab Chip*, 2011, **11**, 3218-24.

207. C. A. Baker and M. G. Roper, *Anal. Chem.*, 2012, **84**, 2955-60.

208. A. E. Kirby and A. R. Wheeler, *Lab Chip*, 2013, **13**, 2533-40.

209. R. Zenobi and R. Knochenmuss, *Mass Spectrom. Rev.*, 1998, **17**, 337-66.

210. F. Foret and P. Kusy, *Electrophoresis*, 2006, **27**, 4877-87.

211. M. Petkovic and T. Kamceva, *Metallomics*, 2011, **3**, 550-65.

212. X. Wang, L. Yi, N. Mukhitov, A. M. Schrell, R. Dhumpa and M. G. Roper, *J. Chromatogr., A*, 2015, **1382**, 98-116.

213. H. K. Musyimi, J. Guy, D. A. Narcisse, S. A. Soper and K. K. Murray, *Electrophoresis*, 2005, **26**, 4703-10.

214. M. Brivio, N. R. Tas, M. H. Goedbloed, H. J. Gardeniers, W. Verboom, A. van den Berg and D. N. Reinhoudt, *Lab Chip*, 2005, **5**, 378-81.

215. M. Gustafsson, D. Hirschberg, C. Palmberg, H. Jornvall and T. Bergman, *Anal. Chem.*, 2004, **76**, 345-50.

216.   F. Lapierre, G. Piret, H. Drobecq, O. Melnyk, Y. Coffinier, V. Thomy and R. Boukherroub, *Lab Chip*, 2011, **11**, 1620-8.

217.   K. P. Nichols and H. J. G. E. Gardeniers, *Anal. Chem.*, 2007, **79**, 8699-704.

Chapter 2

Plastic LC/MS Microchip with an Embedded Microstructured Fibre

Having the Dual Role of a Frit and a Nanoelectrospray Emitter

2.1 Introduction

Microfluidic devices, or micro total analysis systems (µTAS), are miniaturized platforms which are particularly valuable for integrating one or several steps of chemical analysis in a single device. Advantages of microchips include reduced sample and reagent consumption, and rapid, high-throughput analysis. Various functions can be integrated onto a single device, including pumping, sample pre-treatment, separation and detection.[1-4]

For microscale separations such as liquid chromatography (LC), such integration is essential for reducing extra-column dead volume that contributes to poor separation efficiency. LC analysis in microfluidic devices is particularly challenging since the chip must be able to withstand the high pressures applied by the pump, and as such LC microchips have seen less use than other separation techniques like capillary electrophoresis (CE) despite LC being more established, robust and versatile. For conventional chromatographic packing material, a retaining frit must be incorporated into the channel. Monolithic stationary phases, such as porous polymer monoliths (PPM), circumvent frit-related issues but can be challenging to fabricate in their own right.[5,6] On-chip detection is typically preferred, but can be very complicated and/or limited in sensitivity (e.g. UV-vis absorption), selectivity (e.g. refractive index), or the kinds of analytes that can be detected (e.g. fluorescence). Mass spectrometers, on the other hand, are sensitive, informative detectors especially useful for online LC analysis. With a goal to interface LC with MS detection, a simple, robust, inexpensive LC microchip that has an integrated retaining frit and ESI emitter was prepared.

Integration of features into traditional microfluidic devices fabricated from glass or silica tends to be limited to microfabrication techniques such as photolithography and chemical etching.

When applied to microfluidic devices these methods and materials can be expensive and not well suited for single-use applications.[7] For example, frits have been patterned within glass channels by UV-initiated polymerization, but they can be irreproducible or unstable under high pressure.[8] Another common approach is the use of a channel obstruction such as a weir, whereby particles are retained while the mobile phase may pass through a small tapered opening.[9-11] Microfabricating such features, however, adds additional time, cost, and complexity. Integrating features into PDMS microdevices, another common µTAS substrate, is much simpler as the material is easily formed against a mould with good spatial resolution, however PDMS devices have a number of issues that make them unsuitable for LC including solvent incompatibility and poor robustness under pressure.[12-14]

Polymer devices are a promising alternative as they are inexpensive and can be rapidly prototyped using hot embossing techniques. Further, the microchip material properties can be tuned for the application, as a wide variety of polymers exist with vastly different physical and chemical properties. Cyclic olefin copolymer (COC; Zeonor) is an example of such material; it is cheaper to process than glass, has good mechanical properties and can be embossed with microstructures with high reproducibility. Further, COC is chemically inert to most commonly used polar LC and MS solvents and shows no reported carry-over, thus allowing for longer term device use.[15]

Another benefit of polymeric microfluidic chips fabricated by hot embossing is the ability to embed other microfluidic components in the polymer prior to bonding the cover plate. In this way, for example, capillary tubing can be embedded directly into the separation channel, which allows coupling with a LC pump without the need for a specialized port or drilled hole in the cover plate.[16] At the other end, an electrospray emitter may also be embedded in the channel, which is a much simpler and potentially more precise integration approach compared to attaching an external emitter to a glass chip, for example. Indeed, a great many approaches have been tried to effectively integrate nano-electrospray emitters into a microchip.[1,17]

The central feature in our microchip design is a microstructured fibre (MSF). Designed and marketed as optical fibres, MSFs are fabricated in silica and typically comprise an array of evenly spaced parallel channels of homogeneous size.[1] A SEM image of one example of MSF having 54 holes is shown in Fig. 2.1.
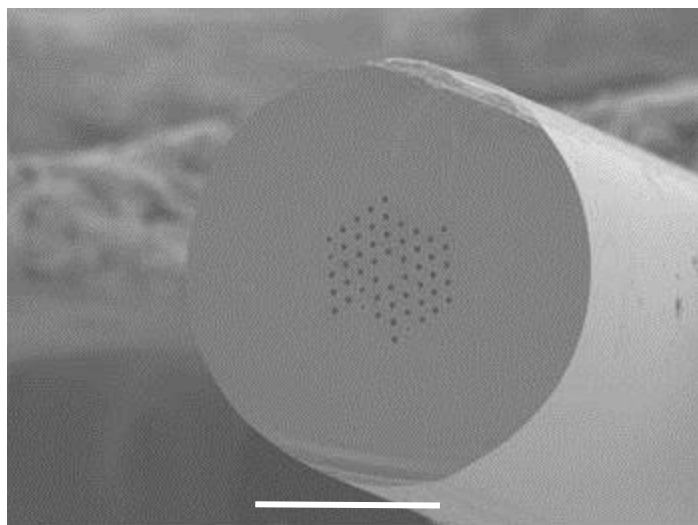
Figure 2.1: An SEM image of a 54-hole MSF with the outer polymer coating removed. Holes are ~3.8 μm, the diameter of the holey region is ~75 μm and the diameter of the stripped MSF is ~230 μm. Scale bar is 100 μm.

The outer diameter of the fibres is similar to that of standard capillary dimensions, allowing facile coupling with external fluidic systems and components. When using standard capillary fittings and connections, the optical fibres can be used in fluidic applications without any modification. Independent of the microchip, we have demonstrated the utility of MSFs for CE,[19] open-tubular liquid chromatography,[20] and most relevantly, nano-electrospray ionization MS,[21] whereby sub-μL/min flow rates produce smaller charged droplets and hence greater sensitivity with less sample.[22] MSFs were found to be excellent ESI emitters, giving comparable signal intensity and stability as commercial tapered nanoESI emitters but without their tendency to clog. Coincidentally, the size of the holes in the MSF is on the order of 3-6 μm, suitable for retaining chromatographic packing material. In this way, the embedded nano-ESI emitter also functions as the retaining frit. Because the emitter and frit are the

same piece, which is integrated directly into the column on the microchip, the extra-column dead volume is minimized and fabrication is greatly simplified.

2.1.1 Materials and Fabrication Methods

There is a great variety of materials used for microchip manufacturing today, where most commonly glass, silicon and various polymers are used. Glass and silicon were the first materials to be used; both have somewhat similar mechanical properties, and most microfabrication techniques used in microelectronics can be transferred directly into manufacturing of microchips for chemical applications.[23] Both materials can be used to prototype well defined and reproducible features both in nano- and micro-scale.[7] They are resistant to most commonly used solvents for chromatography and MS, have negligible solvent swelling, and maintain stable channel architecture even after multiple uses. Glass is also optically transparent (including UV region), which allows simple optical on-chip detection with both UV and fluorescence. Silicon is opaque, thus optical detection methods are not applicable to it. Some disadvantages of using glass and silicon include initial price of these materials and their fragility; microfabrication methods for these materials also require cleanroom facilities and/or dangerous substances (HF),[24] which results in high manufacturing cost. Because of that, a cheaper and more versatile alternative was found in polymers.

Cost of polymer production is much lower; manufacturing techniques do not often require state-of-art facilities, thus overall price of the device is significantly reduced, and single use polymeric chips are common. There are, however, some common drawbacks for polymeric materials, including lower resolution of micro features, solvent instability, water swelling, and partial opacity in UV region. For example, some materials like polydimethylsiloxane (PDMS) show non-specific absorption of small and large bio-molecules, allow evaporation or gas permeability and can even leach un-crosslinked oligomers, thus creating interferences in detection.[25,26] However, due to their popularity, a variety of polymers have been developed, where a material with desired features can be easily selected for any particular application. Some common polymers used extensively in microchip technology

include PDMS, poly(methyl methacrylate) (PMMA), polycarbonate (PC), and currently becoming more and more popular cyclic olefin copolymer (COC).

COC is an excellent material for replication of miniature structures onto its surface; most studies have been dealing with micrometre sized features, however there have been reports of successfully implementing structures down to the tens of nanometres.[27] COC is stable in most polar solvents commonly used in chromatography and MS, it has very low water absorption (<0.01%) which allows multiple uses of same device with negligible channel swelling.[15,28,29] COC is also resistant to weak and strong acids, thus it can be effectively used in positive ESI-MS mode, which typically has some weak acid added to facilitate ion formation.[15] COC is transparent down to near UV region, thus optical detection and in-channel UV-polymerization is possible.[5] Currently several manufacturers offer COC, where somewhat different properties are observed depending on the grade.

2.2 Experimental

2.2.1 Materials

Acetonitrile (HPLC grade) and toluene were purchased from Fisher Scientific and used without further purification. Formic acid (analytical reagent, 98%) was obtained from BDH Chemicals (Toronto, ON, Canada). Leucine enkephalin (synthetic acetate salt), bradykinin acetate and insulin were purchased from Aldrich (Oakville, ON, Canada). Deionized water (>18 MΩ cm) was obtained from a Milli-Q Gradient water purification system (Millipore, Bedford, MA, USA). Red fluorescent 3.0 µm silica particles (PSi-R3.0) were obtained from Kisker Biotech GmbH & Co. KG (Steinfurt, Germany) and 3.5 µm Zorbax SB-C8 particles were purchased from Agilent (Wilmington, DE, USA). An aromatic drug candidate with the general structure **1** and fluoxetine (**2**) were kindly provided by Eli Lilly and Company (Indianapolis, IN, USA) (Fig. 2.2). The microstructured fibres with 54-hole pattern (LMA-PM-15) were purchased from NKT Photonics (Birkerød, Denmark). Fused silica capillaries (O.D. = 90 µm, I.D. = 20 µm; O.D. = 153 µm, I.D. = 74 µm; O.D. = 237 µm, I.D. = 102 µm; O.D. = 363 µm, I.D. = 74 µm) were purchased from Polymicro Technologies (Phoenix, AZ, USA).

1 **2**
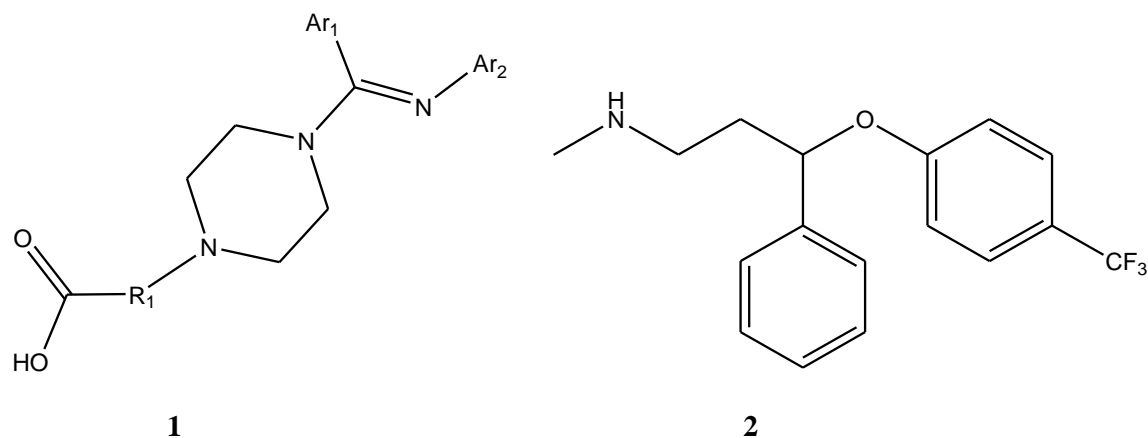
Figure 2.2: Structure of small drug molecules, 1 (proprietary drug candidate) and 2 (fluoxetine), successfully separated and detected on the microchip.

2.2.2 Microchip Fabrication

COC plates (COC-1420R, 150 x 150 x 2 mm and 150 x 150 x 1 mm) were obtained from Zeon Chemicals (Louisville, KY, USA) and cut to size (75 x 25 mm) using a mechanical punch. One of these sheets of COC was embossed with a capillary using a HEX-01 hot embosser from Jenoptik AG (Jena, Germany), which precisely controls the upper and lower plate temperatures and embossing force in an evacuated chamber. Capillaries having outer diameters of 90, 150, 230 or 360 μm were used for channel embossing, but only 150 μm and 230 μm O.D. capillaries produced functional chips. The glass transition temperature (T_g) of COC-1420R is 136 °C. To avoid direct contact of the steel press with the COC, flat, hard aluminum alloy plates (7075-T6, OnlineMetals, Seattle, WA, USA) were placed above and below the COC substrate. In the round channel formed by the embossed capillary, a 7 cm length of capillary having the same O.D. as the channel diameter was placed at one end (1.75 cm into the channel), to become the fluidic inlet to the chip. At the other end of the chip was placed a 2 cm piece of MSF (1.25 cm into the channel), to become the frit/emitter. The MSF was cut into 2 cm pieces using a fibre cleaver (FiTel, Furukawa Electric, Japan) with the acrylate coating on. The coating was removed prior to placing the MSF in the chip by soaking the cut MSF pieces in acetone for 5 min and manually stripping the coating off. Another piece of COC was placed on the substrate and thermally bonded to enclose the channel with the capillary and MSF embedded in it. To

prevent leaking of the chip around the capillary and fibre, the chips were further bonded with pieces of aluminium covering only the ends, ensuring the channel would not be blocked by keeping the pieces 1 mm from the open channel. As an added step to improve chip robustness at higher pressures, toluene was added to the edges to soften the polymer directly contacting the inlet capillary and outlet fibre, and the third bonding step was performed with plates only at the ends. Optionally, an annealing step was performed, whereby the chip was heated under contact force only, to better bond the cover plate to the substrate across the entire chip without deforming the channel features.[6,30] A schematic design of the chip from a side view, showing stepped ends due to second and third bonding steps, is shown in Fig. 2.3 along with a photograph of a completed chip.
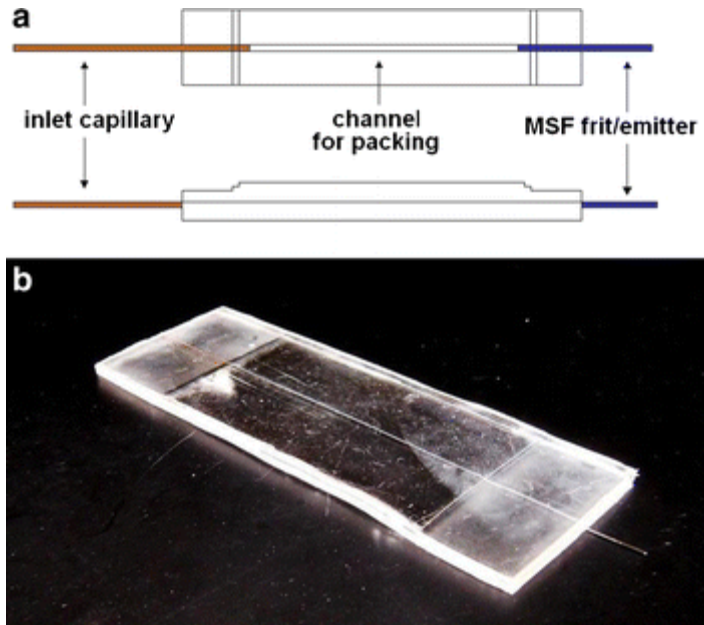
Figure 2.3: a) Schematic design of top and side view of the microchip, showing an inlet capillary, an open packing channel, a MSF having a dual role of a frit and an emitter, and two levels of depression on each side of the chip resulting from the second and third bonding steps; b) A photograph of an operational device with a 150 μm channel.

2.2.3 Microchip Packing

A slurry of commercial silica particles (Agilent 3.5 μm Zorbax SB-C8) was prepared in acetonitrile at 50-70 mg/mL and sonicated for 15 min to ensure full particle wetting by the solvent. The slurry was loaded into a small stainless steel tube and introduced into the chip using a

conventional HPLC pump. An ultrasonic cleaner (Fisher Scientific model FS110) was used during the packing process to help pack the beads more tightly, by fully immersing the microchip in the water. The column was packed until the bed was ~2 mm from the end of the inlet capillary. The chip was left connected to the pump with constant flow (only solvent) and sonication continued for 15 min to better pack the column. Following packing, the chip was examined with an optical microscope for quality of packing before use.

2.2.4 LC/MS Experiments

An Eksigent nanoLC pump (Livermore, CA, USA) was used to provide fluid flow for all separations and MS measurements. Mobile phases A (99% water, 1% acetonitrile, 0.1% formic acid) and B (99% acetonitrile, 1% water, 0.1% formic acid) were used for separations and for electrospray measurements. The capillary outlet from the nanopump was coupled with the inlet capillary on the microchip via a PEEK MicroTee (Upchurch Scientific/IDEX Health Sciences, Oak Harbor, WA, USA). Spray voltage was applied through a platinum wire inserted into the same MicroTee. The microchip was mounted on the x,y,z stage of the MS ion source (Proxeon, Odense, Denmark) using adhesive tape, and a CCD camera was used to monitor both the electrospray and position the emitter ~1.5 cm from the MS orifice. Mass spectra were recorded by an API 3000 triple-quadrupole mass spectrometer (MDS Sciex/Applied Biosystems, Concord, ON, Canada). Evaluation of electrospray performance and online detection of analytes were evaluated using the above set-up (Fig. 2.4).
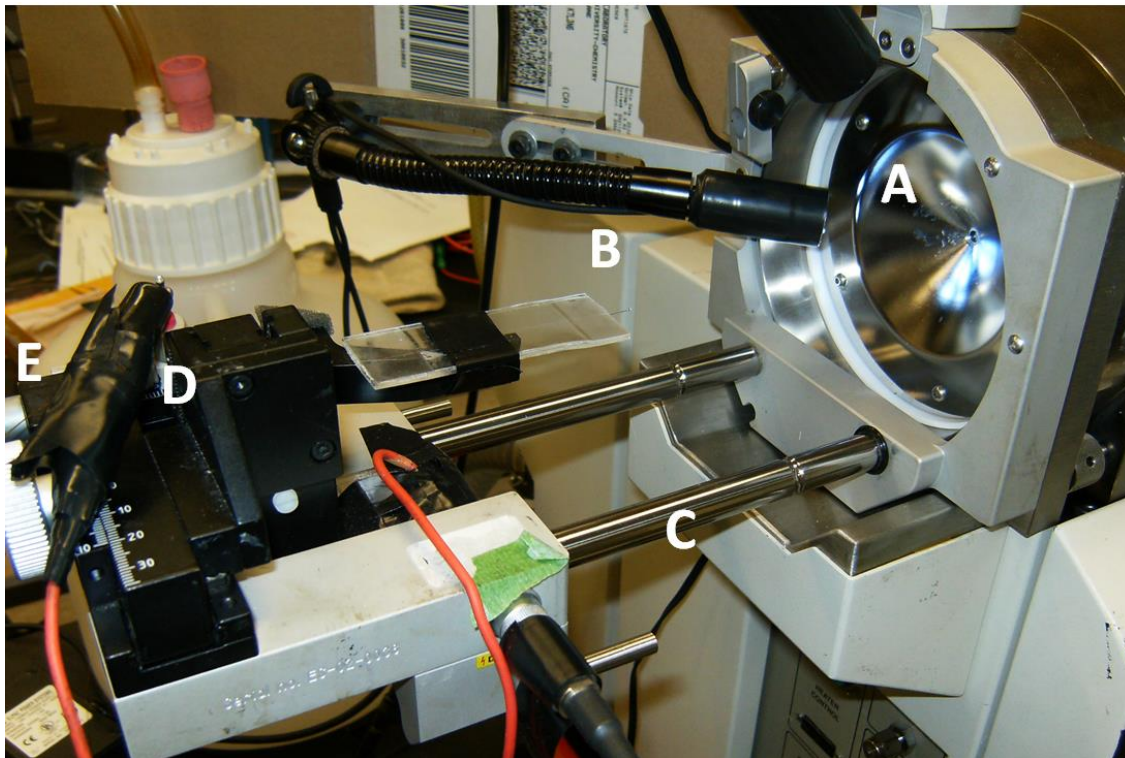
Figure 2.4: A photograph of the online monitoring set-up of LC/MS microchip separation and detection. A: MS orifice; B: MSF (emitter) of the microchip with the sample eluting from the tip; C: An x, y, z stage used to position the emitter next to the orifice; D: Ionization voltage applied through the liquid junction through the platinum wire; E: Connection to the Eksignet pump.

2.3 Results and Discussion

2.3.1 Microchip Fabrication

For LC/MS, the chip must be able to withstand the high pressures of particle packing, have a homogeneous, symmetrical channel for chromatography, and be resistant to chromatographic solvents such as acetonitrile, methanol and water. In the interests of the latter, the substrate material is the most important consideration. COC is particularly valuable in this regard for its stability in the presence of mid-to-high polarity solvents such as those used in reversed phase LC. It also has an accessible glass transition temperature and good embossing behaviour, making it very amenable to fabrication and thermal bonding using a hot embosser. Furthermore, COC is established as an embossing substrate in the literature and has documented ability to self-bond in the presence of non-polar solvents such as toluene and cyclohexane even under low temperatures.[31,32]

67

Sheets of COC commonly come in thicknesses of 1 mm and 2 mm. While 1 mm pieces behaved well under some conditions, the second and third embossing steps to help prevent leakage from around the inlet and outlet tended to cause the thinner sheets to bow, ultimately weakening the substrate/cover bond in the middle of the chip. Thus, for their added strength, 2 mm sheets were used in this study.

The shape and homogeneity of the channel are primarily determined by the initial embossing step. Because the stamp is simply a round capillary, the embossed channel is expected to have a round bottom, and at the ideal limit, perfectly vertical side walls. However, upon depressing the capillary into the COC surface, the surface dips near the capillary and does not reform around it, leaving a rounded edge on the channel. After bonding the cover plate, these rounded edges leave a space that runs the entire length of the channel; a cross section of the channel is shown in Fig. 2.5.
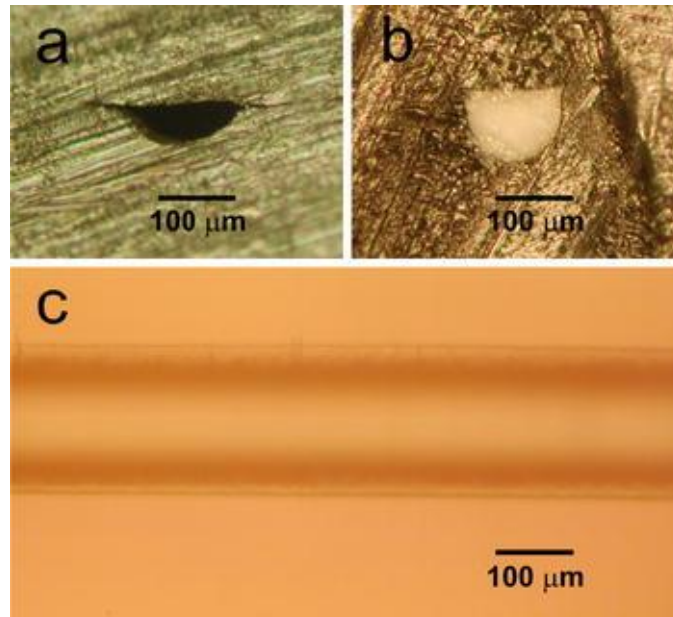
Figure 2.5: a) Photomicrograph of a cross section of an early microchip embossed with a 150-µm-O.D. capillary having significant space in the corner of the channel; b) Photomicrograph of a cross section of a more optimized microchip embossed with a 150-µm-O.D. capillary having minimal corner space; c) Photomicrograph of a packed 150-µm channel in a chip (top view). Note the regions at either side of the channel that are lighter due to less packing in the narrow spaces along the channel corners.

This artifact is not uncommon, and this behaviour in COC was previously demonstrated experimentally and simulated.[29] Such a space adds significant volume with more surface area than the bulk channel, causing different flow rates in these spaces (radial inhomogeneity of flow) and subsequently poorer separation efficiency and peak tailing when packed with stationary phase particles. The added dead volume in these spaces where packing cannot reach further due to finite particle diameter contributes to poor efficiency. Being thus undesirable, the extent of formation of the spaces was minimized by embossing the capillary under higher temperature and greater force for longer periods. The optimized parameters for this step were limited mostly by the ability of the substrate to maintain its shape under high temperature and force conditions. In addition to the embossing step, it was found that annealing the completed chip by heating it under contact force (~50 N) helped to reduce the actual size of the corner spaces, although the spaces were always present.

Perhaps the most limiting aspect of LC microchips is their inherently poor robustness to the high pressures required for flow through the packing material, especially during packing where high pressures are required to achieve a more even packing of particles.[33,34] For polymeric chips, the primary mode of failure under high pressure is leakage of the mobile phase at interfaces. The interface between the inlet capillary or outlet fibre and the polymer sheets is the weakest. To prevent such leakage at these junctions, bonding of the cover plate to the embossed substrate required optimization, and to this end several steps were added to the fabrication process. The initial bonding step was optimized for the highest temperature, force and time combination that stopped short of deforming the embossed channel, requiring a temperature below the T_g (136 °C). It should also be noted that keeping the mating surfaces dry and free of debris improved the quality of bonding. Unfortunately, however, in order to prevent channel deformation the bonding near the inlet and outlet was so weak that following the initial bonding step, the chip leaked with flow through the open channel, even in the absence of packing. A second bonding step was thus added, one where only the regions of the chip covering the inlet and outlet had force applied (indicated by the depressions on each end of the chip in Fig. 2.3). As

69

channel deformation was less of a concern in these regions, harsher bonding conditions could be employed, again optimized for stronger bonding without chip deformation, effectively closing the polymer around the tubing and preventing leaks. Because such chips were still not robust to high pressures, however, non-polar solvent was used to help soften the polymer at these interfaces to further improve bonding in these regions. For this step, toluene was applied to each end and allowed to wick into the interface, at which time a third bonding step was used to seal the ends more completely. The toluene could not be added after the initial bonding step, however, since it could wick all the way into the channel and cause blockage there, necessitating the third bonding step. After completing the bonding, annealing the chip as described in the experimental section provided further adhesion between COC plates and improved its robustness in the presence of applied pressure.

Packing the microchip was accomplished by coupling it to a HPLC pump which delivered a slurry of 3.5 μm beads into the chip under sonication. Optimized chips, prepared as described above, could be packed this way at pressures up to 100 bar without leaking. Microscope examination of the channels packed under this pressure with the aid of sonication revealed that channels were tightly packed with no observable voids. These examinations were repeated several times during regular microchip use, and the microchannel packing was apparently unchanged after multiple runs. During normal operation, flow-induced back pressure did not exceed 40 bar (600 psi), so leakage caused by high pressures is not a major problem. Indeed, microchips could be used repeatedly over several months without leaking. The failure mode for most chips was not leakage, and if a chip did not leak during its first use, it never failed by leaking. When leakage did occur, it typically came from the middle region of the chip, not from the extra-bonded ends.

2.3.2 Performance of the MSF as a frit

A successful frit should be strong, should retain the chromatographic particles completely and not significantly increase the back pressure of the system. From previous studies[36] it is known that short lengths of MSFs do not possess high flow-induced back pressure at the relatively low flow rates

employed in microfluidics, owing to the plurality of channels that combine to give a cross-sectional area equivalent to a 30 μm I.D. capillary.[19] Relative to the permeability of the packed bed, the frit should not add significant flow resistance.

The strength of the frit in the LC/MS chip is very good. Because the MSF resides embedded over 1 cm within the chip, the flow-induced pressure reached in this study does not cause the MSF to dislodge and chip failure has never occurred at the frit.

MSFs can be obtained with a variety of hole sizes and shapes.[21] For this study, the size of the holes in MSF is 3.8 ± 0.1 μm[20], making them suitable for retaining standard ~3 μm chromatographic particles. Indeed, the 3.5 μm Zorbax particles used in this study were observed to pack tightly against the frit with none observed in the channels of the MSF, and no packing material was lost during chip operation. Despite the individual particle size being small enough to fit within a hole of the MSF, the particles are retained by the so-called "keystone effect" whereby particles are forced together and against the walls or frit simultaneously, making them effectively much larger.[14] To confirm that no microspheres were entering the channels, commercial 3 μm particles functionalized with a red fluorescent dye were packed into the chip. Using a fluorescence microscope, no microspheres were observed anywhere in the channels. Furthermore, no MSF frit has been observed to clog.

While particles were not found to enter the MSF channels, they were able to get past the head of the MSF in some cases, similar to the image in Fig. 2.6.
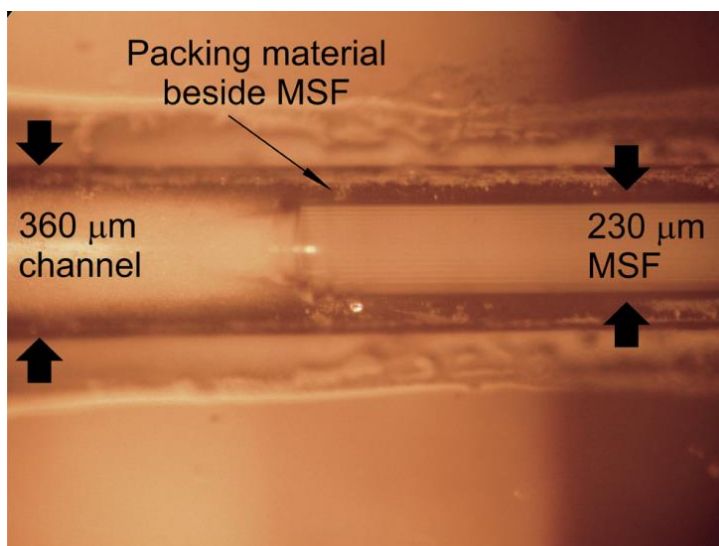
Figure 2.6: Photomicrograph of a MSF (having 168 holes) embedded in the channel of a chip embossed with a 360 μm O.D. capillary. In this case, the MSF is much smaller than the channel, causing packing material to enter the spaces that form beside the MSF frit.

In very early chips, with insufficient embossing in the first step, channels were wide near the channel/frit interface and packing material was observed beside the frit, but further optimization in fabrication protocols led to a channel with no such widening.

2.3.3 Performance of the MSF as a nanoESI emitter

MSFs have been previously shown in our group to be excellent nanoESI emitters that exhibit high spray stability (RSD < 5%) over a wide range of conditions.[21] In this study, the electrospray behaviour of the MSF was characterized while integrated in a polymeric LC/MS device, with voltage applied to a liquid junction before the chip inlet capillary. Taylor cone formation was visually monitored using a CCD camera and the signal was measured as a total ion current (TIC) while spraying mobile phase into the MS. Under isocratic mobile phase conditions, a range of solvent compositions from 0%-100% A (mobile phase compositions are described in the experimental section) were tested for 20 min periods. Presented in Fig. 2.7 is a series of TIC traces corresponding to various isocratic compositions at 300 nL/min and 500 nL/min flow rate.
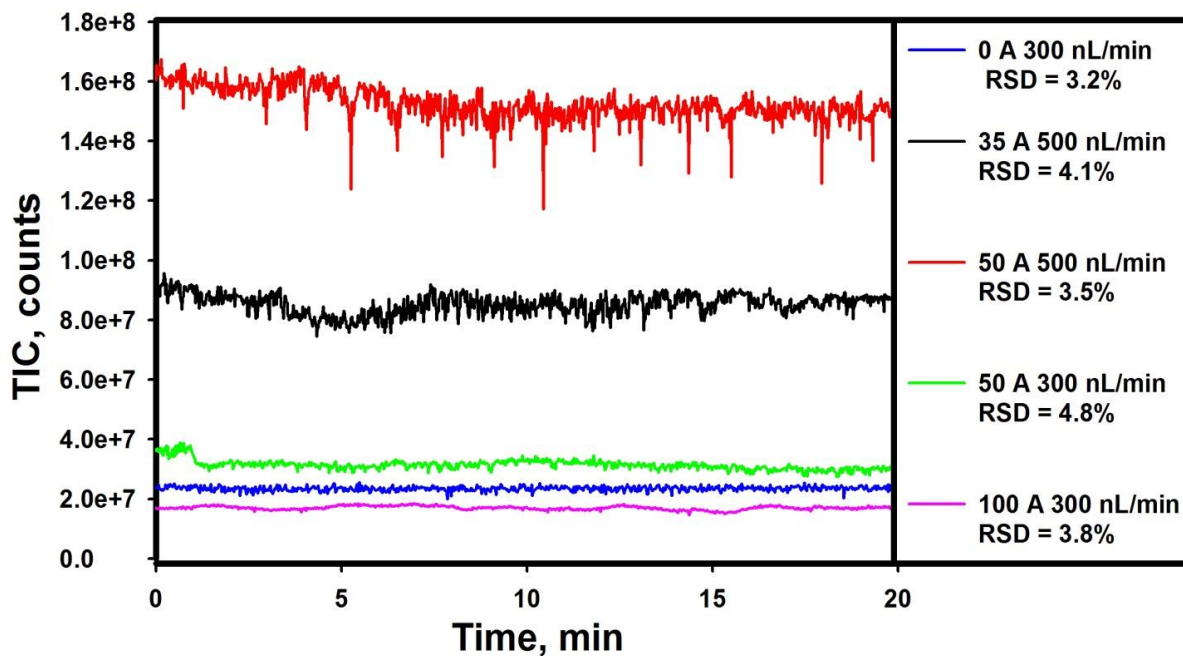
Figure 2.7: TIC traces at various flow rates (300 and 500 nL/min) and isocratic mobile phase compositions (from 0% A to 100% A), where all relative standard deviations are under 5%.

Electrospray at extreme solvent compositions is notoriously difficult,[35] but from this chip the signal is strong and consistent over a long period (≥20 min), and the stability of the signal is good (≤4.3% relative standard deviation). Furthermore, stable electrospray of 50% A mobile phase was achieved at flow rates over the range 10-500 nL/min, showing relative standard deviations (RSD) in the TIC traces of ≤10% in all cases. Indeed, at any solvent composition, conditions can be optimized (applied voltage, emitter position) to achieve stable spray within a minute. The typical range of applied voltage that leads to stable spray is 2.6-3.3 kV.

Electrospray behaviour is dependent on system properties such as solvent composition, applied voltage and emitter position, such that at a given position, a range of voltage will generate stable spray from a given liquid. When the mobile composition is constantly changing, as it is in solvent gradient LC, it is difficult to expect an emitter to behave well across the entire gradient under otherwise similar conditions.[36] To demonstrate the effectiveness of the LC/MS chip for gradient

73

separations, a complete solvent gradient from 100%-0% A was electrosprayed at the same flow rate and voltage over a 15 min time period, as shown in Fig. 2.8.
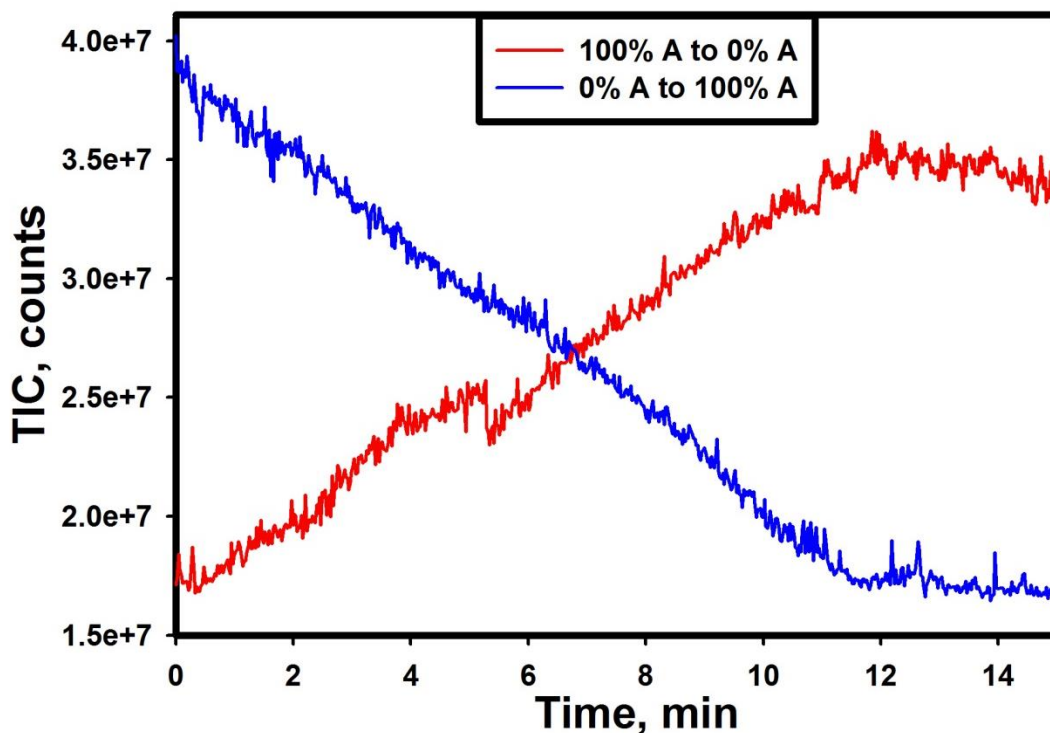
Figure 2.8: Evaluation of MSF performance as an ESI emitter for a gradient elution where solvent composition was constantly changing from 100% A to 100% B (and vice versa) over 15 minutes.

As expected, the TIC signal intensity gradually changed with a change in mobile phase, but the noise associated with the TIC signal was low at any given point in the gradient. The reverse experiment, a gradient from 0%-100% A in 15 mins, was also performed and the data is included in Fig. 2.6. The inverse TIC profile was observed for this gradient and exhibited similar stability.

2.3.4 LC Separation

The performance of the microchip as a separation device was evaluated by separating small drug molecules in isocratic elution mode and larger proteins in gradient elution mode. Column efficiency and peak shapes were used to evaluate the chromatographic performance of the micro-device. The exact length of the packed bed, however, could not be precisely controlled using our packing protocol and ranged from 3.8 to 4.5 cm. For this reason, retention times could not be reliably

compared between chips. For the same chip, however, between runs on the same day, retention time reproducibility was typically less than 4% RSD for the isocratic elution of the Eli Lilly compound **1** at 300 nL/min of 65% A mobile phase. From day to day, the retention time reproducibility was <6% RSD.

LC/MS chips were prepared with different channel sizes arising from embossing different size capillaries in the embossing step. In this study, capillaries with outer diameters of 90 μm, 150 μm, 230 μm and 360 μm were used to prepare chips. The smallest channels, using the 90 μm O.D. capillary, did not lead to functioning chips because the region of the 54-hole MSF containing most of the openings did not align with the imprinted channel, i.e. most of the holes in the MSF were positioned above the embossed LC channel. The largest channel, using the 360 μm O.D. capillary, provided a significant mismatch with the size of the MSF, leaving a taper near the channel/frit interface that introduced dead volume and allowed packing material to be deposited beside the frit. The chromatographic performance of chips made using 150 μm and 230 μm O.D. capillary, where the channel had similar dimensions to the embedded MSF, was evaluated in more detail.

A typical isocratic separation of two small-molecule drugs in a 150 μm channel LC/MS chip is shown in Fig. 2.9 top.
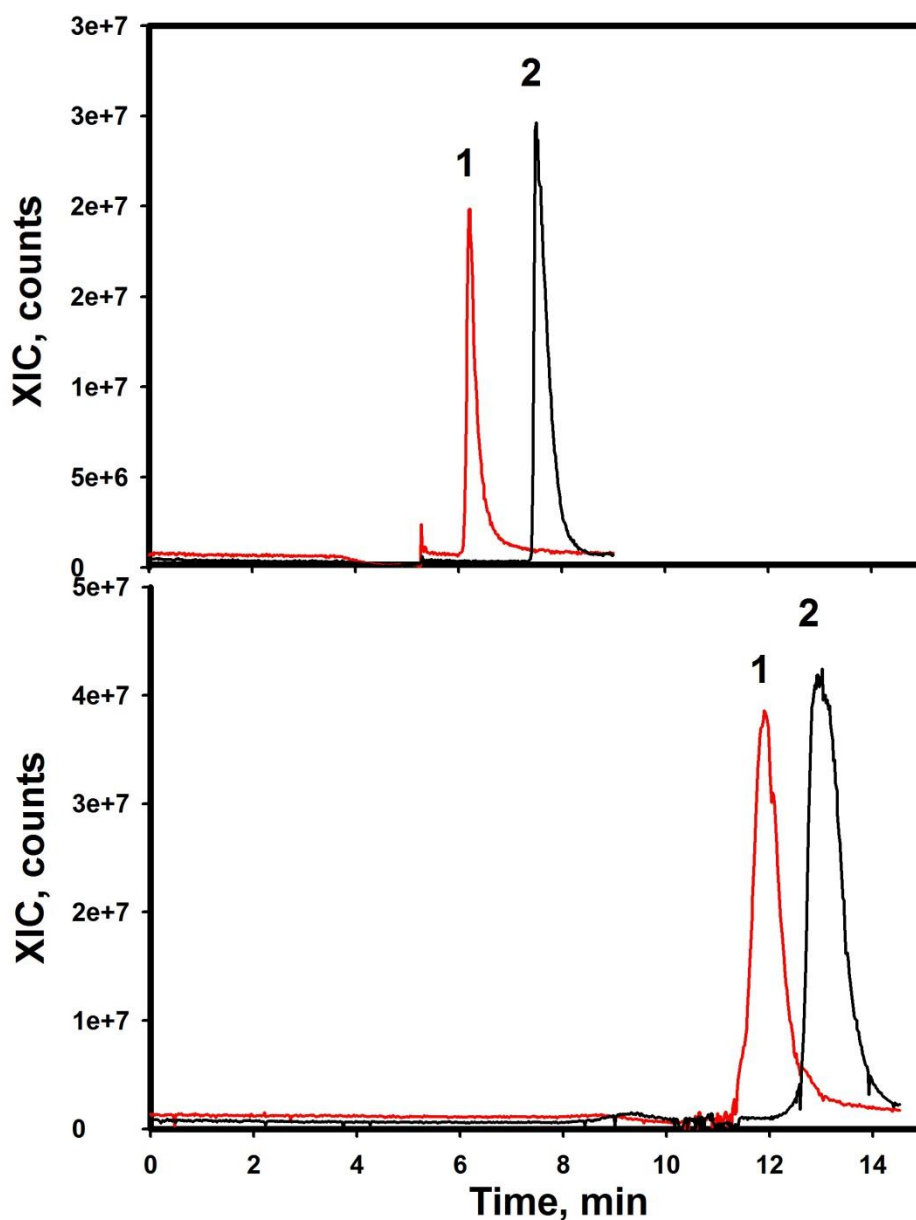
Figure 2.9: Extracted ion current (XIC) traces showing the on-chip isocratic separation of two small Eli Lilly drug molecules (1 (*m/z* = 379.9 (M+H$^+$), and 2 (*m/z* = 310.3 (M+H$^+$). Top: a 150-μm channel design using 65% A mobile phase at 300 nL/min (300 nL injection of an aqueous mixture of 5 μM each). Bottom: a 230-μm channel design using 60% A mobile phase at 500 nL/min (500 nL injection of an aqueous mixture of 5 μM each) with ESI detection.

While the peaks are fully resolved, it is clear that significant tailing is present. As described above and shown in Fig. 2.5, the shape of the channel in the microchip is not ideally round, but instead contains spaces in the corner where the substrate and cover plate meet. These spaces provide

76

alternative flow pathways and dead volume in which analytes can lag, contributing to peak tailing. These spaces were observed for both 150 μm and 230 μm channels, but the peak tailing for the larger channel was not as pronounced (see Fig. 2.9 bottom). The extent of the asymmetry of the peaks was determined by calculating the asymmetry factor (A_s), which is the ratio of the right to the left parts of the peak at 10% of the peak height (Eqn. 2.1), where t_R is retention time, t_{right} is time at 10% peak height on the right side of the peak and t_{left} is time at 10% peak height on the left side).[37]

$$A_s = \frac{t_{right} - t_R}{t_R - t_{left}}$$

Equation 2.1

For the 150 μm channel, the asymmetry factor for the isocratic elution of **1** under the conditions in Fig. 2.9 top was 4.0 ± 0.4 and for **2** it was 6.1 ± 0.3. For the 230 μm channel, the asymmetry factors for **1** and **2** were 1.7 ± 0.4 and 2.6 ± 0.4, respectively, under the isocratic conditions in Fig. 2.9 bottom. This difference in peak symmetry for the different sized channels can be attributed in part to the relative contribution of the aforementioned corner spaces to the channel shape in each case. While these regions of reduced flow in the 150 μm channel occupy less space than those in the 230 μm channel, they are deeper, leading to slower mass transfer in and out of the regions. Additionally, the greater surface area-to-volume ratio for the 150 μm channel increases the influence of the hydrophobic COC walls on the retention of the analytes, further leading to peak tailing. Indeed, unmodified COC has been used as a stationary phase in reversed phase chromatography.[38] To exacerbate these issues, mass transfer between the channel and the corner spaces/wall has a greater effect on the peaks in Fig. 2.9 top because the linear velocity of the mobile phase is greater than in Fig. 2.9 bottom under the conditions used.

With regard to band broadening, the column efficiency was calculated using the conventional formula for theoretical plates with peak width taken at half the peak height. For the 150 μm channel, the column efficiency calculated for the isocratic elution of fluoxetine under the conditions in Fig 2.9 top was $113\,000 \pm 7\,000$ theoretical plates per metre, and for the 230 μm channel it was $59\,000 \pm$

3 000 plates/m under the conditions in Fig. 2.9 bottom. The theoretical plate number achieved is lower than that of a commercially available column packed with the same 3.5 µm C-8 particles.[39] This is expected, as the commercial columns have optimized circular channel geometry, and can withstand higher pressures. However, when compared with PPM-based microfluidic device, more than four times the number of theoretical plates is achieved (113 000 plates/m vs. 25 000 plates/m) on a 150 µm channel device.[40] The difference in efficiency can be attributed to the larger volume occupied by the regions of reduced flow in the 230 µm channel. For this larger channel, the corner spaces contributed to a much greater overall channel deformation, causing a wider distribution of flow paths and consequently broader peak shape. The differences may also arise from poor packing near the wall in these channels. The so-called wall effects of particle packing describe the ordered packing structure of spheres against a hard flat surface, which causes increased void volume between particles for several particle-lengths into the packing bed. It has recently been studied in some detail[41] and it was found that the wall effects were worse for larger channels in a similar size range as those in the current study. The increased corner spaces in our larger channels cause further packing inhomogeneities as the particles in these regions are not well packed, leading to poorer column efficiency.

The quality of the LC/MS chromatogram is dependent on the intensity and stability of the electrospray signal, which is in turn dependent on several parameters, one of the most important being solvent composition. To demonstrate the ability of our polymer LC/MS chips to perform in gradient mode separations, where solvent composition can change significantly within a few minutes, a gradient separation of three proteins in a 150 µm channel is shown in Fig. 2.10.
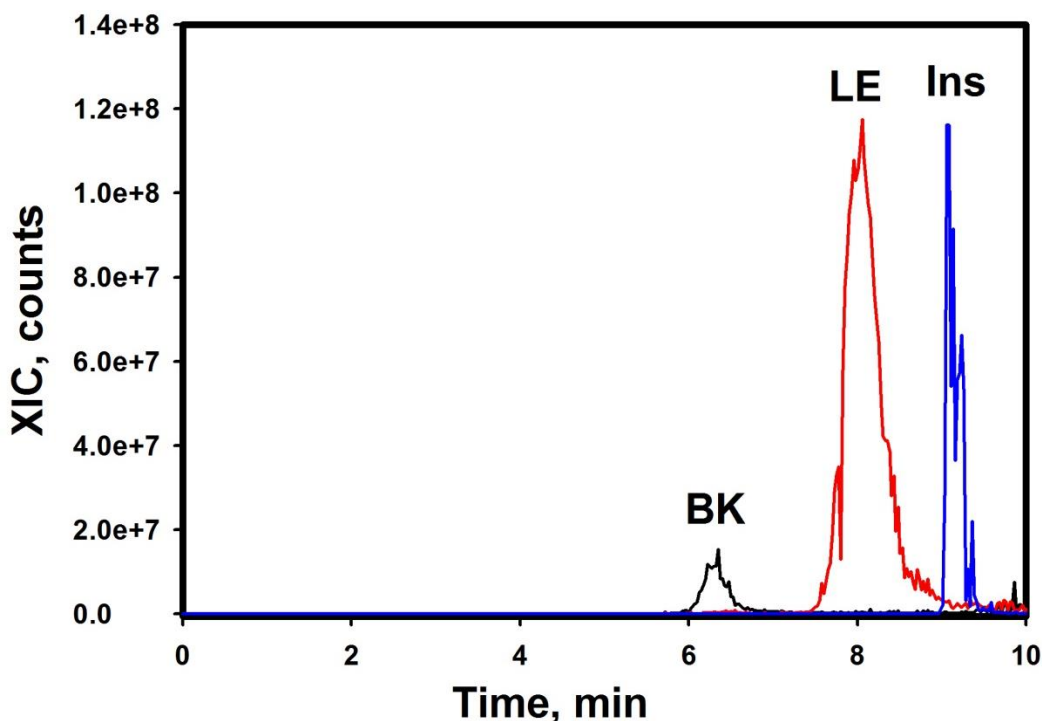
Figure 2.10: Extracted ion current traces showing the on-chip gradient separation of three peptides ((bradykinin, BK (m/z = 531.2 $(M + 2H)^{2+}$); leucine enkephalin, LE (m/z = 556.3 $(M + H)^{+}$); and bovine insulin, Ins (m/z = 1,147.9 $(M + 5H)^{5+}$)) in a 150-µm-channel design. Gradient conditions: 99 –70 % A in 9 min, then 70–30 % A in 1 min at 300 nL/min with ESI detection. Injection: 500 nL of an aqueous mixture of 5 µM each.

With decreasing polarity, bradykinin, leucine enkephalin and insulin were separated in ten minutes using a complex gradient from 99% to 70% A in 9 min, then from 70% to 30% A in 1 min to focus the insulin peak. Similar to the isocratic elution conditions, the added dead volume in the reduced-flow side regions of the channel contributes to broadened and asymmetric peaks. Nevertheless, the successful separation of these bio-molecules under gradient elution demonstrates the chip's chromatographic versatility.

2.4 Conclusion

Overall, a simple and inexpensive microfluidic device with a packed reversed phase separation channel was fabricated featuring an integrated MSF serving dual functions as a frit and an electrospray emitter. The rapid prototype device required only a few simple steps to be fabricated by hot embossing and was able to withstand pressures of up to 100 bar. The same device could be used for several

months (weekly use) without significant change in separation efficiency or electrospray stability. The most significant drawback of the proposed design is a result of the thermo-elastic properties of the substrate material during the embossing step that results in deep corner regions along each side of the channel after bonding. These spaces contribute to dead volume and ultimately peak broadening and tailing. The dual functionality of the integrated MSF as a frit and emitter results in less post-column dead volume and simplifies coupling to MS detection. The geometry and size of the features in the MSF are very suitable for retaining particles ≥3 μm and for use as a robust electrospray emitter, integrating well with the channel in an embossed LC/MS chip.

2.5 References

1.   T. Sikanen, S. Franssila, T. J. Kauppila, R. Kostiainen, T. Kotiaho and R. A. Ketola, *Mass Spectrom. Rev.*, 2010, **29**, 351-91.

2.   Q. Lu and G. E. Collins, *Lab Chip*, 2009, **9**, 954-60.

3.   A. Ishida, M. Natsume and T. Kamidate, *J. Chromatogr., A*, 2008, **1213**, 209-17.

4.   S. Gotz and U. Karst, *Anal. Bioanal. Chem.*, 2007, **387**, 183-92.

5.   M. F. Bedair and R. D. Oleschuk, *Anal. Chem.*, 2006, **78**, 1130-8.

6.   Y. Yang, C. Li, J. Kameoka, K. H. Lee and H. G. Craighead, *Lab Chip*, 2005, **5**, 869-76.

7.   D. Mijatovic, J. C. T. Eijkel and A. van den Berg, *Lab Chip*, 2005, **5**, 492-500.

8.   X. C. Wang, X. H. Yang and X. M. Zrang, *Anal. Sci.*, 2006, **22**, 1099-104.

9.   Q. Lu and G. E. Collins, *J. Chromatogr., A*, 2010, **1217**, 7153-7.

10.   G. A. Lord, D. B. Gordon, P. Myers and B. W. King, *J. Chromatogr., A*, 1997, **768**, 9-16.

11.   R. D. Oleschuk, L. L. Shultz-Lockyear, Y. Ning and D. J. Harrison, *Anal. Chem.*, 2000, **72**, 585-90.

12.   M. W. Toepke and D. J. Beebe, *Lab Chip*, 2006, **6**, 1484-6.

13.   R. Mukhopadhyay, *Anal. Chem.*, 2007, **79**, 3248-53.

14.   A. Gaspar, M. E. Piyasena and F. A. Gomez, *Anal. Chem.*, 2007, **79**, 7906-9.

15. P. S. Nunes, P. D. Ohlsson, O. Ordeig and J. P. Kutter, *Microfluid. Nanofluid.*, 2010, **9**, 145-61.

16. A. Arora, G. Simone, G. B. Salieb-Beugelaar, J. T. Kim and A. Manz, *Anal. Chem.*, 2010, **82**, 4830-47.

17. S. Koster and E. Verpoorte, *Lab Chip*, 2007, **7**, 1394-412.

18. P. Russell, *Science*, 2003, **299**, 358-62.

19. B. Rogers, G. T. T. Gibson and R. D. Oleschuk, *Electrophoresis*, 2011, **32**, 223-9.

20. A. B. Daley, R. D. Wright and R. D. Oleschuk, *Anal. Chim. Acta*, 2011, **690**, 253-62.

21. S. Su, G. T. T. Gibson, S. M. Mugo, D. M. Marecak and R. D. Oleschuk, *Anal. Chem.*, 2009, **81**, 7281-7.

22. M. Wilm and M. Mann, *Anal. Chem.*, 1996, **68**, 1-8.

23. G. M. Whitesides, *Nature*, 2006, **442**, 368-73.

24. R. T. Kelly, J. S. Page, Q. Z. Luo, R. J. Moore, D. J. Orton, K. Q. Tang and R. D. Smith, *Anal. Chem.*, 2006, **78**, 7796-801.

25. X. F. Sun, R. T. Kelly, K. Q. Tang and R. D. Smith, *The Analyst*, 2010, **135**, 2296-302.

26. E. W. K. Young, E. Berthier, D. J. Guckenberger, E. Sackmann, C. Lamers, I. Meyvantsson, A. Huttenlocher and D. J. Beebe, *Anal. Chem.*, 2011, **83**, 1408-17.

27. N. Gadegaard, S. Mosler and N. B. Larsen, *Macromol. Mater. Eng.*, 2003, **288**, 76-83.

28. F. Bundgaard, G. Perozziello and O. Geschke, *Proc. Inst. Mech. Eng., C-J Mech.*, 2006, **220**, 1625-32.

29. R. K. Jena, S. A. Chester, V. Srivastava, C. Y. Yue, L. Anand and Y. C. Lam, *Sensor. Actuat. B-Chem.*, 2011, **155**, 93-105.

30. X. Illa, W. De Malsche, J. Bomer, H. Gardeniers, J. Eijkel, J. R. Morante, A. Romano-Rodriguez and G. Desmet, *Lab Chip*, 2009, **9**, 1511-6.

31.   T. I. Wallow, A. M. Morales, B. A. Simmons, M. C. Hunter, K. L. Krafcik, L. A. Domeier, S. M. Sickafoose, K. D. Patel and A. Gardea, *Lab Chip*, 2007, **7**, 1825-31.

32.   D. A. Mair, M. Rolandi, M. Snauko, R. Noroski, F. Svec and J. M. J. Frechet, *Anal. Chem.*, 2007, **79**, 5097-102.

33.   D. A. Mair, E. Geiger, A. P. Pisano, J. M. J. Frechet and F. Svec, *Lab Chip*, 2006, **6**, 1346-54.

34.   S. Roy, C. Y. Yue, S. S. Venkatraman and L. L. Ma, *J. Mater. Chem.*, 2011, **21**, 15031-40.

35.   M. Karas, U. Bahr and T. Dulcks, *Fresen. J. Ana.l Chem.*, 2000, **366**, 669-76.

36.   S. Jung, U. Effelsberg and U. Tallarek, *Anal. Chem.*, 2011, **83**, 9167-73.

37.   J. P. Foley and J. G. Dorsey, *Anal. Chem.*, 1983, **55**, 730-7.

38.   O. Gustafsson, K. B. Mogensen and J. P. Kutter, *Electrophoresis*, 2008, **29**, 3145-52.

39.   Zorbax® HPLC column specification datasheet, *Brechbuhler Scientific Analytical Solutions*. [Online]. Available: https://www.brechbuehler.ch/fileadmin/redacteur/pdf/columns-sampleprep/lc-columns/zhzor.pdf [Accessed: March 31, 2016]

40.   D. S. Reichmuth, T. J. Sheppod and B. J. Kirby, *Anal. Chem.*, 2005, **77**, 2997-3000

41.   S. Bruns, J. P. Grinias, L. E. Blue, J. W. Jorgenson and U. Tallarek, *Anal. Chem.*, 2012, **84**, 4496-503.

Chapter 3

Electrowetting on Superhydrophobic Natural (*Colocasia*) and Synthetic Surfaces Based Upon Fluorinated Silica Nanoparticles

3.1 Introduction

Superhydrophobic surfaces are a subject of great interest due to their unique water-repellent properties that have found utility in many applications. Superhydrophobic surfaces are characterized as having both a water contact angle (WCA) above 150° and a very low roll-off angle (ROA), below 10°.[1-4] The superhydrophobic properties of a surface are attributed to the combination of a material's surface geometry and chemical composition. Surface roughness on both micrometre and nanometre scales causes air to be entrapped between the surface and the water droplet, referred to as a Cassie-Baxter state.[5] An appropriate chemical composition (e.g. significant fluorination) can further lower the surface energy of the material.[6-8]

Superhydrophobic materials possess unique properties such as self-cleaning, anti-icing[3] and anti-fouling,[9] which have been adapted to a number of applications including manufacturing stain-repellent textiles,[10] anti-biofouling coatings for marine applications,[7] water/ice-resistant paints,[4] etc. Recently, there has been significant interest in implementing superhydrophobic coatings into digital microfluidics (DMF). DMF has emerged as an alternative to traditional "continuous flow" microfluidic approaches, where individual droplets can be independently controlled in a pre-determined fashion. DMF offers other advantages of "in-channel" microfluidics, such as high analysis speed, specificity, small sample size and limited waste production, precise control, and the variety of sample preparation strategies that can be implemented and multiplexed on a single device.[11-14] Furthermore, DMF devices do not require the more complicated fabrication procedures associated with some channel-based devices, e.g. pumping systems, valves etc. DMF relies on the discrete and precise control of the individual droplets of various sizes, where droplets can be moved, split, merged

and mixed on a small platform.[15-18] Different approaches are used to discretely move droplets on the surface, including electrowetting-on-dielectric (EWOD),[19,20] dielectrophoresis,[21] acoustic wave,[22] and magnetic actuation,[23,24] EWOD is currently the most commonly used methodology with DMF devices, where the droplet actuation results from a shift in the distribution of electrohydrodynamic forces due to an applied voltage, leading to the reduction in the CA between a droplet and the surface.[11,25-27] There are several required design elements for EWOD-based devices including individual electrodes for droplet manipulation coated with a dielectric layer for charge accumulation and a hydrophobic top layer. A higher initial WCA often requires lower voltage to initiate droplet movement, thus highly hydrophobic surfaces are commonly employed in DMF devices.[28] The most popular hydrophobic layer used is Teflon® AF, which although common, has limitations. The contact angle of Teflon with water is ≈ 120°, which renders the surface sufficiently hydrophobic for droplet manipulation, however the surface coating is not very robust or durable, and simple operations can remove Teflon from the surface of the device.[29,30] Teflon is also sensitive to other commonly used solvents, and has reported biofouling which limits the number of uses per single device.[31,32] Clearly, there is a need for an enhanced, more robust material.

An inspiration for many synthetic superhydrophobic surfaces comes from those that occur naturally, *i.e.* plant leaves like lotus (*Nelumbo*) or elephant ear (*Colocasia*).[2] Extensive studies on these surfaces show that they have an optimal combination of surface roughness, arising from microbumps formed by convex surface papillae, and low surface energy, resulting from the formation of a crystalline wax film, to create a superhydrophobic surface.[7,33]

In this chapter a series of hydrophobic and superhydrophobic materials for EWOD applications are explored, which are based upon fluorinated silica nanoparticles (FSNP) of various sizes and fluorine composition. This material is stable, robust and may be adapted for EWOD applications. The EWOD properties of FSNP coatings on a simple device are compared to the EWOD performance with a natural surface, *Colocasia* leaf.

3.2 Methods and Materials

3.2.1 Materials

Deionized water (Fisher Scientific, Ottawa, Canada) mixed with various proportions of acetonitrile and methanol was used to form droplets on different surfaces. Acetonitrile, methanol, ethanol, absolute ethanol and ammonia were purchased from Fisher Scientific (Canada); trifluorotoluene (TFT) and tetraethoxysilane were purchased from (Sigma Aldrich, MO, US). Glass microscope slides (Fisher Scientific, $76 \times 25 \times 1.0$ mm^3) were used as the device substrate. Surfaces used in this study were selected based on varying level of hydrophobicity. Teflon® AF (DuPont™) was used as a reference as it is a standard hydrophobic surface coating used for DMF devices. It was spin coated with a Laurell WS-650 spin coater (North Wales, PA, USA) using a two-step process: 500 RPM for 10 seconds and 3000 RPM for 30 seconds. The measured thickness of the coating was about 150 nm.[34] Natural superhydrophobic surfaces (*Colocasia* plant leaves) were grown locally and harvested when leaf sizes were >30 cm diameter. The leaves were used either within hours of being harvested, or dried after being attached to the substrate to prevent curling. Leaf materials (fresh and dried) were adhered to the dielectric surface using double-sided adhesive tape, taking care to ensure that the leaf surface was as flat as possible. Ultra-Ever Dry® (UED) was purchased from Hazmasters (Ottawa, Canada) as a two-part coating, a base coat (adhesive) and top coat, which contained the FSNPs.

3.2.2 Silica Nanoparticle Synthesis

Bifunctional silica particles were synthesized by a modified Stöber method.[35] In a typical synthesis to produce 90 nm particles the following procedure was used. Initially, the solvent (9.0 mL of absolute ethanol) was mixed with water (1.6 mL 18 MΩ) and ammonia (2.5 mL 2 M in ethanol) and left to stir at 60 ^{o}C for 30 min. Then tetraethoxysilane 2.2 mL (~2.0 g) was added to start the synthesis of the silica particles. The mixture was left to stir at 60 ^{o}C overnight. The ammonia concentration was

changed to synthesize the silica particles with different sizes (i.e. 5-10 nm, 25-30 nm and 125-150 nm).

The functionalization agents, 2-(perfluorooctyl)ethyl triethoxy silane (Sigma Aldrich, MO, US) and *N*-(6-aminohexyl)aminomethyl-triethoxysilane (Gelest, PA, US) were then added and the heating was continued for another 2 hours. In all preparations, a total of 100 µL of functionalization agents were used, respectively. The particles were recovered by centrifugation (3900 RPM). The particles were then purified by dispersion in methanol (25 mL) and centrifuged (3900 RPM) before the supernatant was removed. The particles were then re-dispersed in TFT (25 mL) and centrifuged (3900 RPM) to remove the supernatant. The particles were finally re-dispersed in methanol (25 mL) and centrifuged (3900 RPM) for supernatant removal. Using the above protocol, particles with the volume fractions of 0 %, 10 %, 25 %, 50 %, 75 % and 90 % for 2-(perfluorooctyl)ethyl triethoxy among the two surface functionalization agents (with the diameter of 85-90 nm) were synthesized and characterized with SEM.

3.2.3 EWOD Testing

A prototypical EWOD device was prepared using a standard glass microscope slide which served as the device substrate. Adhesive single-sided copper tape (thickness ~ 34 μm) was cut and attached to the cleaned glass slides to serve as electrodes. Double-sided adhesive tape (thickness ~ 164 μm) was used as a dielectric layer which had a hydrophobic/superhydrophobic layer deposited on top of it. FSNP-based superhydrophobic coatings were either deposited by droplet casting ("casted FSNP") or by aero-spraying ("sprayed FSNP"). For the "casted FSNPs", a droplet of suspended nanoparticles (in TFT) was deposited over a dielectric layer and the extra solvent was allowed to evaporate for at least 30 minutes. The samples were then further dried in the oven at 120° for 15 minutes. With this method an excess of liquid is deposited on the surface, to make sure that the whole surface is evenly coated. For the "sprayed" method the FSNPs solution (in TFT) was aero-sprayed using a house-built device directly onto the dielectric surface, where no further evaporation was

required.[36] The samples still needed to be dried in the oven at 120° for 15 minutes to ensure good adhesion.

The commercial FSNP surface (UED) was deposited using chromatographic sprayer, as recommended by manufacturer. Briefly, both base and top coats were applied with a thin-layer chromatography sprayer. The base coat was sprayed twice over the clean glass slide surface and air dried in a fume hood for 20 minutes at ambient temperature. Similarly, two layers of the top coat were uniformly sprayed over the dried surface of base coat and then air dried in the fume hood for at least two hours before use.

All EWOD experiments were performed on an "open-top" device configuration, where the DMF microchips were placed inside a custom-made draft-reducing box to prevent droplet movement due to air currents within the laboratory (Fig 3.1).
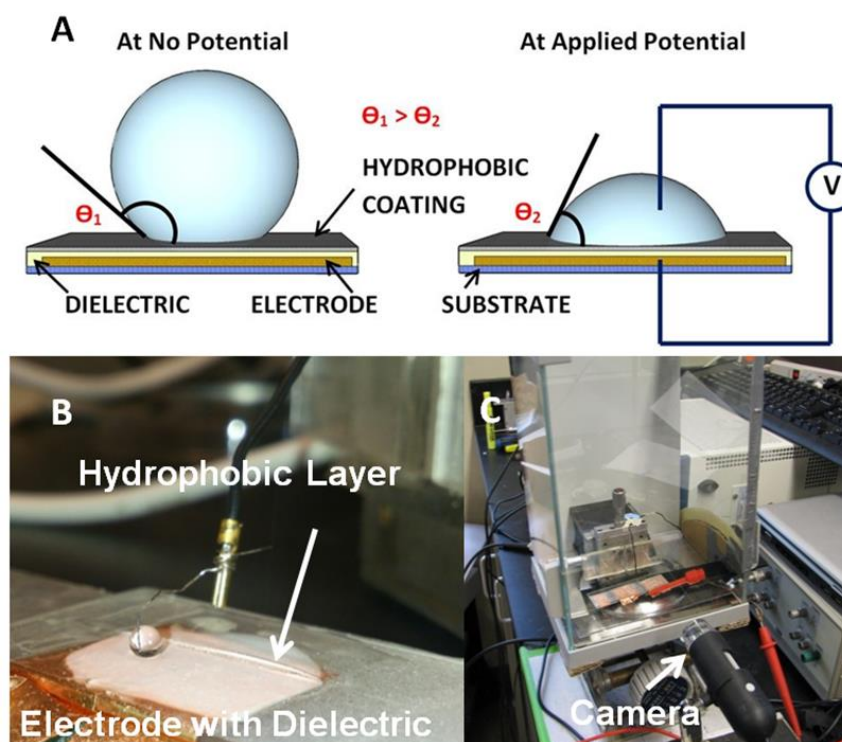
Figure 3.1: A) Schematic of an "open-top" style device; B) photograph of the working device coated with synthesized FSNPs; C) experimental set-up, where the EWOD device was placed inside the draft-reducing box, and a USB camera was setup to take images for the measurement of CA.

3.2.4 DMF Device Fabrication

Several device designs and manufacturing approaches to DMF device fabrication were explored. Early prototype design was based on printed circuit board (PCB) technology, however the device was not functional as discussed in section 3.3.5. A fully functional DMF device was fabricated using a standard lithographic approach, as described further below.

3.2.4.1 PCB Microchip Design

PCB DMF device was kindly provided by CMC microsystems, obtained from a commercial PCB manufacturer, where a standard multilayer printing approach was used. The design was developed to include various configurations of copper electrodes – i.e. spacing and shape; pads of various sizes were also implemented. Fig. 3.2 demonstrates the final fabrication design.
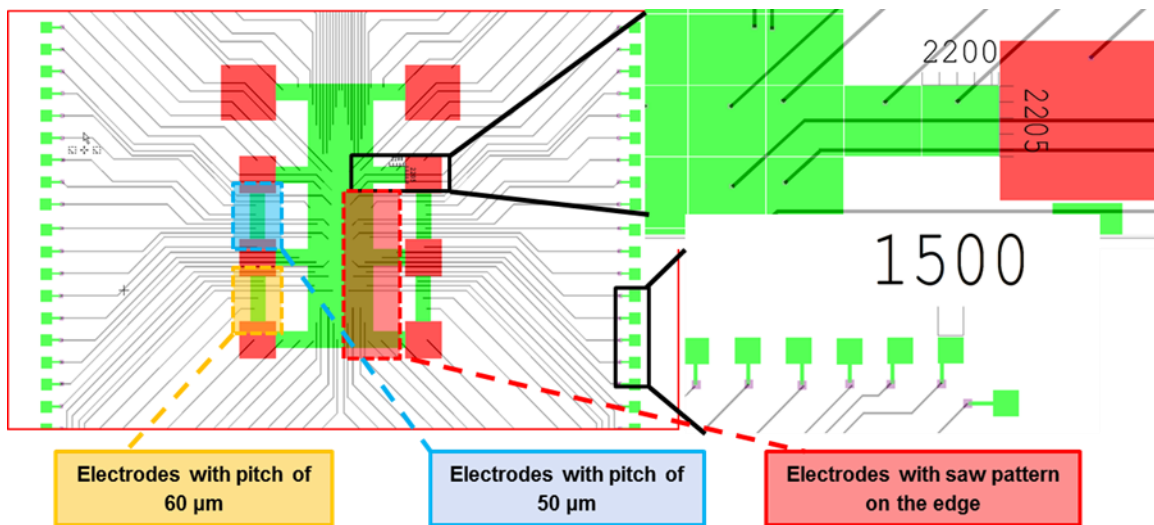
Figure 3.2: Schematic design of PCB microchip, where electrode spacing, size and shape were varied.

The size of the PCB substrate is 10.0 cm by 10.0 cm. Electrodes are 2.2 mm x 2.2 mm, where the standard gap between them is 40 μm, unless specified otherwise. Additional designs include 2.0 mm x 2.0 mm electrodes with 50 μm gap (blue area in Fig. 3.2) and 2.0 mm mm x 2.0 mm electrodes with 60 μm gap (orange area in Fig. 3.2). Two large pads are 7.5 mm x 7.5 mm with 40 μm gap, and six smaller pads are 5.0 mm x 5.0 mm with corresponding gap distance (colour-coded from Fig. 3.2). The electrodes are defined by a green pattern, pads are red and the grey lies are the copper connections

on the backside of the chip. The control pads (1.5 mm x 1.5 mm) on the outside of the chip are wired to the copper electrodes/pad where the droplets are positions, and by applying voltage to the control pads the droplets can be actuated on the inside of the device. The device was then coated with ~ 14 μm of Parylene-C by vapour deposition, and further coated by either Teflon® AF or FSNPs. Fig. 3.3 shows photograph a fabricated PCB EWOD-DMF device.
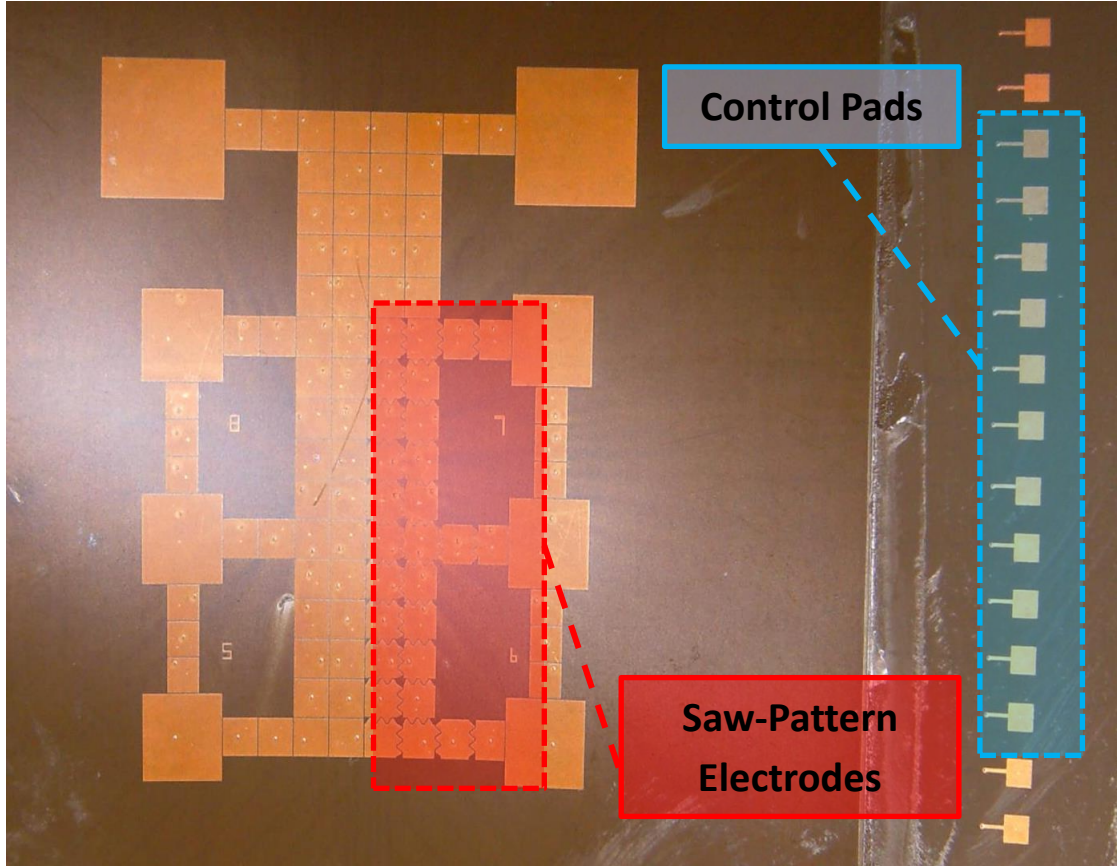
Figure 3.3: A photograph of a EWOD-DMF PCB microchip, coated with Parylene-C and Teflon® AF.

3.2.4.2 Photolithographic Fabrication Method

Droplet actuation was tested on a DMF device fabricated in the University of Toronto Nanofabrication Centre (TNFC) cleanroom facility using photolithographic methods described previously.[37] Device fabrication reagents included photoresist developer MF-321 from Rohm and Haas (Marlborough, MA), chromium etchant CR-4 from Cyantek (Fremont, CA), photoresist stripper AZ-300T from AZ Electronic Materials (Somerville, NJ), Teflon® AF from DuPont (Wilmington,

DE) and Parylene C dimer from Specialty Coating Systems (Indianapolis, IN). DMF devices consisted of an array of 80 interdigitated working electrodes (2.2 mm x 2.2 mm) connected to 10 larger reservoir electrodes (4.5 mm x 4.5 mm). Glass substrates (49.5 mm x 74.2 mm x 1.1 mm) coated with chromium (200 nm) and photoresist from Telic Co. (Santa Clarita, CA) were exposed to UV from a Suss MicroTec mask aligner (29.8 mW/cm^2, 10 seconds) under an acetate photomask printed at 20,000 dpi (Pacific Arts and Designs, Inc, Markham, ON). The exposed substrates were then developed in MF-321 (3-5 min.) and baked on a hot plate (125^{0}C, 1 min.). Developed substrates were then etched in CR-4 chromium etchant for 3 minutes before being stripped of remaining photoresist in AZ-300T (5 min.). Substrates were rinsed in isopropanol, contact pads were covered in dicing tape and the substrates were coated with ~7 µm of Paralyene-C by vapour deposition. Subsequently, Teflon® AF was applied to the devices by spin coating as described above. Alternatively, superhydrophobic devices were coated with UED using the chromatography spraying protocol referenced above. Fig. 3.4 demonstrates a functional DMF device coated with Teflon® AF.
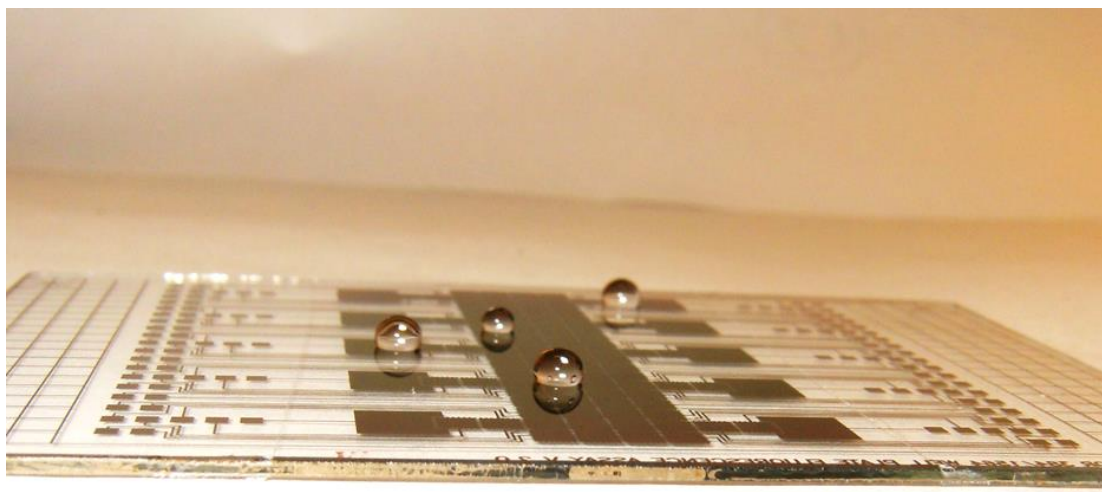
Figure 3.4: A photograph of an EWOD DMF device coated with Teflon® AF with several 10 µL aqueous droplets deposited on it.

Voltage was supplied through either a microfluidic toolkit (µTK - Micralyne, Edmonton Canada), which was used to generate DC voltages up to 2 kV, or through the microfluidics integration platform (MIP) system (PXI-4130 SMU module with a Tegam High Voltage Amplifier Model 2350)

90

provided by CMC Microsystems to generate DC voltages up to 200 V. CAs were recorded using a microUSB microscope, and imageJ freeware was used to measure and analyze CAs.

Surface characterization of the leaves and nanoparticle coatings was performed using scanning electron microscopy with energy dispersive X-ray (SEM-EDX). SEM-EDX analysis was performed on a MLA 650 FEG ESEM, where samples were gold coated prior to high vacuum scan in the backscatter mode.

3.3 Results and Discussions

3.3.1 Natural Surface – *Colocasia*

Superhydrophobicity in nature is a well-known phenomenon, where plant surfaces in particular were extensively studied and characterized.[38] The surface of the *Colocasia* exhibits superhydrophobicity, however to our knowledge the electrowetting properties of the elephant ear have not been reported to date. Fig. 3.5 demonstrates surface features of the elephant ear leaf, where the surface roughness (micro- and nano- scale) results in its superhydrophobicity.[39] The superhydrophobicity is attributed to the individual "microbumps" formed by surface papillae while the crystallized wax provides a low-energy surface. A previous electrowetting study performed on the lotus leaf demonstrated that substantially higher voltage is required for the EWOD actuation to be observed on a natural leaf surface compared to standard Teflon® AF coating.[40] Here we compare the EWOD performance of a natural *Colocasia* leaf surface, a new synthetic fluorinated silica nanoparticle coating, and a Teflon surface.
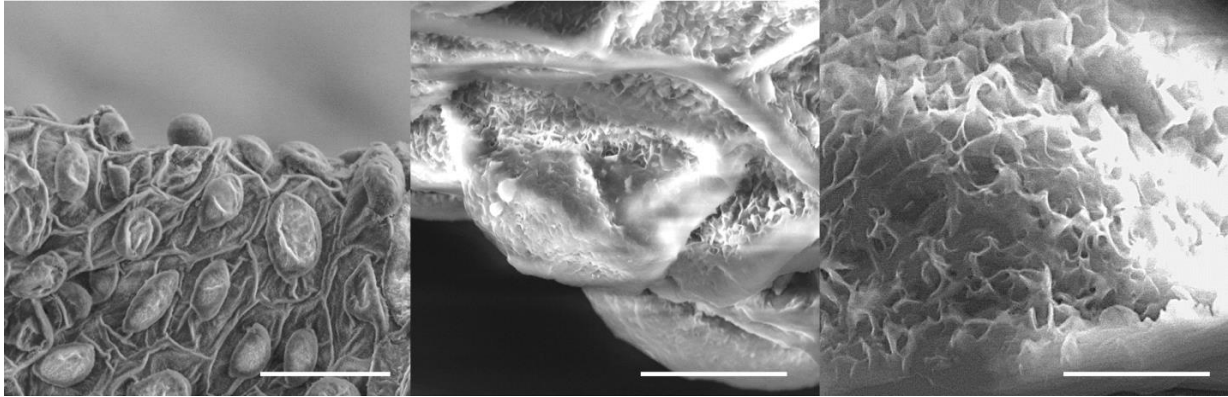
Figure 3.5: SEM images at different magnification of a dried *Colocasia* leaf, where the surface roughness can be observed on both micro- and nano-scale; (left) view of the leaf surface (scale bar = 50 µm); (centre) surface papillae attributing to micro-roughness (scale bar = 10 µm); (right) micro- and nano-roughness observed on individual papillae (scale bar = 2 µm).

Initial experiments were performed by directly attaching the leaf to the surface of the copper electrode (i.e. without a dielectric layer). Under an applied voltage (0.3 kV) the formation of bubbles in a droplet was observed due to water electrolysis and the leaf surface is quickly damaged indicating that the *Colocasia* leaf is a poor dielectric. All the following leaf EWOD experiments were conducted with a dielectric layer (adhesive tape) between the leaf and electrode.[41] The effect of the applied voltage to the water droplet is shown in Fig. 3.6.
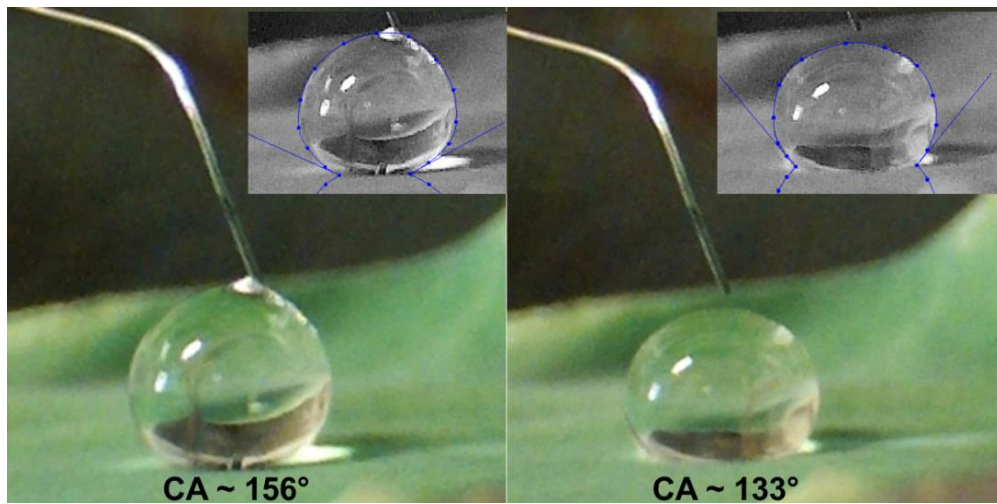
Figure 3.6: Contact angle change of a water droplet (10 µL) on a surface of *Colocasia* leaf under an applied voltage of 2.0 kV where CA change of over 20° is observed.

The EWOD experiments were performed on both the top and underside surfaces of the dried leaf and the results are summarized in Fig. 3.7.
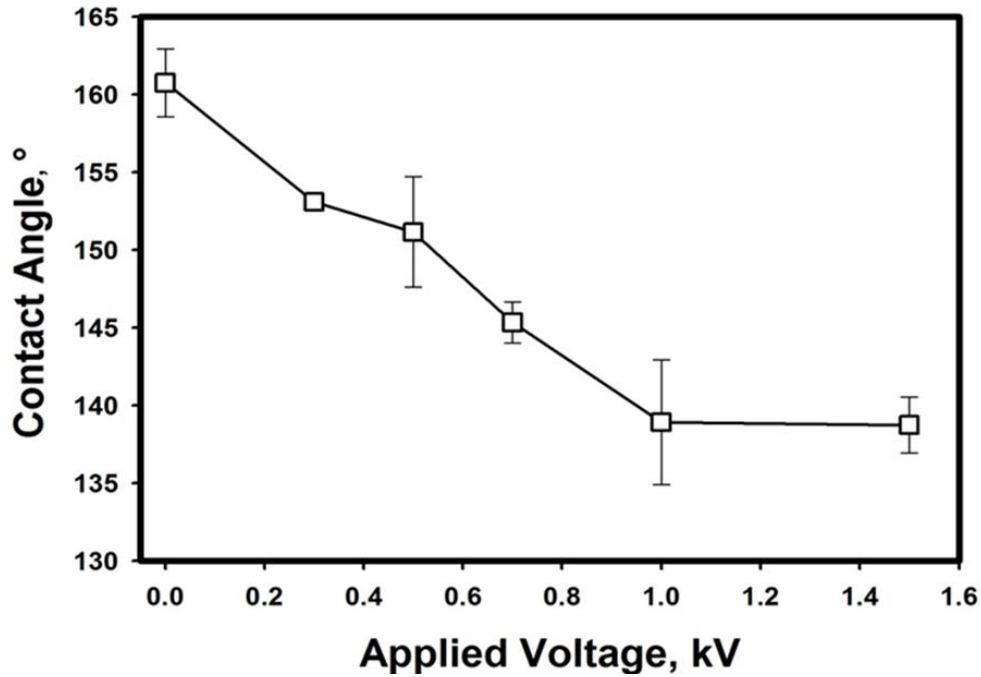
Figure 3.7: Contact angle observed for natural dried *Colocasia* leaf surfaces (top and underside) under increasing applied voltage. Error was calculated as an RSD value of 3 measurements.

The top and underside of the leaf showed similar WCA change at the same applied DC voltage, and SEM indicates similar morphologies between the two surfaces. Data presented here is a combined characterization of both top and underside of the leaf. CA change is determined as the difference between initial CA under no applied potential and the CA as the voltage is increased (eqn. 3.1):

$$CA_{change} = CA_{V=0} - CA_{Vapplied} \hspace{4cm} \text{Equation 3.1}$$

No CA change was observed when the applied voltage < 0.3 kV, and the CA steadily decreased as higher voltage was applied, until 1.5 kV where further increases in voltage resulted in no observable change, presumably due to contact angle saturation.[42,43] Thus, while EWOD can be demonstrated on the *Colocasia* leaf it requires a relatively high voltage (above 0.3 kV) compared to synthetic surfaces, which is not practical for general EWOD applications. A probable reason behind

this high voltage requirement is the thickness of the leaf (~60 μm dried and ~80 μm fresh), which is much thicker than a typical hydrophobic Teflon® AF coating (on the order of tens to hundreds of nanometres)[44,45] used in EWOD applications. Furthermore, the leaf was difficult to evenly adhere to the dielectric layer, and manual smoothing of the surface was found to damage the surface papillae and wax (data not shown). Although interesting, due to its high voltage requirements, the natural leaf surface is not well suited as a surface for DMF platforms, however its superhydrophobic properties served as a basis of comparison for synthetic superhydrophobic surfaces based upon silica nanoparticles.

3.3.2 Fluorinated Silica Nanoparticles Coating Characteristics and EWOD Performance

Synthetic hydrophobic coatings often employ heavily fluorinated species due to the high surface energy of these materials when placed in contact with water. Superhydrophobic coatings can be created by combining perfluoroalkyl substituents on a silica nanoparticle. These materials offer significant flexibility through a range of particle sizes and surface functionalizations. We conducted a systematic study that explored the effect of both degree of fluorination and particle size on the electrowetting properties of a synthesized surface. The comparison between different deposition methods ("sprayed" vs "casted") was also made. There are visual differences between the deposition methods, where the aero-sprayed surface is more translucent and evenly coated than the droplet casted surface Fig. 3.8.
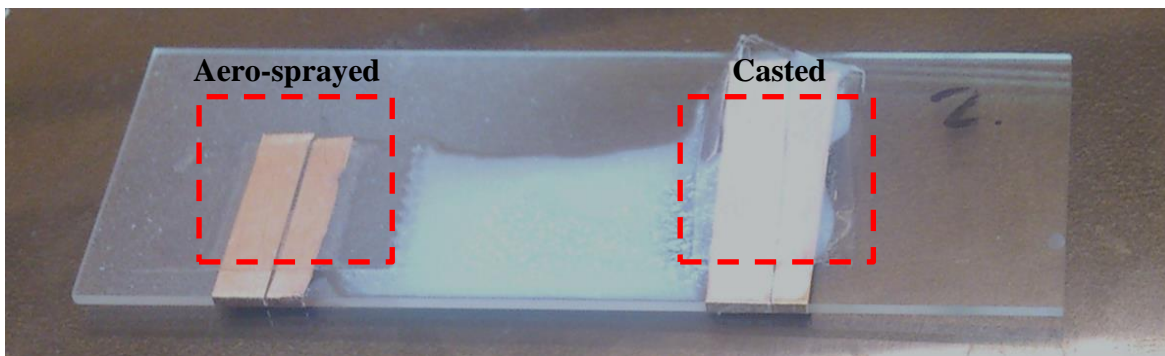
Figure 3.8: Visual comparison of the custom FSNP coating deposited via aero spraying (left) and droplet casting methods (right), where droplet casting method creates visibly thicker coatings.

For both material application methods, FSNPs do not form a homogeneous film layer, thus the coating thickness cannot be precisely measured. The FSNP coating thickness is estimated by examining the number of particle layers present via SEM (Fig. 3.9).
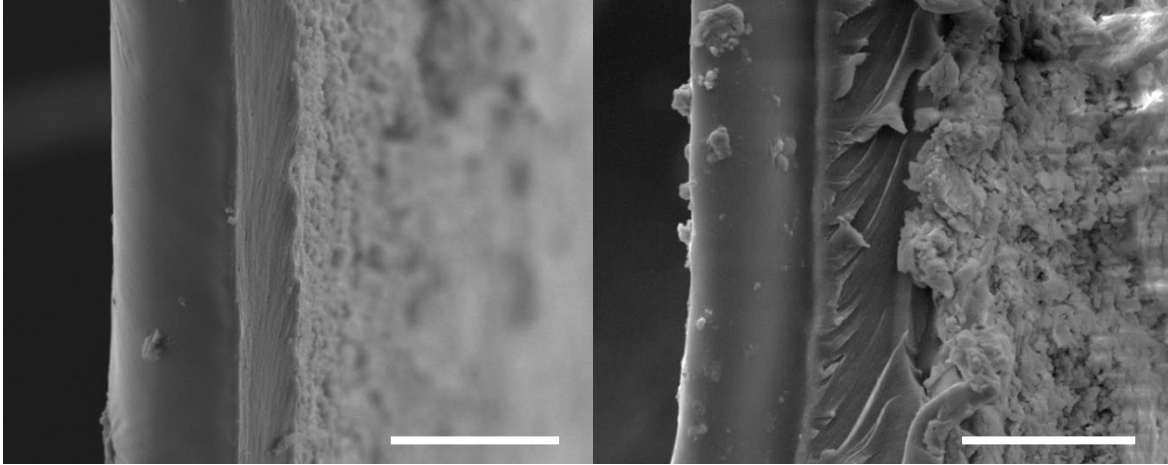
Figure 3.9: The SEM analysis of aero-sprayed surface (left) and droplet-casted surface (right). Images show the layer thickness formed by the standard application method, where the FSNPs are deposited onto a substrate (scale bar = 50 μm). The aero-spraying forms a thin layer typically comprised of 1 to 2 layers of FSNPs, while droplet casting results in multiple layers (6-10) of FSNPs deposited on top of each.

The FSNP coated tape is viewed edge-on and the number of particle layers was determined. The layer thickness is then calculated by multiplying the number of layers by the diameter of the modified particle. The droplet casting method generally results in 6 to 10 layers of the FSNPs, and the aero-sprayed methods results in single or double particle layer. The thickness can therefore vary between 90 and 1600 nm for the droplet casting; and 15-380 nm for the aero-sprayed FSNP coating depending upon particle size (Table 3.1).

Table 3.1: Thickness measurements of the custom-made FSNP coatings of different deposition methods.

Silica Particle Diameter (nm)	Droplet Casting Thickness (nm)		Aero-Sprayed Thickness (nm)	
	6 layers	**10 layers**	**Monolayer**	**Double layer**
5-10	90-120	150-200	15-20	30-40
25-30	210-240	350-400	35-35	70-80
85-90	570-600	950-1000	95-100	190-200
125-150	810-960	1350-1600	135-160	270-380

Scanning electron micrographs of surfaces coated with FSNP particles (90% fluorination) in four size ranges are shown in Fig.3.10.
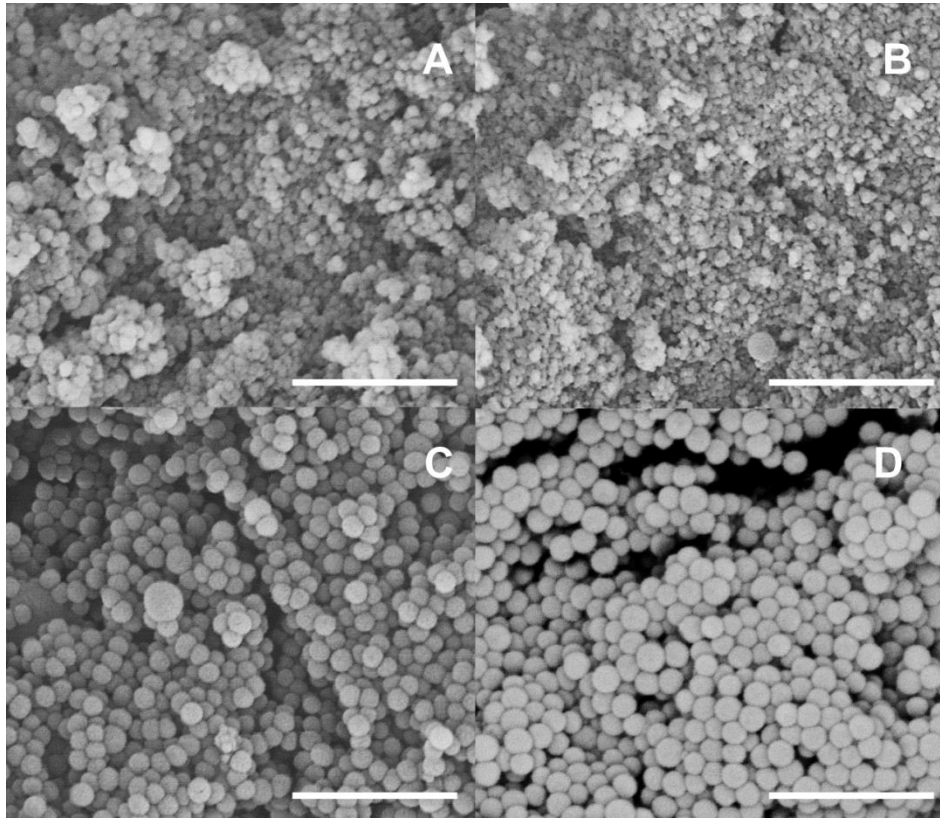
Figure 3.10: 100 000× magnified SEM images of the "casted" of FSNPs of various diameters: A) 5-10 nm, B) 25-30 nm, C) 85-90 nm, D) 125-150 nm. Scale bar is 1 μm in each image.

One evaluation criterion for electrowetting is the minimum voltage required for observable CA change. In this set of experiments, the minimal observable movement is defined as slight "twitching" of the droplet under the applied voltage. The results of this evaluation are presented in Table 3.2 for the "aero-sprayed" deposition method and "casted" deposition method. From Table 3.2 it can be seen that the particle size has a significant effect on the minimal voltage required for the onset of observable EWOD, whereas for the "sprayed" deposition method the particle size dependence appears more pronounced, with larger particles requiring lower actuation voltage (Table 3.2). Furthermore, actuation voltages for the "casted" FSNP layer are lower in every case than those required for the "sprayed" surface, suggesting that the droplet casting method is more suitable for

DMF applications. As the surface contact angle is related to the roughness and particle size, the change in CA was measured for each particle size and deposition method at constant voltage, the data also appearing in Table 3.2.

Table 3.2: DC voltage required for the onset of EWOD for the spray and cast coated particle deposition method for particles of varying sizes but constant degree of fluorination (90%).

Silica Particle Diameter (nm)	Droplet Casting Surface		Aero-Sprayed Surface	
	Minimum Voltage (V)	CA change (°)	Minimum Voltage (V)	CA change (°)
5-10	40 ± 20	6.5 ± 1.8	170 ± 10	2.4 ± 1.2
25-30	20 ± 10	8.4 ± 2.5	140 ± 10	2.3 ± 2.1
85-90	20 ± 10	12.9 ± 2.6	50 ± 10	8.3 ± 2.5
125-150	50 ± 20	9.7 ± 1.6	50 ± 20	9.2 ± 2.0

The surface roughness increases with particle diameter, however the contact angle change is not significantly impacted. That being said, the CA change for any given particle size is always higher for "casted" particles vs. "sprayed" particles. This is directly related to the relative coating thickness produced by the two deposition methods.

A similar set of experiments was carried out to determine whether the degree of fluorination affects the performance of the fluorinated silica particles as a hydrophobic layer for EWOD. It was established from the previous set of experiments that the "casting" deposition method allowed droplet actuation at lower voltages than the "sprayed" method, so the fluorination study was performed using the "casted" surfaces. For consistency, the 85-90 nm particles were used to study fluorination variation, where fluorinating degree ranged from 0-90%. Stable particles with 100% fluorination required a modified deposition procedure, thus they were not tested here. Particles with 0% and 10% fluorination did not exhibit hydrophobic properties (i.e. the droplet wetted the surface). Fluorination ≥25%, however, results in a hydrophobic surface with a measureable water droplet contact angle. Fig. 3.11 indicates that surfaces with 25 and 50% fluorination are not strictly superhydrophobic, as the observed CA is below 150°. The surfaces with higher degree of fluorination (75% and 90%) are both superhydrophobic, with contact angles >150°, and there is no significant difference in initial CA

between them. The CA measured at a constant applied voltage of 150 V was found to be independent of the degree of fluorination, measuring 142.2 ± 2.5° for all the surfaces tested.
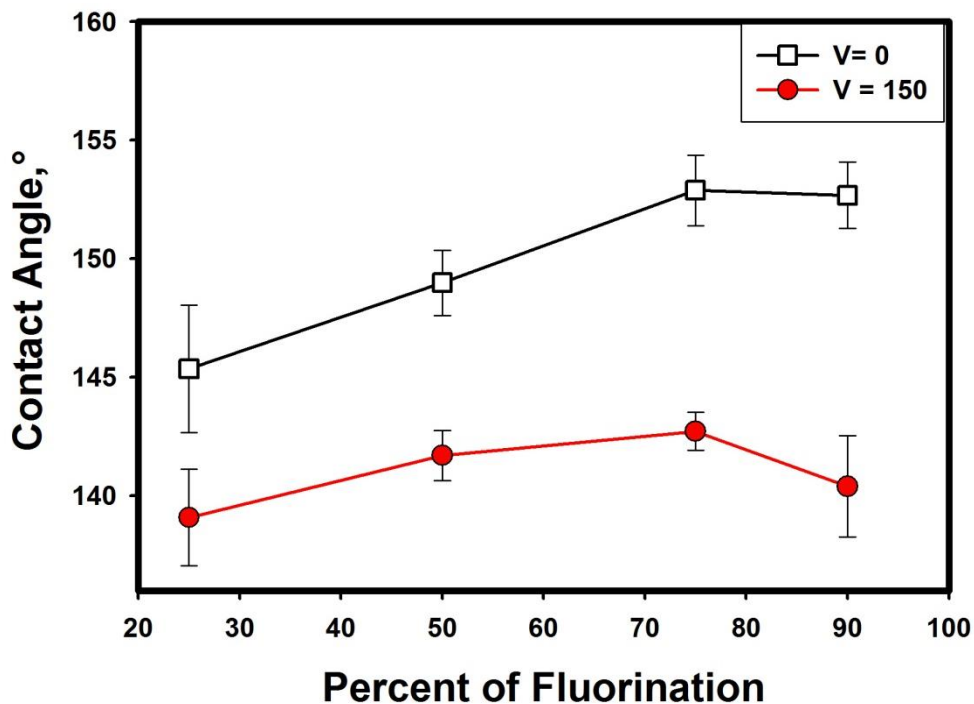
Figure 3.11: The effect of degree of fluorination on the initial contact angle (□) (at V=0) and the contact angle (●) under applied potential of 150 V. Error was calculated as an RSD value of 3 measurements.

Higher percent fluorination results in more reproducible EWOD which can be achieved at a lower voltage. FSNPs fluorinated at 25% required at least 80 ± 10 V to observe EWOD, while 50% fluorination only required 30 ± 10 V. EWOD can be achieved at 20 ± 10 V for both 75 and 90% FSNPs, however some irreproducibility in EWOD was observed for 75% fluorinated surface. The minimum advantages associated with more extensive fluorination suggest particles with lower fluorine content can be a cost-effective alternative to the expensive fluorine derivatization reagents.

3.3.3 Compatibility with Non-Aqueous Solutions

To better take advantage of the high diversity of applications that can be implemented onto a DMF platform, it is necessary for the coating to be compatible with solvents other than water. Aqueous mixtures of biological solutions, buffers, and salts have been extensively studied on both

open-top and two-plate configurations of DMF devices, however techniques such as separation or detection might require organic solvents to be used on the surface of the chip.[12,46] Chemical compatibility and electrowetting behavior of fluorinated nanoparticle-based surfaces with several commonly used solvents (i.e. acetone, acetonitrile, methanol, 2-propanol and diiodomethane) was probed. Overall, the FSNP surface coatings were robust to methanol, 2-propanol and diiodomethane and the casted surfaces displayed superior solvent resistance compared to the aero-sprayed coating. The contact angles for both methanol and 2-propanol were less than 90° for surfaces prepared using both deposition methods. On the "casted" surface, EWOD is observed starting at 150 V, and it becomes consistent at >170 V. Conversely the "aero-sprayed" surface required at least 600 V to achieve reproducible movement. Acetonitrile droplets show a CA of < 90°, although EWOD is possible at significantly lower voltages than for the alcohols tested (i.e. some change in contact angle can be observed at 90 V), reproducible electrowetting was achieved at voltages above 100 V. Although acetonitrile damaged the aero-sprayed surface, it did not appear to have an adverse effect on the thicker "casted" surface. Diiodomethane, being the least polar of the tested solvents, was found to form droplets with CA >90° on the surface, where EWOD can be observed at >80 V. This result demonstrates the amphiphobic character of the fluorinated nanoparticle surface as both highly polar (water) and non-polar (diiodomethane) solvents showed high CA. Experiments show that the fluorinated nanoparticle surface is incompatible with acetone, where the droplet spreads over the surface, often removing silica particles. Acetone droplets damage the surface, rendering it unusable; this effect is more obvious for the thinner "aero-sprayed" surface than a "casted" surface coating.

3.3.4 Stability of the Superhydrophobic Coatings

Longevity experiments were performed on both types of surface particle deposition methods i.e. droplet casting and aero-sprayed, where particles of different sizes were tested. A constant 110 V was applied in each case, and the change in contact angle with a fresh water droplet was measured on a weekly basis. The surfaces used in the longevity experiments were used for other multiple

experiments during the first two weeks, but only for longevity tests thereafter. Performance stability of

the surfaces was evaluated by examining how the initial water contact angle changes with time and use

for the "casting" method and the aero-sprayed method (Fig. 3.12).
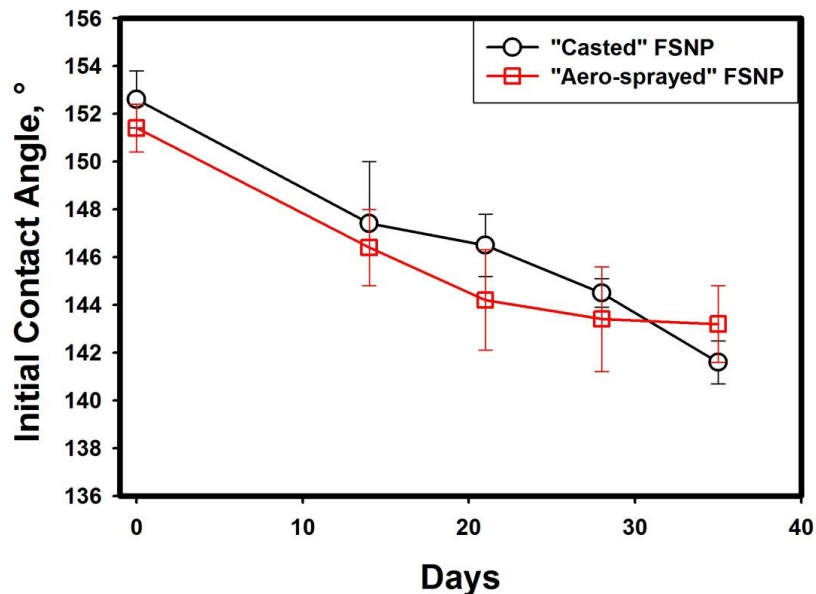
Figure 3.12: Effect of time on the WCA for 85-90 nm FSNPs with 90% fluorination, deposited by either droplet casting (○) or aero-sprayed (□) methods. Error was calculated as an RSD value of 3 measurements.

The decline in the WCA was measured for all FSNPs diameters synthesized, and detailed

information is present in Fig 3.13.
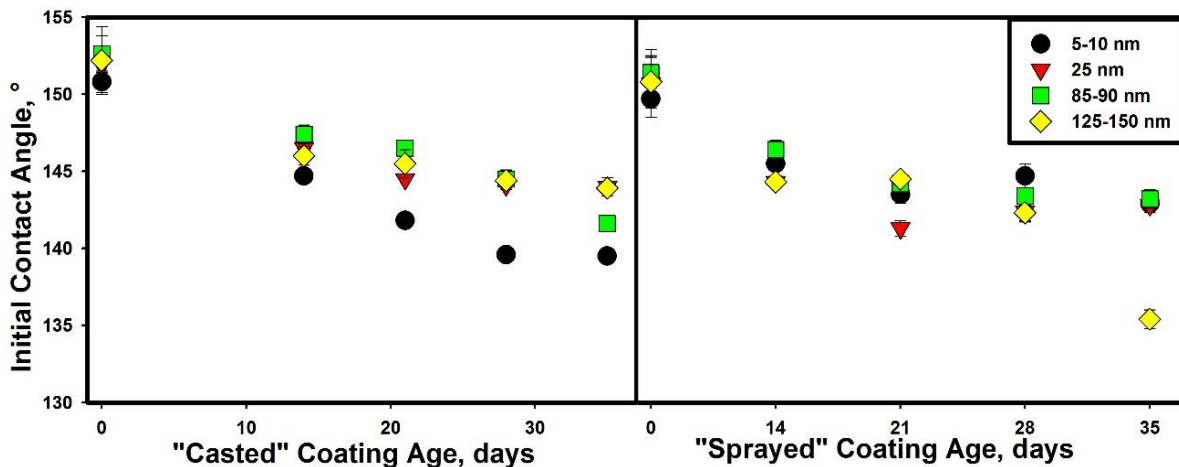
Figure 3.13: The decrease in the WCA for the "casted" and "sprayed" surfaces measured over a period of 35 days for various silica nanoparticles diameters. Error was calculated as an RSD value of 3 measurements.

100

A detailed comparison for each of the particle sizes is presented in Fig. 3.14 and 3.15.
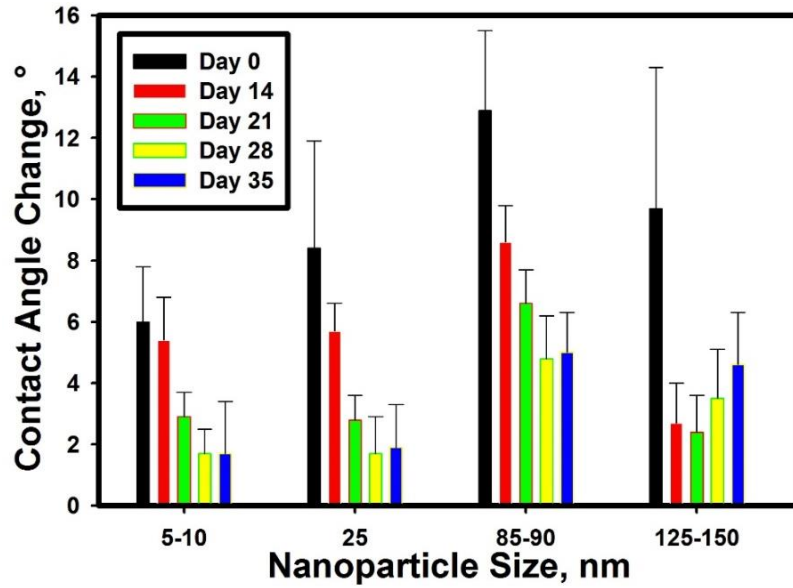
Figure 3.14: Contact angle change for "casted" surfaces with varying sizes of silica particles, 90% fluorinated. CA change was recorded at V = 110 V for all measurements. Error was calculated as an RSD value of 3 measurements.
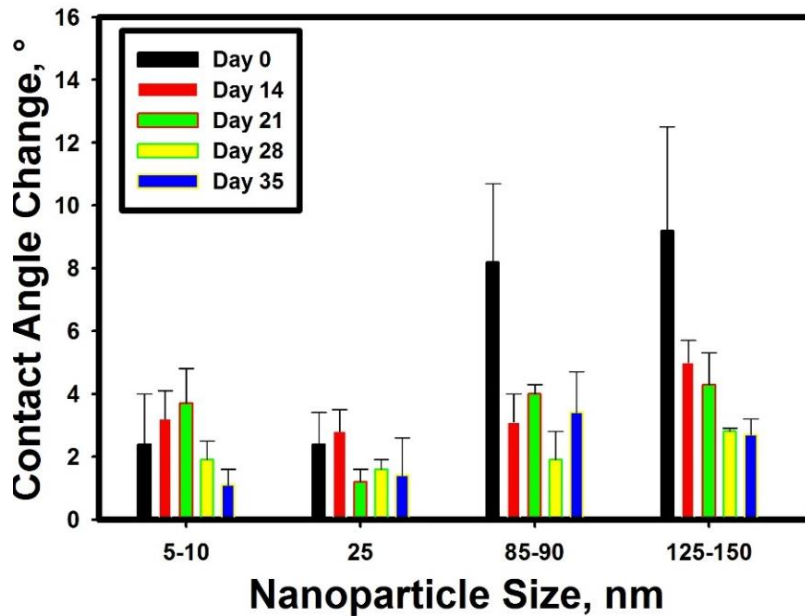
Figure 3.15: Contact angle change for "sprayed" surfaces with varying sizes of silica particles, 90% fluorinated. CA change was recorded at V = 110 V for all measurements. Error was calculated as an RSD value of 3 measurements.

The contact angle change, under the same applied voltage, decreases with time for both deposition methods (Fig. 3.12). The "aero-sprayed" surfaces generally show a larger decrease in both CA and CA change with time (e.g. after two weeks of use the CA change is less than 6°). Coatings with FSNPs in the range of 5-10 nm and 25-30 nm do not show as significant a drop in CA change with time; however even freshly prepared 5-30 nm particles exhibit smaller initial contact angle changes (i.e. 5°). Surfaces with 85-90 nm and 125-150 nm particles show the best performance, where there is steady but gradual decrease in CA change, and after 4 weeks of testing the WCA change is still above 4°. In terms of the most robust surface suitable for EWOD applications, 85-90 nm silica particles deposited by "casting" method offers best performance, where after 35 days of use the CA change is about 5°. The "casted" surfaces are generally more robust and demonstrate better stability with time and a smaller drop in CA change after prolonged use.

3.3.5 Printed Circuit Board EWOD Device Characteristics and Performance

PCB technology is often a quick and inexpensive alternative to photolithographic methods, and it is widely adopted in microelectronics technology. Commercial PCB microchips could be directly purchased with specified parameters (i.e. electrode size, gap, and shape) and it was a good starting point to incorporate various electrode designs and parameters. The performance of this particular PCB microchip design did not result into droplet actuation, and this can be explained by the unforeseen flaws in the device fabrication.

The performance of the EWOD device depends on many parameters, including the composition and thickness of electrodes, dielectric layer and the hydrophobic layer. A variety of metals has been used in electrode manufacturing, including gold, silver, titanium, copper and chromium; typically, the thickness of the electrodes is ranging from several nanometres to ~ 200 nm.[47] The shape of electrodes also contributes to the effectives of droplet actuation, where intertwining or "crossing over" electrodes can facilitate movement. The "saw" shape of the electrodes, where a resting droplet is overlapping two electrodes, can significantly lower the actuation voltage.[48,49] Another

102

important consideration is the inter-electrode distance, which can also effect the actuation; the narrower distance between the electrodes is reported to lower the actuation voltage. In our PCB design we have tried various combinations of shapes (straight or saw) and inter-electrode distances – 40, 50 or 60 μm. The height of the electrodes was determined to be on the order of several micrometres, thus in order to create an even dielectric layer, about 14 μm of parylene C was required.

The device did not demonstrate a reproducible performance, where the main reason for the failure was the unexpected design flow, inherited from the fabrication procedure. The manufacturing of PCB device required "vias", plated through holes to connect the copper electrodes on different layers. The "vias" were significantly higher than the rest of the electrode, and were protruding even when coated with dielectric layer. These "vias" were trapping the droplets in place, preventing their actuation.

3.3.6 Droplet Actuation of Digital Microfluidic Devices with Hydrophobic Coating

Hydrophobic coatings (Teflon® AF and FSNPs) were tested for droplet actuation performance using a DMF platform/device consisting of an array of 80 interdigitated working electrodes (2.2 mm x 2.2 mm) (Fig. 3.4). The droplets of 10-20 μL were actuated across several electrodes and the required voltage and reproducibility of droplet movement was probed. The Teflon® AF coated devices required an actuation voltage of 250±50 V and showed consistent droplet movement across the electrode array. Similarly a surface coated with commercial FSNP showed reproducible droplet actuation at a voltage of 300±100 V. In these experiments the voltage was applied to the electrode intended for auction, and ground voltage was applied to the electrode where the droplet was resting. For the Teflon® AF coated devices the droplet would actuate to the next electrode and remain there until the voltage was applied to the next adjacent electrode. The Teflon® AF surface with a contact angle of ≈ 120° provided enough droplet/surface adhesion to "pin" the droplet. Conversely, a droplet often continues to slide beyond the actuating electrode after the first actuation step for the superhydrophobic FSNP coated surfaces, as the friction is minimal on superhydrophobic surfaces. As

103

a result, once the droplet was actuated its momentum carries it beyond the next electrode. This is particularly problematic for devices that are manually actuated as the droplet moves beyond the next electrode before the voltage is applied. In automatic systems the voltage switching time can be minimized and erratic droplet actuation should be minimized by the pinning force afforded through the contact angle change with application of voltage.

3.4 Conclusion

Natural and synthetic superhydrophobic coatings that utilize both micro- and a nano- structure with hydrophobic coatings provide low friction surfaces for aqueous droplet actuation. Electrowetting-on-dielectric was examined for both natural and FSNP coated surfaces and compared to Teflon® AF. EWOD for the natural surface showed the highest voltage requirement at 300 V, which is undesirable. EWOD on FSNP surfaces occurred at significantly lower voltages (<50 V) and is shown to depend on the method of coating application (i.e. casting or aero-spray), particle dimension and degree of fluorination. The casting method showed enhanced robustness with minimal contact angle difference, and contact angle change over a month of use. FSNP coated DMF device was used for droplet actuation and showed similar voltage requirement to Teflon® AF coated devices (~ 250±50 V). Although the CA change observed on the FSNP surfaces was smaller than that of Teflon® AF, droplet movement was possible but with lower precision, due to the lack of a pinning force (i.e. reduced adhesive force) in the absence of an applied voltage.

3.5 References

1.   M. C. Draper, C. R. Crick, V. Orlickaite, V. A. Turek, I. P. Parkin and J. B. Edel, *Anal. Chem.*, 2013, **85**, 5405-10.

2.   B. Bhushan and Y. C. Jung, *Nanotechnology*, 2006, **17**, 2758-72.

3.   L. Cao, A. K. Jones, V. K. Sikka, J. Wu and D. Gao, *Langmuir*, 2009, **25**, 12444-8.

4.   X. M. Li, D. Reinhoudt and M. Crego-Calama, *Chem. Soc. Rev.*, 2007, **36**, 1350-68.

5.   A. B. D. Cassie and S. Baxter, *T. Faraday Soc.*, 1944, **40**, 0546-50.

6.   M. Ma and R. M. Hill, *Curr. Opin. Colloid Interface Sci.*, 2006, **11**, 193-202.

7.   B. Bhushan and Y. C. Jung, *Prog. Mater. Sci.*, 2011, **56**, 1-108.

8.   F. Mumm, A. T. van Helvoort and P. Sikorski, *ACS Nano*, 2009, **3**, 2647-52.

9.   J. Genzer and K. Efimenko, *Biofouling*, 2006, **22**, 339-60.

10.   D. Xiong, G. Liu and E. J. Duncan, *Langmuir*, 2012, **28**, 6911-8.

11.   F. Mugele and J.-C. Baret, *J. Phys.: Condens. Matter*, 2005, **17**, 705-74.

12.   D. Chatterjee, B. Hetayothin, A. R. Wheeler, D. J. King and R. L. Garrell, *Lab Chip*, 2006, **6**, 199-206.

13.   I. Moon and J. Kim, *Sens. Actuators A: Phys.*, 2006, **130-131**, 537-44.

14.   M. Abdelgawad and A. R. Wheeler, *Microfluid. Nanofluid.*, 2007, **4**, 349-55.

15.   S. K. Cho, H. J. Moon and C. J. Kim, *J. Microelectromech. Syst.*, 2003, **12**, 70-80.

16.   D. Brassard, L. Malic, F. Normandin, M. Tabrizian and T. Veres, *Lab Chip*, 2008, **8**, 1342-9.

17.   A. Banerjee, Y. Liu, J. Heikenfeld and I. Papautsky, *Lab Chip*, 2012, **12**, 5138-41.

18.   A. Accardo, F. Mecarini, M. Leoncini, F. Brandi, E. Di Cola, M. Burghammer, C. Riekel and E. Di Fabrizio, *Lab Chip*, 2013, **13**, 332-5.

19.   S. K. Cho, S. K. Fan, H. J. Moon and C. J. Kim, *Fifteenth Ieee International Conference on Micro Electro Mechanical Systems, Technical Digest*, 2002, 32-5.

20.   S. C. Shih, H. Yang, M. J. Jebrail, R. Fobel, N. McIntosh, O. Y. Al-Dirbashi, P. Chakraborty and A. R. Wheeler, *Anal. Chem.*, 2012, **84**, 3731-8.

21.   Y. J. Zhao, U. C. Yi and S. K. Cho, *J. Microelectromech. Syst.*, 2007, **16**, 1472-81.

22.   D. Beyssen, L. Le Brizoual, O. Elmazria and P. Alnot, *Sensor Actuat B-Chem*, 2006, **118**, 380-5.

23.   N. Pamme, *Lab Chip*, 2006, **6**, 24-38.

24.   Z. Long, A. M. Shetty, M. J. Solomon and R. G. Larson, *Lab Chip*, 2009, **9**, 1567-75.

25.   R. Bavière, J. Boutet and Y. Fouillet, *Microfluid. Nanofluid.*, 2007, **4**, 287-94.

26.	M. J. Jebrail, M. S. Bartsch and K. D. Patel, *Lab Chip*, 2012, **12**, 2452-63.

27.	K. H. Kang, *Langmuir*, 2002, **18**, 10318-22.

28.	M. Jonsson-Niedziolka, F. Lapierre, Y. Coffinier, S. J. Parry, F. Zoueshtiagh, T. Foat, V. Thomy and R. Boukherroub, *Lab Chip*, 2011, **11**, 490-6.

29.	F. Saeki, J. Baum, H. Moon, J. Y. Yoon, C. J. Kim and R. L. Garrell, *Abstr. Pap. Am. Chem. S.*, 2001, **222**, 341-2.

30.	H. Zhang and S. G. Weber, *Top. Curr. Chem.*, 2012, **308**, 307-37.

31.	V. N. Luk, G. C. H. Mo and A. R. Wheeler, *Langmuir*, 2008, **24**, 6382-9.

32.	S. H. Au, P. Kumar and A. R. Wheeler, *Langmuir*, 2011, **27**, 8586-94.

33.	H. J. Ensikat, P. Ditsche-Kuru, C. Neinhuis and W. Barthlott, *Beilstein J. Nanotechnol.*, 2011, **2**, 152-61.

34.	S. C. C. Shih, R. Fobel, P. Kumar and A. R. Wheeler, *Lab Chip*, 2011, **11**, 535-40.

35.	W. Stober, A. Fink and E. Bohn, *J. Colloid Interface Sci.*, 1968, **26**, 62-9.

36.	J. F. Ding and G. J. Liu, *Macromolecules*, 1999, **32**, 8413-20.

37.	A. H. C. Ng, K. Choi, R. P. Luoma, J. M. Robinson and A. R. Wheeler, *Anal. Chem.*, 2012, **84**, 8805-12.

38.	Y. T. Cheng, D. E. Rodak, C. A. Wong and C. A. Hayden, *Nanotechnology*, 2006, **17**, 1359-62.

39.	K. Koch, A. Dommisse and W. Barthlott, *Cryst. Growth Des.*, 2006, **6**, 2571-8.

40.	J. T. Feng, F. C. Wang and Y. P. Zhao, *Biomicrofluidics*, 2009, **3**, 22406.

41.	H. Moon, S. K. Cho, R. L. Garrell and C.-J. C. Kim, *J. Appl. Phys.*, 2002, **92**, 4080-7.

42.	A. G. Papathanasiou, A. T. Papaioannou and A. G. Boudouvis, *J. Appl. Phys.*, 2008, **103,** 034901.

43.	A. I. Drygiannakis, A. G. Papathanasiou and A. G. Boudouvis, *Langmuir*, 2009, **25**, 147-52.

44.   J. B. Chae, J. O. Kwon, J. S. Yang, K. Rhee and S. K. Chung, *26th Ieee International Conference on Micro Electro Mechanical Systems (Mems 2013)*, 2013, 1109-12.

45.   H. Yang, J. M. Mudrik, M. J. Jebrail and A. R. Wheeler, *Anal. Chem.*, 2011, **83**, 3824-30.

46.   D. Mark, S. Haeberle, G. Roth, F. von Stetten and R. Zengerle, *Chem. Soc. Rev.*, 2010, **39**, 1153-82.

47.   H. Liu, S. Dharmatilleke, D. K. Maurya and A. A. O. Tay, *Microsyst. Technol.*, 2010, **16**, 449-60.

48.   D. Das, S. Das and K. Biswas, *International Conference on Systems in Medicine and Biology*, 2010, 371-5.

49.   L. S. Jang, C. Y. Hsu and C. H. Chen, *Biomed. Microdevices*, 2009, **11**, 1029-36.

Chapter 4

Magnetic Droplet Actuation on Natural (*Colocasia* Leaf*)* and Fluorinated Silica Nanoparticle Superhydrophobic Surfaces

4.1 Introduction

Precise and independent control of small volumes of liquids is a fundamental advantage of microfluidic devices. Digital microfluidics (DMF) has recently gained popularity due to its ability to independently address, move and position individual droplets in a precise and reproducible manner.[1,2] Moreover, DMF offers the advantages of channel-based continuous flow microfluidics, such as reduced reagent consumption and the ability to integrate several sample analysis steps onto a single device, while not being susceptible to clogging. The most common method for droplet actuation on DMF devices utilizes the electrowetting-on-dielectric (EWOD) phenomenon, where droplet movement results from a shift in the distribution of electrohydrodynamic forces due to an applied voltage, leading to the reduction in the contact angle (CA) between a droplet and the surface.[3-5] Accurate control over droplet movement is provided through the application of voltage to a photolithographically patterned metallic electrode array (e.g. chromium or gold) coated with both a dielectric and a hydrophobic layer.[6-8] EWOD devices have suffered from robustness concerns that stem from surface contamination and fragility of the hydrophobic layer.[9]

An alternative actuation method for the DMF platform is based on magnetic actuation, where a ferromagnetic fluid or aqueous droplet containing particles with high magnetic susceptibility is manipulated with an applied magnetic field, also known as digital magnetofluidics.[10-12] Like EWOD devices, magnetically actuated devices require a hydrophobic layer to reduce the friction between the aqueous droplet and surface, enabling the droplet to slide over the surface with little resistance.[13,14]

Some plant species have evolved superhydrophobic "self-cleaning" leaves that shed water, dust and debris following a rain to maintain high photosynthetic efficiency.[15] Superhydrophobicity,

defined as having a CA with water in excess of 150°, is achieved through a combination of leaf surface roughness and low surface energy provided by hydrophobic waxy compounds.[16,17] The roughness of the lotus leaf, for example, arises from a hierarchical structure with features on the micrometre and nanometre scales. The water droplet does not wet the hydrophobic surface between these features, leaving them filled with air and keeping contact between the liquid and surface to a minimum. This is in the heterogeneous wetting regime and its behavior is described by the Cassie-Baxter model.[18] Synthetic surfaces with both micrometre- and nanometre-scaled roughness have traditionally been produced in the laboratory using photolithography, chemical vapour deposition, silicon nanowire growth, or electrochemical etching.[19-21] Functionalization of the surface with nonpolar (e.g. perfluoroalkyl) substituents produces superhydrophobic surfaces with high CAs (> 150°) and low roll-off angles (ROA) (<10°) with water.[13,22,23] Superhydrophobic coatings are commonly used in magnetofluidics because increased surface hydrophobicity further decreases the surface friction, which results in a droplet sliding over the surface with minimal applied forces.[24-26] With the reduced friction of the superhydrophobic surface, no additional oil phase is necessary to operate the device, which is often beneficial for hydrophobic surfaces such as Teflon®, making overall operation more facile and efficient.[27] Recently, a number of new commercial superhydrophobic coatings have become available for a range of consumer applications based on silica nanoparticles.[21,28,29] The addition of magnetically susceptible materials, i.e. superparamagnetic particles and ferrofluids, to the droplet enables an actuation force to be easily applied to the droplet through an externally applied magnetic field. Extensive and comprehensive analysis of ferrofluidic manipulation on DMF devices has been previously reported therefore here we concentrate on aqueous droplets containing paramagnetic particles only.[24,30,31] Commercial "magnetic particles" for this purpose are based on (super)paramagnetic particles, where an iron oxide core is surrounded by a layer of silica, which can be functionalized as desired for a given application.[32-35] Many devices using

magnetic actuation have been reported, and complex droplet movement has been demonstrated in three dimensions, including actuation of an inverted droplet.[20]

In this chapter the interactions of aqueous droplets with three different materials with varying degrees of hydrophobicity are investigated, namely Teflon® AF, a standard hydrophobic DMF coating; *Colocasia* leaf, a natural superhydrophobic plant surface; and a commercially available superhydrophobic coating based on fluorinated silica nanoparticles (FSNPs), Ultra-Ever Dry® (UED). Another commercial FSNP-based coating, NeverWet®, was tested for the usability and stability; however its performance was inferior to that of Ultra-Ever Dry®. The FSNPs can be applied to a glass, polymer, fabric[36] or metallic surfaces through a simple spraying procedure.[28]

We examine the superhydrophobicity of the surfaces, including the effect of magnetic field strength and superparamagnetic particle concentration on CA, ROA, ease of magnetic manipulation and actuation speed. We report adhesion force values determined using ROA for droplets on the three surfaces studied, and probe the UED surface stability with non-aqueous solvent combinations commonly employed in DMF applications. We also demonstrate the usability of our magnetic actuation system in a variety of applications, where droplets can be precisely controlled to deliver various volumes of reagents to a hydrophilic patch. The magnetic particle cluster can be removed and reused, serving as the means of continuously supplying the reaction with additional reagents. We have also looked at the two-plate droplet manipulation system, where various operations on the droplet-magnetic particles system can be performed depending on the distance between the two plates, droplet size and particle concentration.

4.2 Experimental

4.2.1 Materials

Deionized water (Fisher Scientific, Ottawa, Canada) mixed with various proportions of acetonitrile and methanol was used to form droplets on different surfaces. Glass microscope slides (Fisher Scientific, 76 x 25 x 1.0 mm) were used as the device substrate. Surfaces used in this study

were selected based on varying level of hydrophobicity. Teflon® AF (DuPont™) was used as a reference as it is a standard hydrophobic surface coating used for DMF devices. It was spin coated with a Laurell WS-650 spin coater (North Wales, PA, USA) using a two-step process: 500 RPM for 10 seconds and 3000 RPM for 30 seconds. The measured thickness of the coating was about 150 nm.[37] Natural superhydrophobic surfaces (*Colocasia* plant leaves) were grown locally and harvested when leaf sizes were >30 cm diameter. Ultra-Ever Dry® (UED) was purchased from Hazmasters (Ottawa, Canada) as a two-part coating, a base coat (adhesive) and top coat, which contained the fluorinated silica nanoparticles (FSNPs). NeverWet ®, (Rust-Oleum, Concord, ON) was purchased from Canadian Tire, as two pre-packaged aerosol cans, containing the base adhesive layer and the top layer containing FSNPs. There were two neodymium magnets used in this experiment – a flat disk used for CA and ROA measurements, and small cylindrical magnet used for droplet manipulation and velocity measurements. The strength of each magnet was measured using a gaussmeter (Model 410, LakeShore Cryotronics Inc., Westervill, OH) over a glass slide of 1 mm in thickness to determine the field strength. The strength was measured to be ~ 2.1 kG for the large disk magnet and ~ 1.8 kG for the small cylindrical magnet. Superparamagnetic particles were obtained from Bioclone Inc. (San Diego, USA), having a diameter of ~1.0 μm and an iron oxide core. Silica-coated superparamagnetic particles (40 mg/mL; catalog #FF-102) with reported magnetization of ~40 emu/g were used for all the experiments.

4.2.2 Surface Preparation

Both base and top coats of UED were applied according to manufacturer's instructions with a thin-layer chromatography sprayer. The base coat was sprayed twice over the clean glass slide surface and air dried in a fume hood for 20 minutes at ambient temperature. Similarly, two layers of the top coat were uniformly sprayed over the dried surface of base coat and then air dried in the fume hood for at least two hours before use. This method results in a uniform superhydrophobic coating of ~ 5.1 ± 0.4 μm as measured by SEM (Fig. 4.1).

111
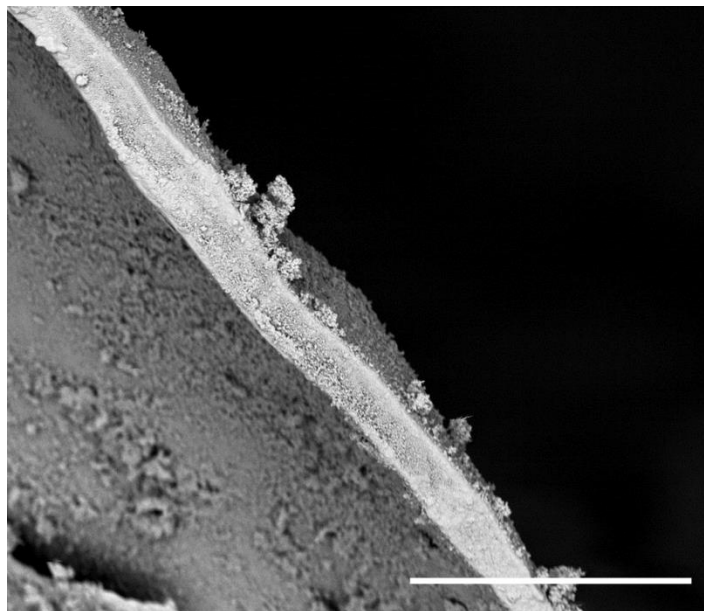
Figure 4.1: SEM of the side view of the FNSP (UED) surface, with both bottom and top layer applied twice (scale bar is 30 µm).

To coat the slide surface with the NeverWet®, the cans were vigorously shaken for about a minute before each use, and then two layers of the base coat were sprayed onto the surface of the methanol-cleaned glass slide from about 30 cm distance. The coated slide was then left to dry for at least 30 minutes in the fumehood. The can containing top layer was shaken for about two minutes, and then two layers were sprayed on the base-coated glass slide from 30 cm distance. The coated slide was left to dry in the fumehood overnight.

4.2.3 Contact Angle and Roll-off Angle Measurements

CAs were recorded using a microUSB microscope equipped with a camera (Veho X400, VMS-004D), and imageJ freeware was used to measure and analyze CAs. The same camera and software were used to measure the roll-off angles. A system of two lab-jacks was implemented, in order to have either a leveled surface (for CA measurement) or to be able to adjust the incline of the surface (for ROA measurement) Fig. 4.2.
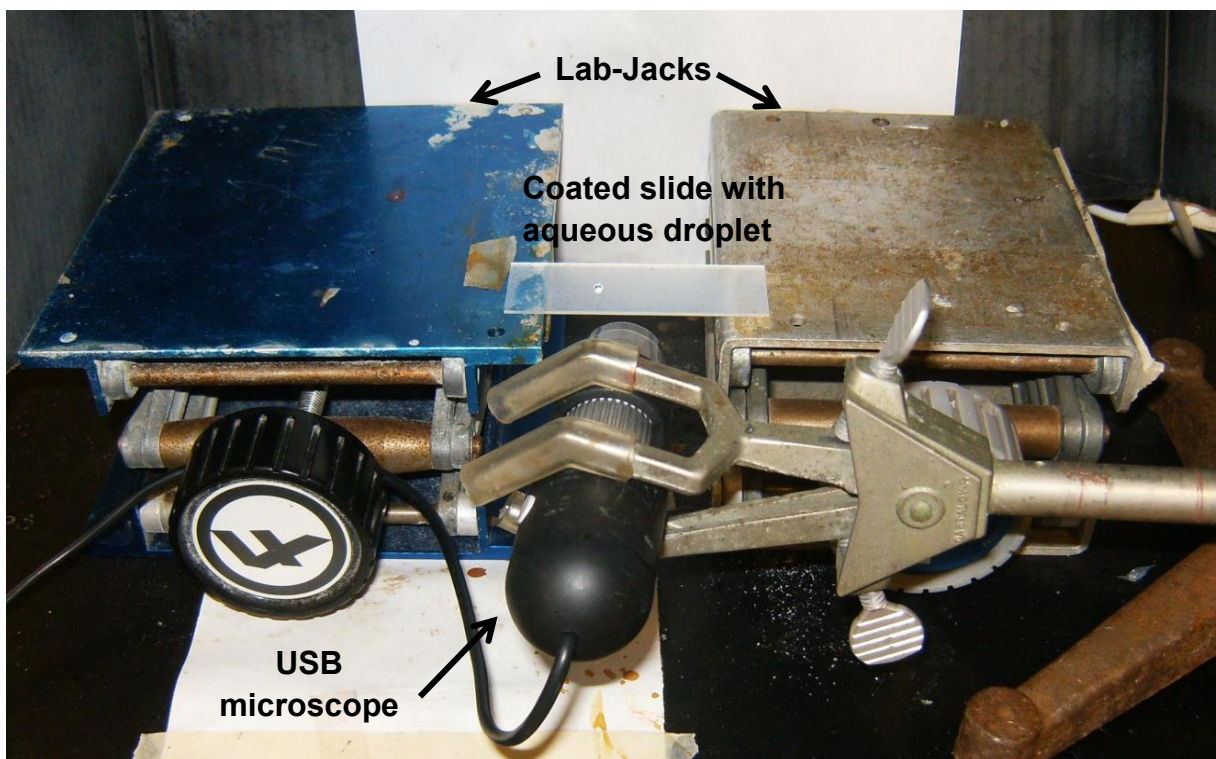
Figure 4.2: The set-up used to measure CAs and ROA, where two lab-jacks were positioned at the same height, and the coated glass slide was positioned in-between the lab jacks.

Fresh leaves of *Colocasia* plant were grown locally and used either within hours of being removed from the garden or dried after being attached to the glass slide. Leaf materials (fresh and dried) were adhered to the slide using double-sided adhesive tape, taking care to ensure that the leaf surface was as flat as possible.

4.2.4 Surface Imaging

Surface characterization of the leaves, the Teflon® AF and both layers of UED coating was carried out with scanning electron microscopy and energy-dispersive X-ray (SEM-EDX). SEM-EDX analysis was performed on a MLA 650 FEG ESEM, where samples were gold coated prior to high-vacuum scanning in the backscatter mode. Elemental composition was investigated by X-ray photoelectron spectroscopy (XPS) using Thermo VG Scientific Microlab 310-F.

4.2.5 Droplet Actuation Velocity

A 30 mm distance was delineated on the underside of a glass slide having FSNPs coated on its top side. The average speed was determined by measuring the time it takes the droplet to travel over the 30 mm distance using Microsoft® Windows™ Movie Maker to analyze videos recorded with a Veho USB microscope with millisecond precision. The maximum (peak) velocity during the experiment was measured over a small distance around the midway point just prior to droplet deceleration.

4.3 Results and Discussion

4.3.1 Surface Characterization

Hydrophobicity/superhydrophobicity stems from both the physical and chemical morphology of the surface. Typical superhydrophobic surfaces have a combination of micro- and nano-scaled roughness to facilitate air entrapment beneath the droplet, described by the Cassie-Baxter model. Further increase in CA arises from lowering the surface energy, achieved by addition of a chemical coating, which often includes fluorination for artificial surfaces or organic wax in plants. The difference in hydrophobicity for Teflon® AF, FSNPs and *Colocasia* leaf can be explained by the surface properties of each substrate. Both commercial surfaces, UED and NeverWet®, were tested for their performance in terms of CA and ROA and the reproducibility of surface coverage. Overall, UED demonstrated a superior performance, where either the deposition method or the material itself was more suitable for magnetic actuation applications. The surfaces coated with NeverWet® demonstrated poor, uneven coverage, where measured CA and ROA could vary greatly depending on where the measurement was taken. UED coating was reproducible from slide to slide, where CA and RO angles were consistent, and systematically higher than those for NeverWet®. Thus, UED was deemed as a superior commercial material, and it was further studied in terms of morphology, composition and performance. SEM analysis was performed to probe the surface morphology of each material, where for UED both top FSNP layer and bottom adhesive coating were analyzed separately. The presence of

fluorine atoms in the top layer of UED was confirmed by both EDX spectroscopy and XPS, where specific peaks corresponding to the X-ray emission (EDX) or electron binding energy (XPS) are characteristic of fluorine (see Fig. 4.3).
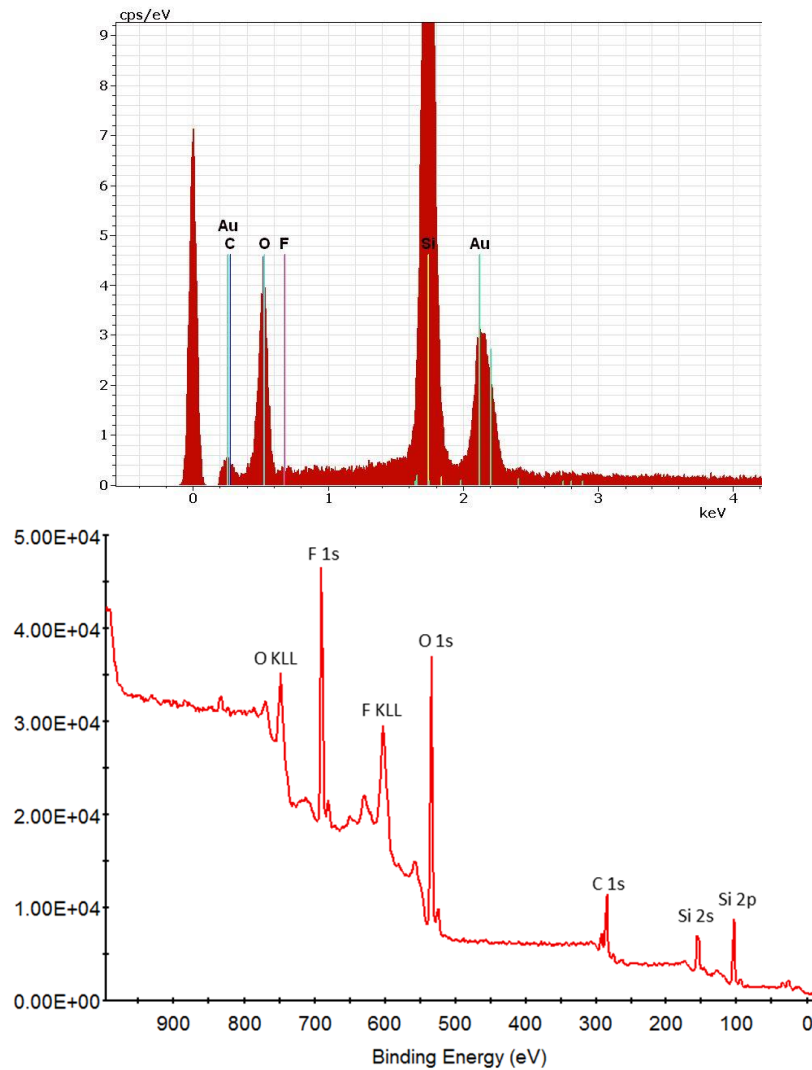
Figure 4.3: EDX (top) and XPS (bottom) spectra of the UED top layer, indicating the presence of fluorine in the material.

Presented in Fig. 4.4 are representative SEM images for each of the surfaces studied on both the micro- and nano-scale.
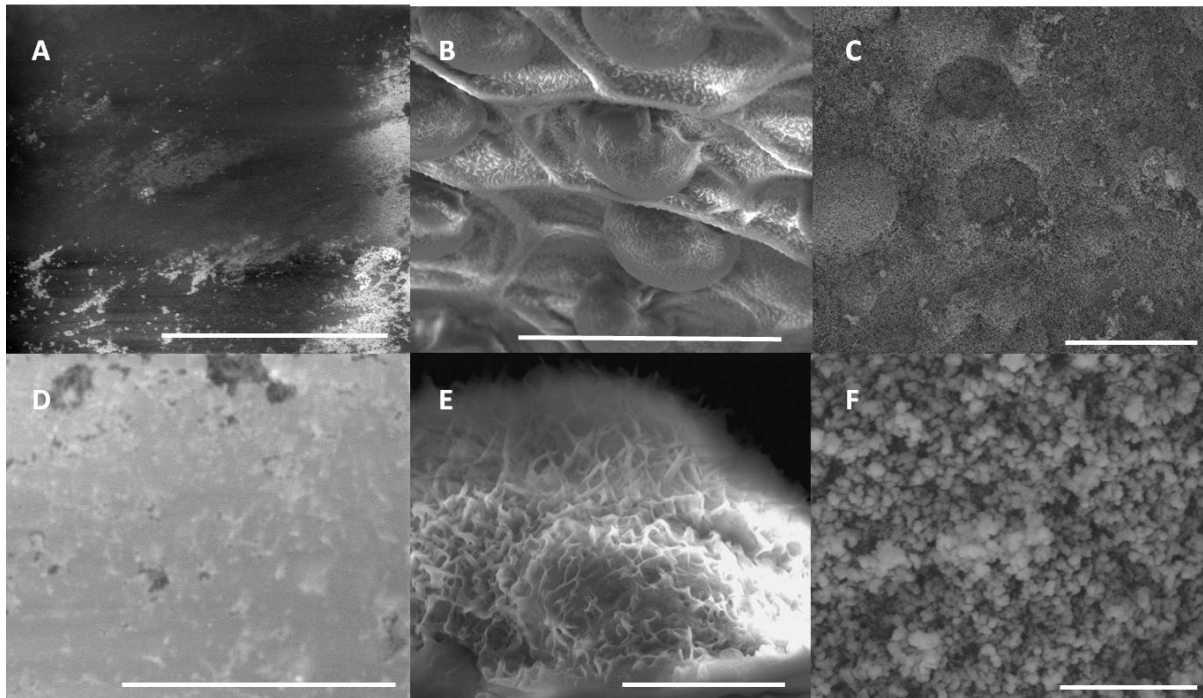
Figure 4.4: Representative SEM images of each of the surfaces studied at various magnifications. Top row shows micro-scale features (scale bar = 20 μm for images A-C), while bottom row shows nano-scale features (scale bar = 4 μm for D and E, and 1 μm for F): A – Teflon® AF surface with no defined micro-sized surface features; B – micro-scale bumps on the *Colocasia* leaf surface; C – micro-scale roughness of FSNP coating; D – Teflon® AF surface with no defined nano-sized surface features; E – close-up of a micro-scale bump on a leaf surface, where nano-scale features of each bump are visible; F – view of FSNP coating, with ~40-50 nm nanoparticles.

Each of the surfaces studied for magnetic actuation were also examined for both static WCA (different droplet sizes) and minimum ROA. Shown in Fig. 4.5 are images of 10 μL water droplets on each surface with associated measurement of CA in each case. The hydrophobic Teflon® AF surface (Fig. 4.5, left) shows a CA of only 115°, while both the FSNPs (Fig. 4.5, centre) with CA ~156° and the *Colocasia* leaf (Fig. 4.5, right) with CA ~152° are superhydrophobic as the CA exceeds 150°. Gravitational Bond number, a dimensionless measurement of droplet's ability to maintain spherical shape, determined by its surface tension and the density difference between the droplet and surrounding medium, was calculated to be less than unity for each of the surfaces confirming spherical droplet shape.[38]

116
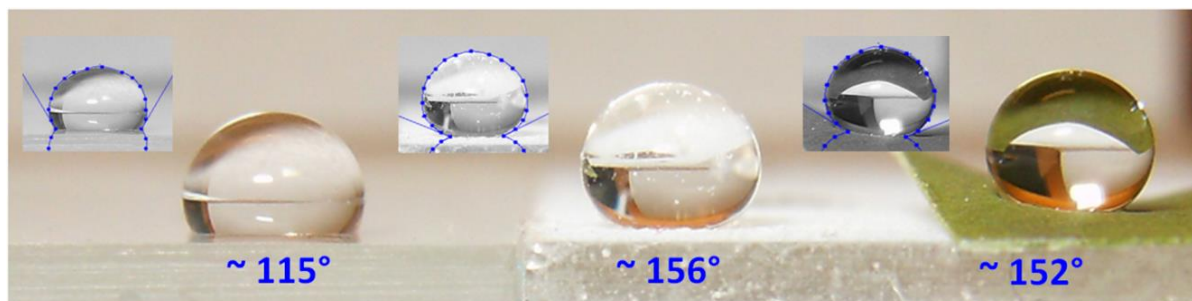
Figure 4.5: Contact angle of a 10 µL droplet of water with the surface coated with Teflon® AF (left); FSNPs (centre); and *Colocasia* leaf (right). In each case the inset shows the software-based contact angle measurement.

The effect of droplet size on the observed static CA was examined for the three surfaces. Fig. 4.6 shows the relationship between droplet size and the measured CA for each surface, where the measured CA decreases as the volume increases.
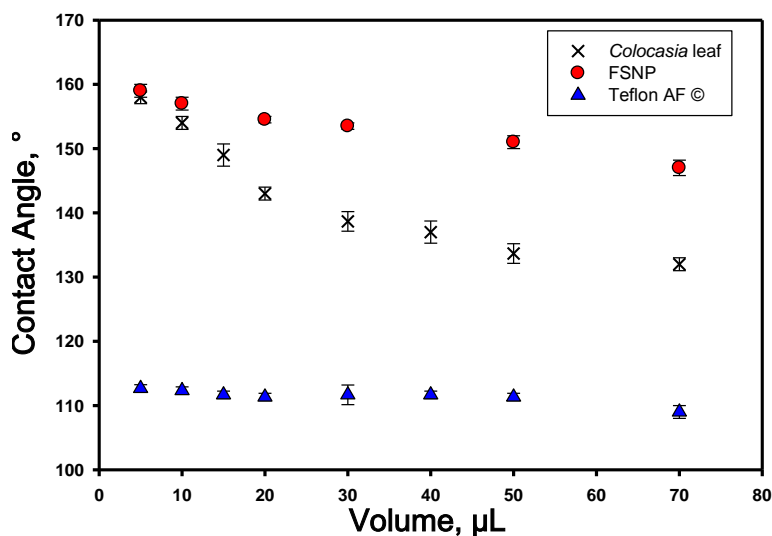
Figure 4.6: The relationship between the water droplet volume and the measured CA for the FSNP, *Colocasia* leaf and Teflon® AF surfaces. Error was calculated as an RSD value of 3 measurements.

As the mass of the droplet increases with volume, the effect of gravity forcing the droplet against the surface begins to affect the shape of the droplet.[39] This effect is not significant for surfaces that are close to "ideal", i.e. those which are hard, smooth and chemically homogeneous, like Teflon® AF. Less chemical homogeneity and more roughness lead to CA hysteresis, which in turn results in a greater dependence of the CA on droplet size.[40] For this reason, droplets larger than 10 µL are not

117

commonly used to measure CA. The data in Fig. 4.6 is consistent with this theory, showing a greater dependence of CA on droplet volume for the rougher, less homogeneous surfaces.

To facilitate magnetic actuation, superparamagnetic particles are added to the droplets. The effect of particle concentration on droplet CA was examined using water droplets with superparamagnetic particle concentrations ranging from 5-30 mg/mL dispensed on each of the surfaces. CAs were measured with and without an applied external magnetic field for each concentration of superparamagnetic particles (Fig. 4.7).
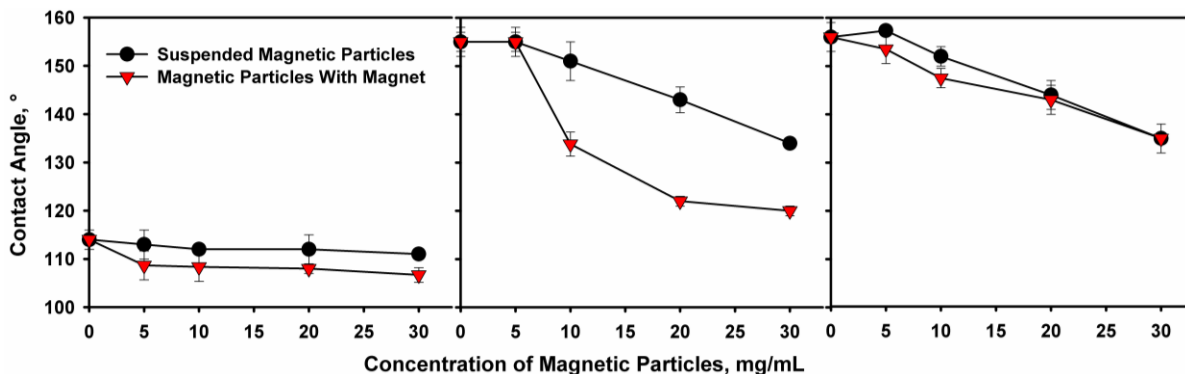
Figure 4.7: Relationship between the contact angle and the increasing concentration of magnetic particles with (▼) or without (●) applied magnetic field on Teflon® AF surface (left), *Colocasia* **surface (centre) and FSNP surface (right). Error was calculated as an RSD value of 3 measurements.**

It is common to observe significant droplet deformation and decrease in CA under applied magnetic field for ferrofluidic droplets – known as magnetowetting.[30] In the heterogeneous system described here, the initially suspended magnetic particles are drawn to the surface under an applied magnetic field thus creating a thin layer between the surface and the rest of the aqueous droplet (Fig. 4.8).
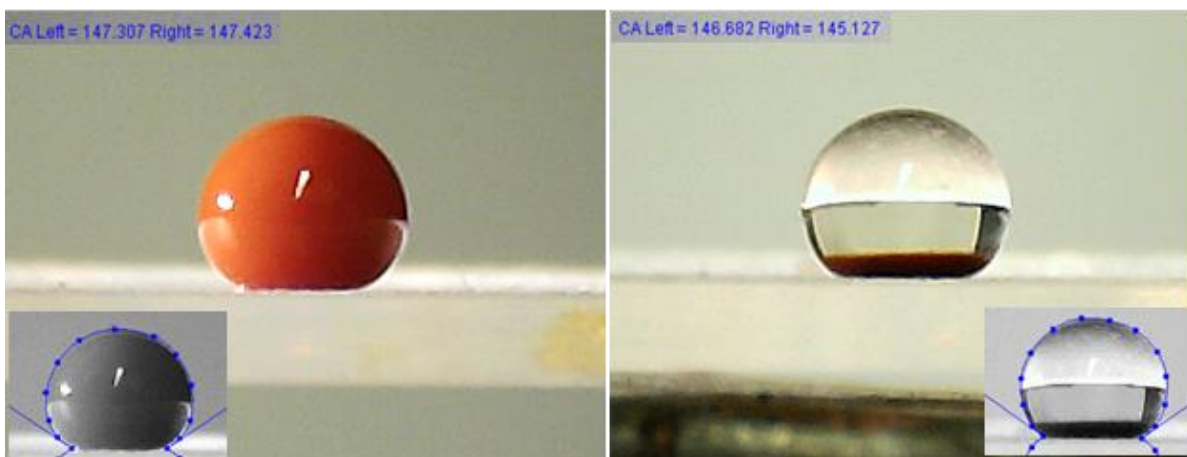
Figure 4.8: Optical microscope image a 10 µL droplet containing 20 mg/mL of suspended magnetic beads (left) and the same droplet under applied magnetic field (right). Inset shows CA assessment.

The water CA for the Teflon® AF surface was independent of particle concentration, indicating that particles associated with the surface do not appreciably alter the wetting characteristics of the material. In the presence of a magnetic field, particles suspended in the droplet become associated with the surface and a small 5° CA decrease is observed for the Teflon® AF. Particle concentration had a larger effect on the CA for *Colocasia* sample where it dropped from >150° to 130° with a particle concentration change (5 mg/mL to 30 mg/ mL). For the waxy leaf surface, superhydrophobicity arises from the hierarchical roughness of the surface, as shown in Fig. 4.4. We postulate that particles in the droplet become associated with the surface and begin to cover the nanostructures, diminishing the effect of roughness and aiding surface wetting. For the FSNP surface, which has only moderate micro-scale roughness but significant nanostructure, CA drops as particle concentration increases in the same manner as for the leaf surface. In the presence of a magnetic field, however, the drop in CA relative to droplets without the magnet was insignificant above 10 mg/mL particle concentration.

4.3.2 Roll-off Angles and Adhesion Force

ROAs measure the ability of a surface to shed a droplet and are determined by finding the tilt angle at which the surface can no longer hold the droplet. Minimal friction with the droplet is

particularly advantageous for self-cleaning surfaces commonly encountered in nature. Low RO angles (<10°) are another characteristic/requirement of superhydrophobic surfaces, but are similarly beneficial for magnetic actuation.

RO angles were measured for each of the three surfaces using water droplets of varying volume. The data in Fig. 4.9 shows decreasing ROA with increasing droplet size. As the mass of the droplet increases with volume, so does the force of gravity acting to make the droplet roll off. The additional frictional (adhesion) force arising from greater surface contact with larger droplets does not increase as rapidly with volume as the force of gravity, and so the net force shifts towards rolling off as the size increases.
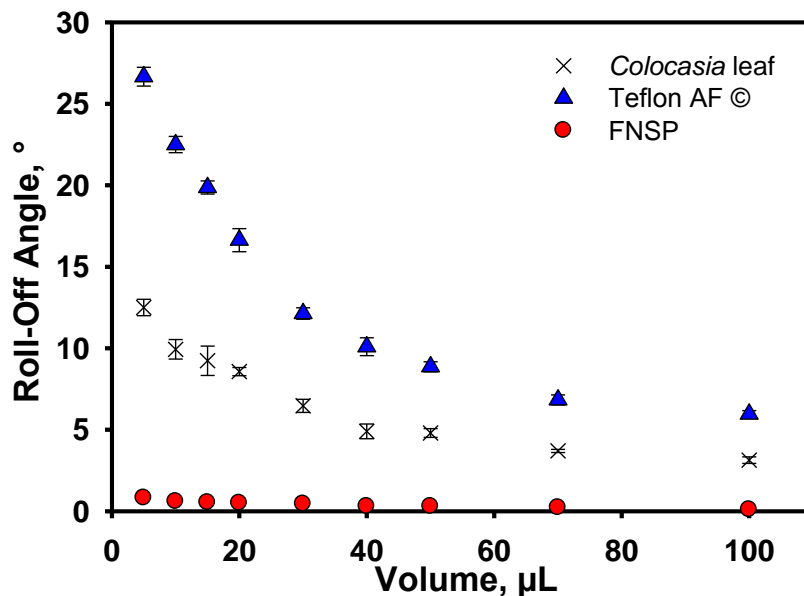
Figure 4.9: Roll-off angles measured for *Colocasia* leaf, Teflon® AF and FSNPs with varying volumes of water droplets. Error was calculated as an RSD value of 3 measurements.

For the superhydrophobic FSNP surface, it was difficult to stabilize the droplet, even on a leveled horizontal surface. The ROA was measured to be <1°. The RO angles of the superhydrophobic leaf were found to range from 3° to 12°, and the hydrophobic Teflon® AF surface was found to have RO angles ranging from 6° to 30°. This trend follows the hydrophobicity of the surfaces as determined by static CA measurements, where lower RO angles correlate with higher CAs. ROAs were also

measured for 10 μL droplets containing suspended magnetic particles with or without applied magnetic field (Fig. 4.10). The RO angles for droplets in the absence of magnetic field had little dependence on the concentration of magnetic particles suspended within them. The force maintaining droplet position stems from the friction induced by contact of the droplet with the surface, and with such little contact, the droplets easily roll off the surface. When the particles are introduced in the droplet, some become associated with the surface, and so the force holding the droplet in place becomes a combination of the wetting forces between the droplet and particles (alongside surface tension acting to hold the particles within the droplet) and the friction forces between the particles and surface. In the absence of a magnetic field the adhesion of particles to the surface does not significantly change with increasing particle concentration, explaining the lack of dependence of ROA on particle concentration. For the *Colocasia* leaf surface, however, the ROA increases with particle concentration. Unlike the FSNP and Teflon® AF surfaces, the leaf surface has microstructure on the same scale as the paramagnetic particles. Some particles are retained by features on the surface enhancing the frictional component of the force holding the droplet. Increasing particle concentration leads to a larger ROA. Whenever magnetic particles were deposited on the leaf surface for either RO tests or actuation, residual magnetic particles were observed on the surface of the leaf.
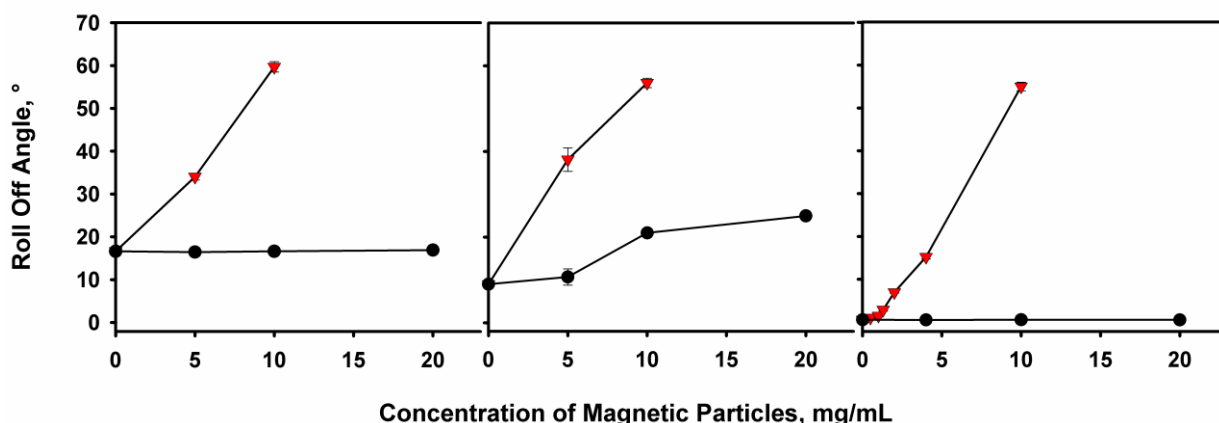
Figure 4.10: Roll-off angles for surfaces with 10 μL droplets having varying particle concentrations with (▼) and without (●) applied magnetic field: Teflon® AF (left); *Colocasia* Leaf surface (centre); FSNP surface (right). Error was calculated as an RSD value of 3 measurements.

121

The addition of superparamagnetic particles to the droplet enables the droplet to be easily captured on a superhydrophobic surface where the RO angle would otherwise be <1°, an ideal situation for a device based on droplet manipulation. Regardless of the intrinsic hydrophobicity of the surface, the forces retaining the droplet were strong enough to entirely prevent the droplet from rolling off when the concentration of the magnetic particles was > 20 mg/mL. In fact, surfaces could be completely inverted without the droplet breaking contact. The relationship between RO angle and particle concentration above 5 mg/mL is nearly independent of the type of surface suggesting the component of the force associated with the friction between the droplet and surface is less significant when magnetic particles are in the presence of the magnetic field. Fig. 4.11 shows the inverted water droplets containing magnetic particles when an external magnetic field is applied on the *Colocasia* leaf and the FSNP surface.
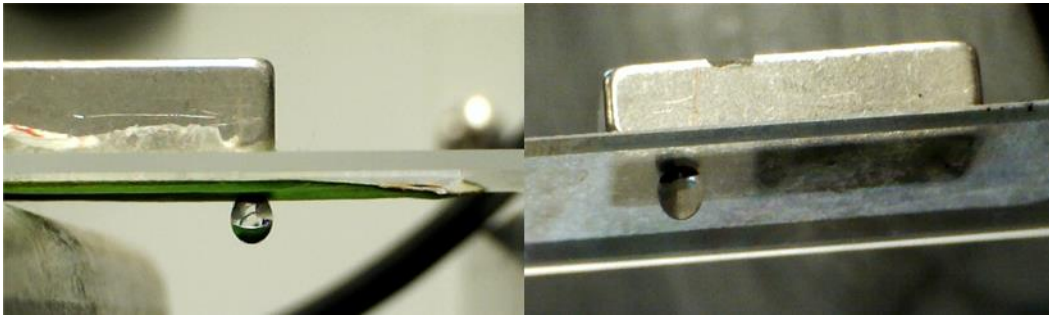
Figure 4.11: Inverted surface of a glass slide with attached *Colocasia* leaf (left) and FSNP layer (right), where the 20 µL droplet of water is retained on the surface due to the presence of 20 mg/mL paramagnetic particles in a magnetic field.

A droplet with magnetic particles held on the inclined surface under applied magnetic field experiences an adhesion force which is a combination of frictional force with the surface, a magnetic force exerted on the particles, and a wetting force between the hydrophilic particles and aqueous droplet. ROA measurements establish that a gravitational force can move a droplet if it overcomes the adhesion force generated by the contact of the droplet on the surface. The collective total surface adhesion force (i.e. $\vec{F}_{\text{adhesion}} = \vec{F}_{\text{friction}} + \vec{F}_{\text{magnetic}} + \vec{F}_{\text{wetting}}$) can be calculated from the ROA using (Eqn. 4.1)*:*

$$\vec{F}_{adhesion} = m \cdot g \cdot sin\Theta \qquad \qquad \text{(Equation 4.1)}$$

where m is mass of the droplet, g is standard acceleration of free fall and Θ (in radians) is the RO angle (Table 4.1). In the conditions explored here, the wetting force is always higher than the magnetic force and particles were carried away by the droplet after the critical ROA is achieved. At higher particle concentration and complete inversion, the droplet remains attached to the hydrophilic patch formed by the particles. Complete inversion on all three surfaces is achieved at > 20 mg/mL particle concentrations.

Table 4.1: Roll-off angle and corresponding $\vec{F}_{adhesion}$ for a 10 µL droplet with different concentrations of superparamagnetic beads on three surfaces under an applied magnetic field.

Bead Concentration, mg/mL	Roll-off Angle with Magnet, °			Total Adhesion Force, µN		
	Colocasia	Teflon® AF	FSNPs	*Colocasia*	Teflon® AF	FSNPs
0	9.0±0.5	16.6±1.0	0.6±0.1	15.3±0.9	28.0±1.6	0.9±0.1
5	38.1±2.7	34.0±0.8	27.8±1.4	60.3±4.6	54.7±1.3	45.6±2.0
10	56.0±1.1	59.7±1.2	55.0±1.0	81.1±2.2	84.4±1.7	80.1±1.5
20	180° inversion			> 97.8±1.2		

4.3.3 Droplet Actuation and Superparamagnetic Particle Concentration

Droplet actuation on the surface of a device is governed by a collection of forces on the droplet. With high enough surface particle density, the wetting force retaining the droplet was found to overcome the force of gravity and the surface could be completely inverted with no droplet disengagement. This strong wetting force between the particles and the droplet is at the heart of droplet actuation by magnetic particles. The particles are strongly attracted to the external magnetic field, and as the magnet is moved, the water droplet stays attached to the particles as it is pulled by the wetting force. Simply by moving a bar magnet, for example, the magnetic particles can be made to lead the water droplet around a surface, the movement being hindered only by the frictional forces between the particles and the surface and between the droplet and the surface (characterized by the droplet's CA).

The ability of the external magnet to actuate droplets was explored for the three surface types. Teflon® AF, a common hydrophobic surface used in DMF applications, shows much lower WCAs than the other surfaces studied, resulting in poor magnetic actuation performance. This surface exhibits too much adhesion/friction for smooth droplet motion, and would require considerably higher concentrations of magnetic particles to operate.[30] The natural superhydrophobic surface, the *Colocasia* leaf, displays WCA of over 150°, where very facile droplet motion can be achieved with relatively low concentrations of magnetic particles. However, the surface shows significant deterioration with time, where magnetic particles damage the surface and individual beads become trapped in the surface microstructure. Furthermore, the leaf cannot be attached easily to most surfaces, and its properties change as it dries, which also makes it brittle and difficult to handle. Combined with seasonal availability, these properties make the natural leaves impractical for DMF applications. The UED surface, a fluorinated silica nanoparticle-based coating, showed the best magnetic actuation performance. Smooth surface actuation was obtained and no difference in contact advancing and receding contact was detectable with our experimental apparatus.

For these reasons, the FSNP surface was used to study the effects of particle concentration and droplet size on droplet actuation. Droplets (10 µL) containing various particle concentrations were deposited onto the FSNP surface using a pipette with a disposable plastic tip, in the presence of a magnetic field. A practical lower limit in particle concentration was reached at 0.4 mg/mL where it became difficult to both deposit and maintain the droplet on the surface. To overcome this challenge, 10 µL droplets containing 0.4 mg/mL particles were deposited and subsequently diluted with water to reduce particle concentration. In this way, droplets diluted to 0.1 mg/mL (i.e. 40 µL droplets) could be magnetically actuated, but disengagement became more frequent. Actuation of 10 µL droplets was, however, consistently smooth and efficient at concentrations of magnetic particles above 1 mg/mL. Actuation of droplets with different volumes (10 µL to 300 µL) containing 1 and 2 mg/mL of particles was also performed using a magnet. Larger droplets exhibited splitting, limiting predictable actuation

124

behaviour to droplets ≤90 µL. Actuation of droplet volumes that exceeded 90 µL generally produced two smaller droplets in which only one contained magnetic particles.

4.3.4 Droplet Actuation Velocity

An important consequence of the high WCA of the UED coating is the ability of the droplet to be actuated with little frictional resistance and rapidly slide over the surface. Fast actuation over the surface is beneficial for many applications where sample processing or analysis time can be reduced by rapid droplet translocation. Actuation speeds achievable with magnetically actuated droplets have been previously reported to be in the range of 2 to 20 mm/s for Teflon® AF[10,27] and around 70 mm/s for superhydrophobic surfaces.[11] The FSNP coating offers reduced friction (higher WCA), thus allowing for higher operational speed under otherwise similar conditions. To determine the speed of the droplet a glass slide was marked with a 30 mm region as shown in Fig. 4.12.
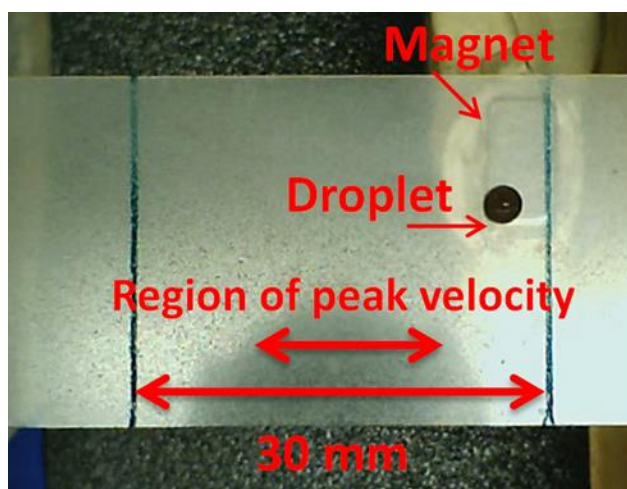
Figure 4.12: The experimental set-up used to measure the actuation speed of the droplet containing superparamagnetic particles on superhydrophobic surface. A 30 mm distance was marked on the underside of a glass slide coated with FSNPs, and the droplet was manually actuated over this distance using a magnet placed under the slide. The average speed was determined by measuring the time it takes the droplet to travel over the 30 mm distance. The small arrow above indicates the distance over which the maximum speed was measured.

There are three different events that can be observed when a droplet is actuated over the surface: steady motion, magnet disengagement, and particle removal.[10,41] For small droplet sizes (≤20 µL), no bead extraction or disengagement was observed at particle concentrations of 20 mg/mL. Under

125

these conditions, the FSNP surface allowed for very smooth and steady droplet movement without observable magnet disengagement at average speeds readily exceeding 250 mm/s, which to our knowledge is the highest velocity reported with a manually controlled magnet. The maximum (peak) speed that was measured over a distance near the middle of the slide, as the magnet begins to decelerate after accelerating, was in excess of 550 mm/s. In general, for the UED surface, actuation failure at higher speeds was by particle removal at larger droplet volume (>50 µL) and high bead concentration (≥20 mg/mL), but otherwise by magnet disengagement.

4.3.5 Solvent Robustness of UED

Traditional analytical techniques often require the use of various organic solvents. The UED surface was tested in terms of its stability and robustness when employed with various proportions of acetonitrile (ACN) and methanol. CAs of droplets of these solutions on the FSNP surface were also investigated.

Presented in Fig. 4.13 are CAs for pure ACN and pure methanol on the FSNP surface as a function of droplet volume, with water CAs included for comparison.
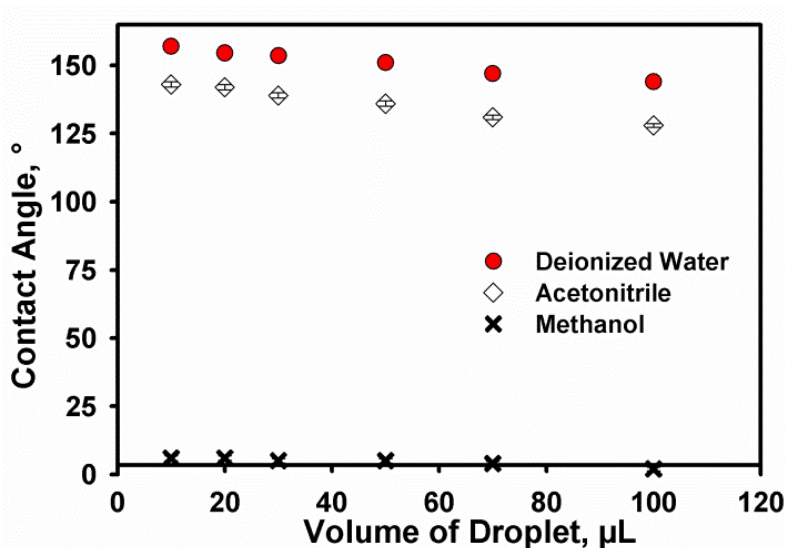
Figure 4.13: Contact angle of droplets of water, acetonitrile and methanol were measured as a function of droplet size on the FSNP surface.

126

For each solvent type, the expected trend towards decreasing CAs with increased droplet volume was observed, a result of increasing influence of gravity with increasing droplet mass. In general, the CAs for ACN droplets were lower than for water, reflecting the ability of the solvent to better wet the surface. Methanol droplets, on the other hand, almost completely wetted the UED surface, leading to CAs <10°. Increased wetting by these solvents on a fluorous surface is not surprising as methanol, and to a lesser extent ACN, are considered "fluorophilic" solvents commonly used in fluorous-phase chromatography.[42] In the case of UED, where fluorous particles are affixed to a surface with a bonding material, wetting of the surface with organic solvents leads to the particles becoming dislodged and the bonding material being damaged. Indeed, FSNP surfaces treated with ACN became discoloured afterward, and when methanol was used, the surface appeared damaged and no longer exhibited superhydrophobic character with water. The manufacturer of UED, UltraTech International Inc., indicates that UED has poor resistance to solvents with surface tension below 30 mN/m.

To establish the tolerance of the FSNP surface to these solvents, CAs of droplets containing 0-100% (v/v) ACN or methanol in water were measured. As the concentration of ACN in the droplet increased, the CAs decreased (data not shown). The CA drops below 150° at ACN concentration of 50% and above, resulting in the loss of superhydrophobicity. However, even pure ACN exhibits CA of above 140° on FSNPs and can be reproducibly actuated over the surface. Increasing concentration of methanol in a droplet also causes a decrease in the static CA on the FSNP surface, as shown in Fig. 4.14. There is a sharp drop in CA above ~80% methanol (v/v), presumably marking the point where the solvent is able to wet the surface enough to damage the base coat and dislodge the particles. Indeed, when the methanol content in the droplet exceeded 85% (v/v), the UED surface became severely damaged and lost its superhydrophobicity. Photograph inserts in Fig. 4.14 show the FSNP surface with droplets containing 90 and 100% methanol, showing the rapid decline in CA with methanol content associated with surface damage, which can be seen clearly in Fig. 4.15. Furthermore,

methanol caused more damage to the surface than ACN at much lower concentration, where even at 25% methanol (v/v) the FSNP surface starts to deteriorate.
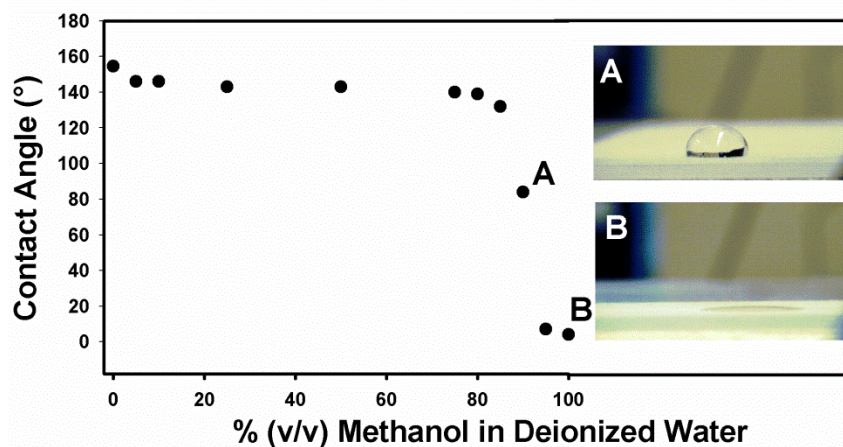
Figure 4.14: Contact angle of a 20 μL droplet with increasing concentration of methanol in water on the FSNP surface. Insert photographs show the droplets at high concentrations of methanol: surface starts to wet at 90% methanol (A); completely wetted surface at 100% methanol (B).

Figure 4.15: Top view of the FSNP surface following exposure to 100% methanol.

4.3.6 Magnetic Particle Cluster Extraction

It was demonstrated that droplets contacting magnetic particles can be precisely and reproducibly actuated over a superhydrophobic surface; some applications however require the droplets to be stationary, where the magnetic beads can be removed and reused again. A requirement for this system is the region of lower hydrophobicity on the surface, where the droplets can be selectively anchored. A variety of ways exist to modify the hydrophobic/hydrophilic properties of the

surface, including masking and UV exposure, composite films, plasma treatment etc.[43,44] In order to create a region of reduced hydrophobicity on the otherwise superhydrophobic surface, nitrocellulose patches (CA 58°) were created using nail polish. In this case, the magnetic beads, i.e. the magnetic cluster, can be selectively extracted from the droplet by a magnetic force, whereas the aqueous droplet would stay pinned on the more hydrophilic (less hydrophobic) patch (Fig. 4.16).
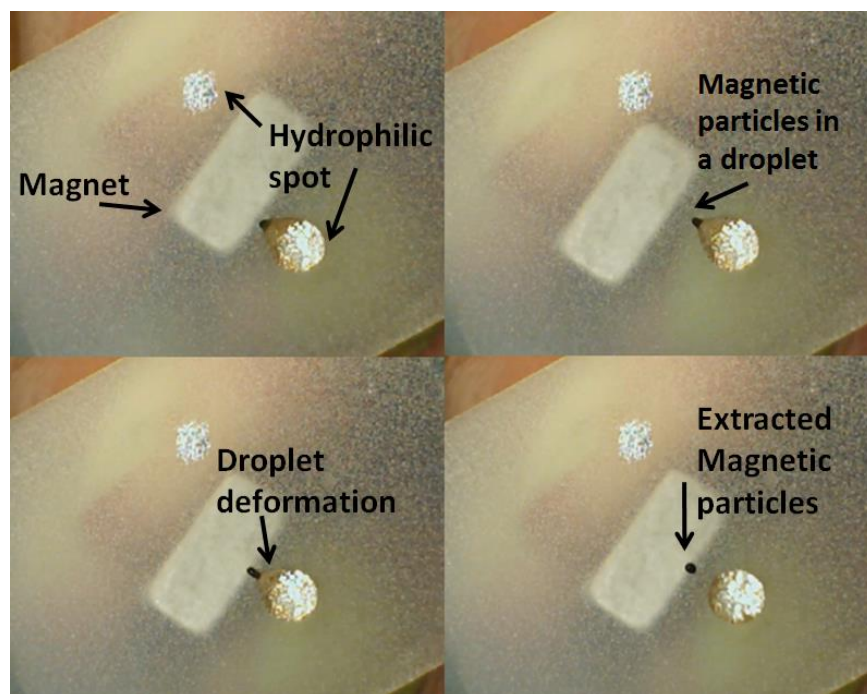
Figure 4.16: Removal of paramagnetic particle cluster (20 mg/mL) from a 20 µL water droplet anchored to a spot with reduced hydrophobicity.

Optimal conditions for the particle extraction, i.e. concentration of the magnetic particles and solvent compositions, were determined. It was previously demonstrated that the magnetic force acting on the cluster is proportional to the weight of the magnetic bead cluster;[45] we determined the minimum particle cluster weight at different combinations of water/acetonitrile mixture (Table 4.2).

Table 4.2: Minimum magnetic particle cluster mass and corresponding concentration in a droplet with various water/acetonitrile compositions.

% Acetonitrile (v/v)	Surface tension,[46] mN/m	Minimum Particle Cluster Mass, mg	Concentration of Magnetic Particles in 20 μL droplet, mg/mL
0	72.8	0.4	20
25	39.8	0.2	7
50	33.1	0.1	5

As seen in Fig. 4.16, the cluster extraction is initiated by the droplet shape deformation, where the magnetic force on the cluster is causing droplet elongation. Aqueous droplets tend to maintain their shape due to high surface tension, however when acetonitrile is added the surface tension significantly decreases (i.e. from ~ 72.8 mN/m to ~33.1 mN/m at 50% acetonitrile).[46] This reduction in the surface tension of the water/acetonitrile mixture aids in the droplet deformation, which in turn facilitates cluster extraction. From Table 4.2 it is evident that under the same applied magnetic force (i.e. the same magnet used) less magnetic particles are required for reproducible extraction. A wide range of droplet sizes was tested (20 to 80 μL), where the extraction efficiency was only dependent on the actual mass of the cluster, and not the droplet size. The larger sized droplets were more difficult to anchor on the hydrophilic patch, and they often would break up into smaller irregularly sized droplets. A mixture containing 75% (v/v) of acetonitrile was tested, however both the coating and the hydrophilic patch started to disintegrate, thus only concentrations of up to 50% (v/v) are practically usable.

Anchored droplets can be supplied with reagent to conduct sample dilution, colorimetric assays and titrations. Fig. 4.17 demonstrates an example of a simple colorimetric acid-base titration, where an anchored droplet of acetic acid (1.0 M) (with phenolphthalein indicator) was titrated with basic droplets (0.5 M NaOH) until the colorimetric end-point, i.e. it turned pink.
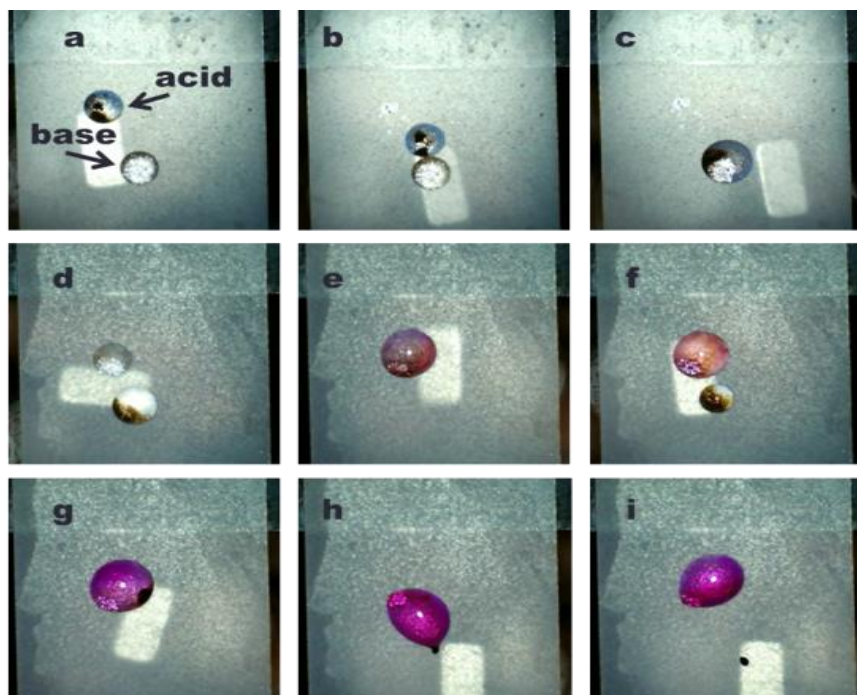
Figure 4.17: Titration of pinned acetic acid droplet (containing phenolphthalein) with sodium hydroxide droplets, where magnetic cluster is repeatedly removed from the stationary acidic droplet and additional basic solution is delivered by the same cluster until the color change can be observed.

4.3.7 Two-Plate Droplet Manipulation

We have also explored the possibly of using a two-plate set-up with our system, where two UED coated glass slides were separated by a known distance, and the droplet containing superparamagnetic beads was positioned between those plates. Depending on the distance, droplet volume and the amount of paramagnetic beads different droplet actuation mechanisms can be observed: droplet can be actuated from the top while staying on the bottom plate; droplet containing magnetic particles is transferred to the underside of the top plate and can be actuated from the top; the bead cluster is extracted to the top plate, while the left over aqueous droplet rolls away in a random direction (Fig. 4.18).

131
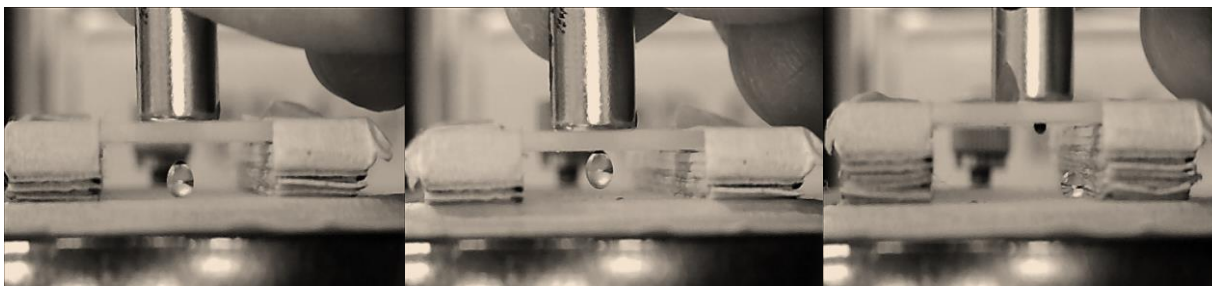
Figure 4.18: Various mechanisms of two-plate droplet actuation. (left) Magnetic bead cluster is attracted to the magnet, however remains within the droplet on the bottom plate; droplet can be actuated from the top, while remaining on the bottom slide. (centre) Magnetic bead cluster and the droplet are both transferred to the top plate, and can be actuated from the top while remaining suspended from the underside of the top plate. (right) Magnetic bead cluster is extracted from the surrounding droplet and transferred to the plate, where it can be actuated from the top; the remaining water droplet rolls-off in a random direction.

The mechanism of two-plate actuation is determined by several factors: the length of the gap between two plates, the mass of the magnetic particles in the droplet (determined from the concentration dispensed), and the size of the droplet, along with the strength of the magnet which was not investigated here. If the gap is too big or the particle concentration is too low, the droplet cannot be actuated; a large droplet in a small gap would contact both plates, thus only the top actuation mechanism would be possible. Fig. 4.19 summarizes possible actuation mechanism for a constant droplet size (10 μL) with changing gap size and magnetic bead concentrations. Fig. 4.20 demonstrates possible actuation mechanisms for a droplet of constant magnetic particle concentration (6 mg/mL) at varying gap distance and variable droplet volumes (5, 10 and 15 μL).
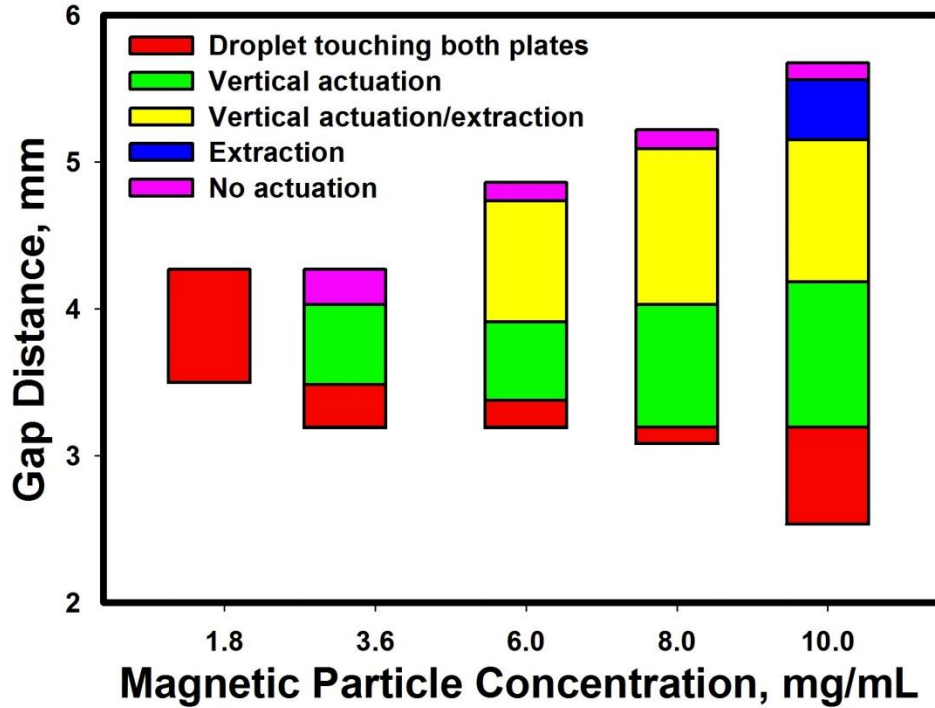
Figure 4.19: Possible actuation mechanisms of a 10 μL droplet containing varying concentrations of magnetic particles at different gap lengths.
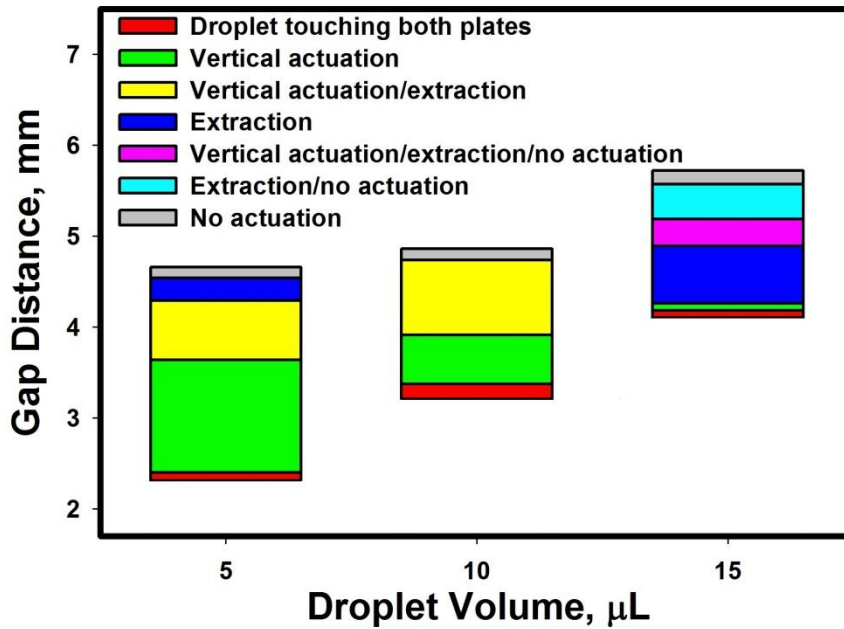
Figure 4.20: Possible actuation mechanisms of a droplet containing 6 mg/mL magnetic particles with varying volume at different gap lengths.

133

Data presented in Figure 4.19 and 4.20 shows that at low concentrations (<3.6 mg/mL) the actuation is not possible. No actuation was observed for large gap distances, i.e. above 6 mm for the maximum concentrated tested of 10 mg/mL. As the concentration of magnetic particles increases at a constant volume, it becomes easier to extract the magnetic cluster, where the extraction and mixed mechanisms become predominant. Higher concentrations of magnetic particles also allow manipulating the droplet at larger gap distances. Larger droplet volumes are also more prone to extraction/mixed mechanisms, as the droplet becomes heavier it becomes harder to transfer the droplet to the top plate, and it is also easier to extract the particle cluster. Overall, it is possible to manipulate a droplet contacting magnetic particles on a two-plate system, where gap length, droplet volume and magnetic particles concentration determine the mechanism and the efficiency of actuation.

4.4 Conclusion

Digital microfluidic devices require surfaces that offer as little frictional resistance as possible in order to facilitate droplet movement. This chapter looked on three hydrophobic surfaces and their effectiveness in being used for magnetic actuation. Teflon® AF, a common hydrophobic surface used in DMF applications, shows lower WCAs than would be considered superhydrophobic, resulting in poor magnetic actuation performance. This surface exhibits too much friction for smooth droplet motion, and requires considerably higher concentrations of superparamagnetic particles than do the other surfaces to exhibit magnetic droplet actuation. A natural superhydrophobic surface, *Colocasia* leaf, displays CAs of over 150°, where facile droplet motion can be achieved with low concentrations of magnetic particles. However, the surface shows deterioration with time as the leaf dries and as the magnetic particles damage the surface features, where individual particles were found to be trapped among these features. A commercially available superhydrophobic material, proved to be the most amenable to magnetic actuation applications. High static WCAs and very low ROAs demonstrated the lack of frictional resistance to droplet movement on this surface. Despite this, strong wetting forces between the water droplet and commercially available superparamagnetic particles, along with surface

134

tension of the droplet, keep the droplet associated with the particles. Above a certain particle concentration for a specific droplet volume, in the presence of a magnetic field generated by a simple magnet, the droplet can be held in place at any tilt angle, even when completely inverted. Movement of the magnet causes movement of the particles, and hence the entire droplet, over the device surface. The very low frictional resistance to movement offered by the FSNP surface allows droplets to be actuated with relatively low concentrations of magnetic particles and with high speeds of over 550 mm/s. The UED surface also showed relatively good robustness to magnetic bead abrasion, and was found to be resistant to pure ACN and methanol $\leq$25% v/v. Alternative droplet manipulation techniques, i.e. two-plate actuation and surface patterning with hydrophilic regions was successfully demonstrated on UED surface coating. Ultimately, a commercial coating material comprising fluorinated particles affixed to an adhesive undercoat, showed superior performance to a natural superhydrophobic surface (*Colocasia* leaf) and a commercial fluorinated polymer film (Teflon® AF) for droplet actuation by magnetic manipulation of superparamagnetic particles in a water droplet. UED possesses many properties amenable to digital microfluidic applications for magnetic actuation.

4.5 References

1.   M. Abdelgawad and A. R. Wheeler, *Adv. Mater.*, 2009, **21**, 920-5.

2.   R. Sista, Z. S. Hua, P. Thwar, A. Sudarsan, V. Srinivasan, A. Eckhardt, M. Pollack and V. Pamula, *Lab Chip*, 2008, **8**, 2091-104.

3.   K. H. Kang, *Langmuir*, 2002, **18**, 10318-22.

4.   J. Zeng and T. Korsmeyer, *Lab Chip*, 2004, **4**, 265-77.

5.   R. Bavière, J. Boutet and Y. Fouillet, *Microfluid. Nanofluid.*, 2007, **4**, 287-94.

6.   I. Moon and J. Kim, *Sens. Actuators A: Phys.*, 2006, **130-131**, 537-44.

7.   H. Moon, S. K. Cho, R. L. Garrell and C.-J. C. Kim, *J. Appl. Phys.*, 2002, **92**, 4080.

8.   S. K. Cho, H. J. Moon and C. J. Kim, *J. Microelectromech. Syst.*, 2003, **12**, 70-80.

9.   V. N. Luk, G. C. H. Mo and A. R. Wheeler, *Langmuir*, 2008, **24**, 6382-9.

10.   Z. Long, A. M. Shetty, M. J. Solomon and R. G. Larson, *Lab Chip*, 2009, **9**, 1567-75.

11.   A. Egatz-Gomez, S. Melle, A. A. Garcia, S. A. Lindsay, M. Marquez, P. Dominguez-Garcia, M. A. Rubio, S. T. Picraux, J. L. Taraci, T. Clement, D. Yang, M. A. Hayes and D. Gust, *Appl. Phys. Lett.*, 2006, **89**, 034106.

12.   N. T. Nguyen, *Microfluid. Nanofluid.*, 2012, **12**, 1-16.

13.   A. A. García, A. Egatz-Gómez, S. A. Lindsay, P. Domínguez-García, S. Melle, M. Marquez, M. A. Rubio, S. T. Picraux, D. Yang, P. Aella, M. A. Hayes, D. Gust, S. Loyprasert, T. Vazquez-Alvarez and J. Wang, *J. Magn. Magn. Mater.*, 2007, **311**, 238-43.

14.   A. H. C. Ng, K. Choi, R. P. Luoma, J. M. Robinson and A. R. Wheeler, *Anal. Chem.*, 2012, **84**, 8805-12.

15.   Y. T. Cheng, D. E. Rodak, C. A. Wong and C. A. Hayden, *Nanotechnology*, 2006, **17**, 1359-62.

16.   K. Koch, A. Dommisse and W. Barthlott, *Cryst. Growth Des.*, 2006, **6**, 2571-8.

17.   H. J. Ensikat, P. Ditsche-Kuru, C. Neinhuis and W. Barthlott, *Beilstein J. Nanotechnol.*, 2011, **2**, 152-61.

18.   A. B. D. Cassie and S. Baxter, *T. Faraday Soc.*, 1944, **40**, 0546-50.

19.   Z. J. Cheng, H. Lai, N. Q. Zhang, K. N. Sun and L. Jiang, *J. Phys. Chem. C*, 2012, **116**, 18796-802.

20.   A. Egatz-Gómez, J. Schneider, P. Aella, D. Yang, P. Domínguez-García, S. Lindsay, S. T. Picraux, M. A. Rubio, S. Melle, M. Marquez and A. A. García, *Appl. Surf. Sci.*, 2007, **254**, 330-4.

21.   X. Zhang, F. Shi, J. Niu, Y. Jiang and Z. Wang, *J. Mater. Chem.*, 2008, **18**, 621-33.

22.   J. Schneider, A. Egatz-Gómez, S. Melle, S. Lindsay, P. Domínguez-García, M. A. Rubio, M. Márquez and A. A. García, *Colloids Surf., A*, 2008, **323**, 19-27.

23.   M. Ma and R. M. Hill, *Curr. Opin. Colloid Interface Sci.*, 2006, **11**, 193-202.

24. Z. G. Guo, F. Zhou, J. C. Hao, Y. M. Liang, W. M. Liu and W. T. S. Huck, *Appl. Phys. Lett.*, 2006, **89**, 081911.

25. X. Hong, X. F. Gao and L. Jiang, *J. Am. Chem. Soc.*, 2007, **129**, 1478-9.

26. E. Bormashenko, R. Pogreb, Y. Bormashenko, A. Musin and T. Stein, *Langmuir*, 2008, **24**, 12119-22.

27. U. Lehmann, S. Hadjidj, V. K. Parashar, C. Vandevyver, A. Rida and M. A. M. Gijs, *Sens. Actuat. B-Chem.*, 2006, **117**, 457-63.

28. H. Wang, J. Fang, T. Cheng, J. Ding, L. Qu, L. Dai, X. Wang and T. Lin, *Chem. Commun.*, 2008, 877-9.

29. N. Gao and Y. Y. Yan, *Nanoscale*, 2012, **4**, 2202-18.

30. N. T. Nguyen, G. Zhu, Y. C. Chua, V. N. Phan and S. H. Tan, *Langmuir*, 2010, **26**, 12553-9.

31. W. Hang Koh, K. Seng Lok and N.-T. Nguyen, *J. Fluids Eng.*, 2013, **135**, 021302.

32. J. F. Nie, Y. Zhang, H. Wang, S. P. Wang and G. L. Shen, *Biosens. Bioelectron.*, 2012, **33**, 23-8.

33. H. Chen, A. Abolmatty and M. Faghri, *Microfluid. Nanofluid.*, 2011, **10**, 593-605.

34. N. S. Mei, B. Seale, A. H. C. Ng, A. R. Wheeler and R. Oleschuk, *Anal. Chem.*, 2014, **86**, 8466-72.

35. I. Pushkarsky, P. Tseng, C. Murray and D. Di Carlo, *Lab Chip*, 2014, **14**, 2882-6.

36. M. Yu, G. Gu, W.-D. Meng and F.-L. Qing, *Appl. Surf. Sci.*, 2007, **253**, 3669-73.

37. S. C. C. Shih, R. Fobel, P. Kumar and A. R. Wheeler, *Lab Chip*, 2011, **11**, 535-40.

38. S. R. Hodges, O. E. Jensen and J. M. Rallison, *J. Fluid Mech.*, 2004, **512**, 95-131.

39. L. Afferrante and G. Carbone, *Soft Matter*, 2014, **10**, 3906-14.

40. J. Drelich, *J. Adhes.*, 1997, **63**, 31-51.

41. N. Vergauwe, S. Vermeir, J. B. Wacker, F. Ceyssens, M. Cornaglia, R. Puers, M. A. M. Gijs, J. Lammertyn and D. Wittersaabios, *Sens. Actuat. B-Chem.*, 2014, **196**, 282-91.

42. Z. P. Xu, G. T. T. Gibson and R. D. Oleschuk, *The Analyst*, 2013, **138**, 611-9.

43. K. Nakata, K. Udagawa, T. Ochiai, H. Sakai, T. Murakami, M. Abe and A. Fujishima, *Mater. Chem. Phys.*, 2011, **126**, 484-7.

44. A. Ghosh, R. Ganguly, T. M. Schutzius and C. M. Megaridis, *Lab Chip*, 2014, **14**, 1538-50.

45. M. Shikida, K. Takayanagi, K. Inouchi, H. Honda and K. Sato, *Sens. Actuat. B-Chem.*, 2006, **113**, 563-9.

46. W. J. Cheong and P. W. Carr, *J. Liq. Chromatogr.*, 1987, **10**, 561-81.

Chapter 5

"Particle-free" Magnetic Actuation of Droplets on Superhydrophobic

Surfaces Using Dissolved Paramagnetic Salts

5.1 Introduction

Digital microfluidics (DMF) has being steadily gaining popularity in the field of analytical chemistry, as it offers the advantages of standard "in-channel" techniques along with the ability to independently control individual droplets.[1,2] However, the high pressures and complex closed channel architectures required to move liquids though a channel-containing device are negated.[3] Furthermore, complex pumps and interconnections are not needed, which can significantly reduce manufacturing complexity, time and cost.[4] DMF device fabrication is compatible with inexpensive and rapid batch processing.[5] Individual nanolitre- to microlitre-sized droplets can be actuated, split and combined as desired, and these processes can be carried out in a parallel fashion.[2,6] Chemical and biochemical sample preparations/assays can be conducted in confined droplets on a DMF platform.[7-11]

Multiple droplet actuation mechanisms for DMF devices exist, with electrowetting-on-dielectric,[1,12] acoustic wave,[13] and dielectrophoresis[14] being the most popular. Magnetic actuation, however, is both an interesting and facile alternative actuation method, where individual droplets containing paramagnetic particles are moved over a (super)hydrophobic surface using a magnet.[15,16] This technique requires little fabrication, where only a low friction surface, particle-containing droplet (i.e. superparamagnetic beads or ferrofluids) and a magnet are required.[6,17] Droplet movement is a result of a magnetic field gradient, magnetic force produced by the particles interacting with the magnet, and the surface tension of the fluid which maintains the particles within the droplet. Aqueous droplets remain attached to the paramagnetic particles, which "anchors" the droplet to an otherwise water repellant surface.[18-20] The magnetic force acting on a droplet can be approximated by eqn. 5.1 (adapted from reference18):

$$\overrightarrow{F_m} = V_{particles}\chi\frac{B_m}{\mu_0}\nabla B_m \hspace{4cm} \textit{Equation 5.1}$$

where $V_{particles}$ refers to the volume of the magnetic material in the droplet, χ is the magnetic susceptibility of the magnetic material, B_m is the applied magnetic field, and μ_0 is the permittivity of free space.

To actuate the droplet $\overrightarrow{F_m}$ the must exceed the force holding the droplet in place, i.e. the frictional force ($\overrightarrow{F_f}$):

$$\overrightarrow{F_f} \cong K_f R_{base}\vec{U} \hspace{4cm} \textit{Equation 5. 2}$$

where F_f refers to the frictional force, K_f is a friction constant, R_{base} is the radius of the bottom contact area between droplet and the surface and $\vec{U}$ is the droplet velocity. As the magnet is moved underneath the substrate/surface the packet of paramagnetic particles is moved in the same direction due to magnetic force gradient, and the droplet can be actuated over the surface when the particles remain in the droplet due to surface tension.

Currently, magnetic actuation studies have focused upon the addition of particles with high magnetic susceptibility to manipulate the droplets. Initial studies utilized crude micron-sized iron oxide particles[20], however superparamagnetic particles of more well-defined size, composition and surface chemistries are now employed.[21,22] Here we present a novel approach for "particle-free" magnetic actuation using paramagnetic salts. Paramagnetic salts have been previously utilized in applications to levitate non-magnetic particles,[23,24] or to control the flow of non-magnetic particles via negative magnetophoresis.[25,26]

Despite possessing magnetic susceptibilities as much as four orders of magnitude less than that of a superparamagneic and ferromagnetic materials,[27] we show that droplets containing sufficient paramagnetic salt concentrations can be directly actuated over a superhydrophobic surface by a magnet. This actuation can be carried out without the need for an oil layer encapsulating the droplet, as superhydrophobic surfaces provide reduced friction.[17] Five paramagnetic salts with magnetic susceptibilities between 4500-72000 χ_m x10^{-6} cm^3 mol^{-1} and different water solubility are compared for

their droplet-based magnetowetting behaviour, sliding angle and adhesion force. Solution susceptibility of each salt is measured for the concentration range used. Maximum actuation speed and droplet disengagement is probed at different concentrations. A facile and rapid droplet-based doxorubicin assay is conducted by actuating paramagnetic salt containing droplets through an excitation sources (532 nm laser) and measuring fluorescence intensity.

5.2 Methods and Materials

5.2.1 Materials

Glass microscope slides (Fisher Scientific, 76 x 25 x 1.0 mm) were used as device substrates. Ultra-Ever Dry® (UED), purchased from Hazmasters (Ottawa, Canada) as a two-part coating, a base adhesive coat and a top coat, which contained the fluorinated silica nanoparticles was used to prepare a super hydrophobic coating. Two NdFeB magnets (K&J Magnetics, Inc., PA) were used in this experiment – a flat disk used for contact angle and roll off angle measurements (1.8 mm x 0.7 mm, ~ 2.1 kG), and a small cylindrical magnet used for droplet manipulation and velocity measurements (1.1 mm x 1.1 mm, ~ 1.8 kG). The field strength of each of the magnets was measured by placing a glass slide on each of the magnets and placing the probe (Gaussmeter Model 410, LakeShore Cryotronics Inc., Westerville, OH) on the glass slide. Salts with different magnetic susceptibilities were obtained as follows: $MnCl_2 \cdot 4H_2O$ (Fisher Scientific, NJ, USA), $FeCl_3 \cdot 6H_2O$ (Sigma Aldrich, MO, USA), $EuCl_3 \cdot 6H_2O$ (Sigma Aldrich, WI, USA), $Er_2(SO_4)_3 \cdot 8H_2O$ (Alfa Aesar, MA, USA) and $GdCl_3$ (Sigma Aldrich, MO, USA). These salts were mixed with deionized water (Fisher Scientific, Ottawa, Canada) and used to prepare dilutions of various concentrations.

5.2.2 Magnetic Susceptibility Measurement

Mass and molar magnetic susceptibility (χ_g and χ_m respectively) of the pure salts and their solutions (χ_s) at various concentrations was measured using a Gouy balance (Magnetic Susceptibility

Balance, Johnson Matthey, Wayne, PA, USA). Mass magnetic susceptibility can be directly obtained

from the instrument, using the eqn. 5.3:

$$\chi_g = \frac{C_{bal} \cdot l \cdot R_{sample}}{10^9 \cdot m}$$ *Equation 5.3*

where C_{bal} is the calibration constant of the balance, l is the length of the salt sample in

centimetres, R_{sample} is the instrument reading and m is the mass of the sample.

Magnetic susceptibility of the salt solutions at various concentrations was obtained using eqn.

5.4:

$$\chi_s = \frac{m_s}{m_s + m_w} \chi_g + \frac{m_w}{m_s + m_w} \chi_w$$ *Equation 5.4*

where χ_w is mass magnetic susceptibility of water ($-0.72 \cdot 10^{-6}$ cm^3 g^{-1}), m_s is the mass of salt

and m_w is the mass of water.[28]

Table 5.1 gives a summary of important properties of the salts used.

Table 5.1: Paramagnetic salts and their relevant physical properties (listed in order of increasing magnetic susceptibility).

Paramagnetic Salt	Measured Magnetic Susceptibility, χ_mx10^{-6}cm^3 mol^{-1}	Literature Magnetic Susceptibility,[29] χ_mx10^{-6}cm^3 mol^{-1}	Concentration range explored, M	Solubility, g/100g of H$_2$O	Molar mass, g/mol
EuCl$_3$·6H$_2$O	4370±30	NA	0.8 – 3.0	Soluble*	366.42
MnCl$_2$·4H$_2$O	13250±280	14600	0.3 – 3.0	77.3	197.91
FeCl$_3$·6H$_2$O	12780±375	15250	0.3 – 3.0	91.2	270.30
GdCl$_3$	23320±160	27930	0.2 – 3.0	Soluble*	263.61
Er$_2$(SO$_4$)$_3$·8H$_2$O	73100±2000	74600	0.05 – 0.67	16	766.82

*Soluble to at least 3 M, the maximum concentration studied.

5.2.3 Superhydrophobic Surface Preparation

Both base and top coats of UED were applied according to manufacturer specifications with a

thin-layer chromatography sprayer. The base coat was sprayed twice over a clean glass slide surface

and air dried in a fume hood for 20 minutes at ambient temperature. Similarly, two layers of the top

coat were then uniformly sprayed over the dried surface of the base coat and air dried in the fume hood

for at least two hours prior to challenging the surface. SEM image of the surface is presented in Fig. 5.1.
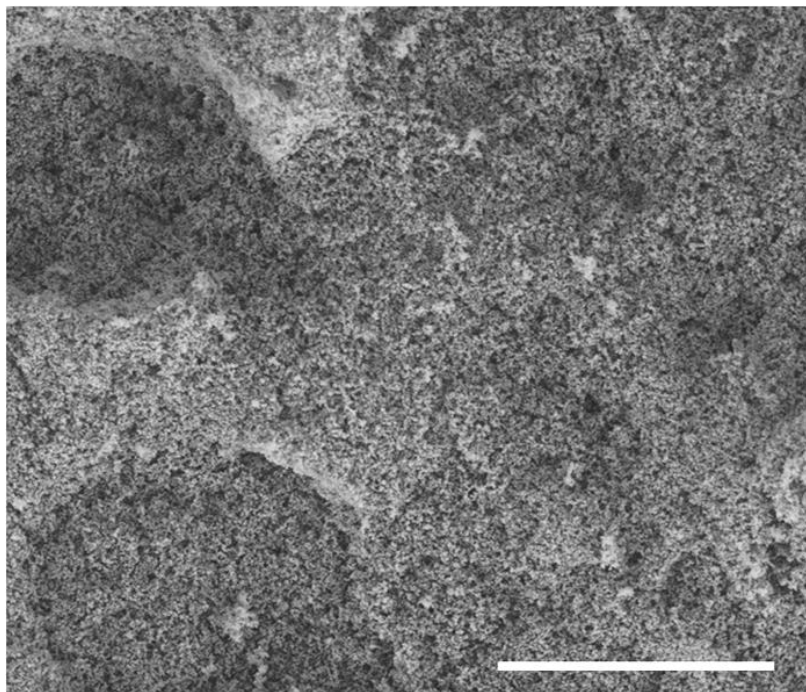
Figure 5.1: SEM photograph of UED surface on a glass slide, demonstrating roughness on micro- and nanoscale due to presence of fluorinated silica nanoparticles (scale bar = 10 μm).

5.2.4 Contact Angle, Roll-off Angle and Droplet Base Diameter Measurements

Contact angles were recorded using a microUSB microscope equipped with a camera (Veho X400, VMS-004D), and imageJ freeware with DropSnake plug-in was used to measure individual contact angles. The same camera and software were used to measure roll-off angles (ROA) and the droplet base diameters for droplets of various salt concentrations.

5.2.5 Droplet Actuation Velocity

A 30 mm distance was delineated on the underside of a glass slide having the UED coated on its top side. The average speed was determined by measuring the time it takes a 10 μL droplet to travel over the 30 mm distance using Microsoft® Windows™ Movie Maker to analyze videos recorded with a Veho USB microscope with millisecond precision. The minimum concentration used in the table refers to the lowest concentration that resulted in reproducible actuation for each salt, and the

maximum concentration refers to the highest concentration tested (values from Table 5.1). Magnet disengagement speed was measured as the speed at which the droplet could not repeatedly follow the motion of the magnet i.e. if the magnet was suddenly stopped, the droplet would disengage from the magnet due to excessive inertia.

5.2.6 Fluorescence Measurements

Doxorubicin hydrochloride (DOX) (Sigma Aldrich, MO, US) was prepared as a stock solution of 10 mM in water. Further dilutions were prepared, where for the control calibration solution, stock solution was diluted in 90% H_2O/ 10% MeOH to give concentrations ranging from 1.3 μM (0.75 μg/mL) to 53.3 μM (30.9 μg/mL). The same concentrations of DOX were prepared in the 0.3 and 0.5 M solution of $MnCl_2 \cdot 4H_2O$ in 90% H_2O/ 10% MeOH. Detection was conducted online, where individual droplets were excited by a green diode laser (Wicked Lasers, Hong Kong) @ 532 nm with 5 mW power. Fluorescence emission spectra were recorded using a custom CCD-based Ocean Optics USB 2000+ spectrometer (FL, USA) with the range of 350 to 1000 nm and resolution of about 1.5 nm. The excitation laser was positioned parallel to the substrate while the collection fibre was positioned perpendicular to droplet movement (i.e. 90° to excitation) to minimize excitation scatter. A schematic drawing and a photograph of the set-up is presented in Fig. 5.2.
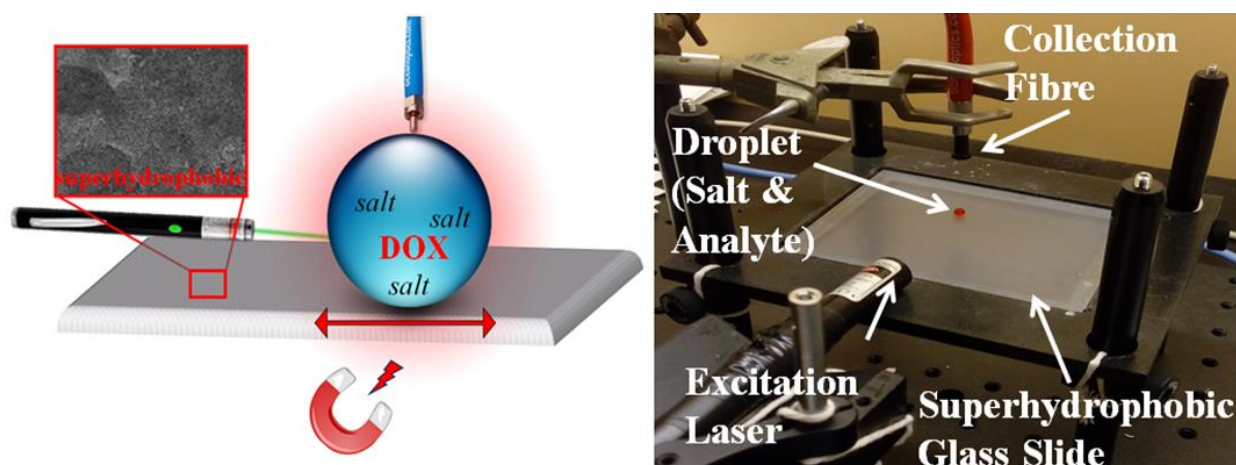
Figure 5.2: Online fluorescence measurement of droplets containing DOX and paramagnetic salt on the superhydrophobic glass slide.

Another series of solutions was prepared to test the effect of increasing salt concentration on the fluorescence of bulk DOX solution of constant concentration (10 μM diluted in 90 % H_2O/ 10% MeOH). 10 μM DOX was introduced in $MnCl_2 \cdot 4H_2O$ solutions (90 % H_2O/ 10% MeOH) with the concentrations ranging from 0.3 to 3.0 M. The change in fluorescence intensity was measured on a Varian Cary Eclipse spectrometer with 532 nm excitation (5 nm slit width) and emission maximum at 592 nm.

To evaluate online fluorescence, a control series of droplets containing varying concentrations of DOX with no salt added, were positioned over a marked hydrophilic spot on the UED surface (i.e. pinning point) to prevent their spontaneous roll-off. Otherwise, the droplets containing both salt and DOX were dispensed over a magnet anywhere on the UED surface and then were actuated by the magnet to a desired location directly under the detection fibre and perpendicular to the excitation laser. The position of the salt-containing droplets can be precisely controlled by a magnet and each dispensed droplet was positioned under the collection fibre until the emission maximum was achieved. It was crucial to control the droplet to ensure reproducible excitation and emission of each droplet. For both the control series and the salt series the position at which the reading was taken was first optimized to produce maximum emission.

5.3 Results and Discussion

5.3.1 Paramagnetic Salt Concentration and Roll-off Angle

Equation 5.1 suggests that three factors are affecting the actuation of droplets containing paramagnetic salts: magnetic field strength, magnetic susceptibility of the salt and the concentration of the salt within the droplet. In this study the magnetic field strength was maintained at 1.8 kG and salt concentration was varied within solubility limits. Fig. 5.3(top) shows the magnetic susceptibility values for different paramagnetic salts at a number of concentrations. Magnetic susceptibility was calculated from an experimentally determined χ_m and Equation 5.4. Salts with higher molar magnetic susceptibility produce a more marked increase in solution magnetic susceptibility with increasing

concentration. The upper range of concentrations is ultimately limited by the solubility of the salt. Four of the salts (Mn, Fe, Gd and Eu) are soluble to at least 3.0 M. The erbium salt, $Er_2(SO_4)_3 \cdot 8H_2O$, was much less soluble and so was studied to a maximum concentration of 0.67 M (Table 1). Even at this relatively low concentration, the solubility of the salt was exceeded and non-dissolved salt was present, similar to droplet containing superparamagnetic particles but with much lower value of χ_m.

The minimum concentration at which a droplet containing a dissolved salt can be reproducibly actuated was examined. Droplets (10 µL) containing different concentrations of salt were actuated over the fluorinated silica nanoparticle coated surface using a 1.8 kG cylindrical magnet. Reproducible actuation is characterized as the droplet being engaged by the magnet and linearly actuated with 100% success (n=10). In general, salts with a larger χ_m could be actuated at a lower concentration. Both $MnCl_2$ and $FeCl_3$ have a very similar magnetic susceptibility values, 13250 and 12780 $x10^{-6}$ cm^3 mol^{-1} respectively. These salts required a concentration of at least 0.3 M to reproducibly actuate 10 µL droplets. Salts with higher magnetic susceptibility, i.e. $GdCl_3$ (23320 $x10^{-6}$ cm^3 mol^{-1}) and $Er_2(SO_4)_3$ (73100 $x10^{-6}$ cm^3 mol^{-1}) require a lower concentration of 0.2 M and 0.05 M respectively for reproducible actuation. The salt with the lowest magnetic susceptibility, $EuCl_3$ (4370 $x10^{-6}$ cm^3 mol^{-1}) required at least 0.8 M solution for reproducible movement. Overall, the most suitable choice of salt for a given application is determined by the solubility of the salt in the droplet medium, magnetic susceptibility of the paramagnetic salt and the cost/gram of the paramagnetic material. Given these considerations, Mn or Fe would be preferable, however analyte compatibility may dictate an alternate choice. On the other hand, certain applications/reagents might benefit from using lower salt concentrations; in this case erbium salt would perform better. The region of Fig. 5.3 (top) highlighted with a framed black box is expanded in Fig. 5.3 (bottom) to more clearly show the solutions with small magnetic solution susceptibilities. If we examine the minimum concentrations for actuation in terms of their magnetic susceptibilities we can identify the minimum solution susceptibility required for droplet actuation. The division line in between the red and green regions in Fig. 5.3 (bottom)

designates the cut-off for reproducible actuation, where all solution compositions to the right are reproducibly actuated (green shading) while those to the left were not (red shading). For our experimental magnetic field strength and superhydrophobic surface this translates into a value of $\chi_s \approx 2.0 \times 10^{-6}$. For the surfaces with lower adhesion this line would be shifted to the left, i.e. it should be possible to actuate droplets with lower magnetic susceptibility. The surfaces with higher adhesion would shift it to the right, i.e. require higher droplet magnetic susceptibility for successful actuation.
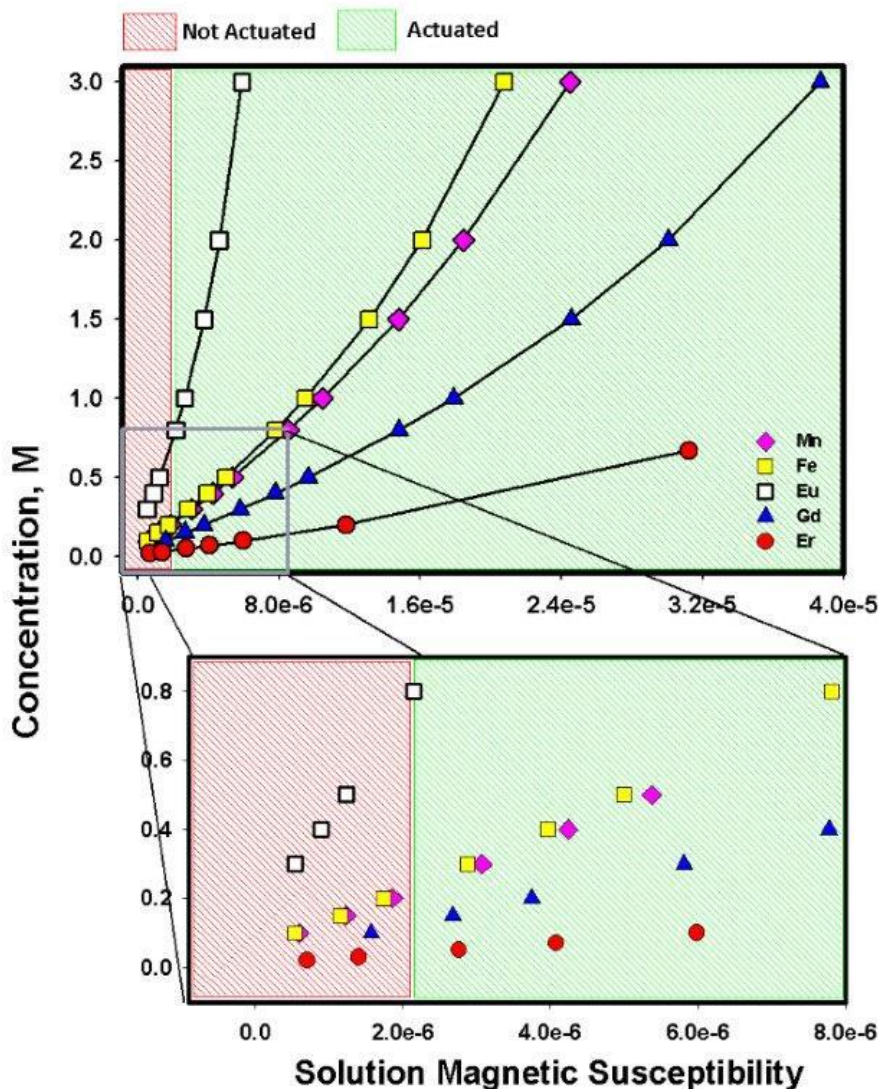
Figure 5.3: (top) The solution magnetic susceptibility (χ_s) of paramagnetic salt solutions at different concentrations tested for magnetic actuation; (bottom) shows an expanded view of a region of Figure 5.3(top) that illustrates the solution magnetic susceptibility cut-off (i.e. left of the line has no reproducible actuation) for 10 µL droplets on a fluorinated silica nanoparticle surface.

147

Superhydrophobic surfaces are characterized by high contact angle and low friction/adhesion[30] where forces as low as micro Newtons are required to actuate a droplet across a surface. Fig. 5.4 demonstrates the high CA between the UED surface and the droplet of manganese salt.
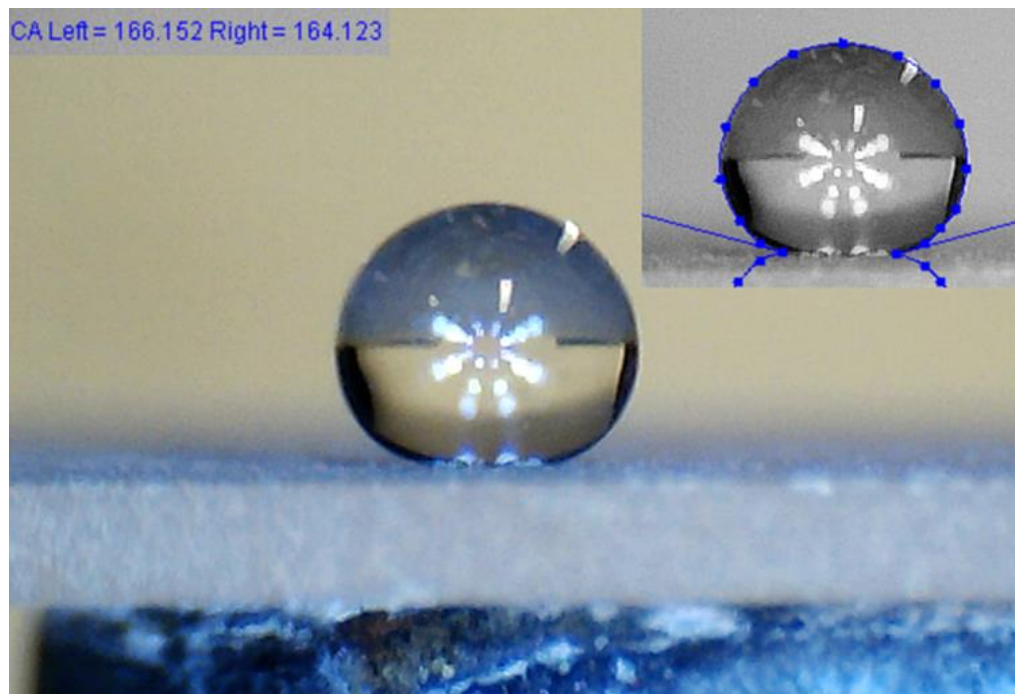
Figure 5.4: A 10 µL droplet of 0.3 M MnCl$_2$·4H$_2$O salt over superhydrophobic UED surface held by a magnet, where contact angle is ~ 165°. The insert shows the measurement from the imageJ software.

The force (F_a) that must be overcome to enable actuation can be estimated by the roll-off/sliding angle of a droplet on a surface in the absence of a magnetic field (i.e. 0.6°+/-0.2 corresponding to a $\overrightarrow{F_a}$ ~ 900 nN).[17] Under an applied magnetic field, droplets containing superparamagnetic particles or salts have a higher ROA, due to the magnetic force generated between the particles within the droplet (superparamagnetic particle based) or solvated metal ions (paramagnetic salt based) and the magnet. Fig. 5.5 shows the ROAs for a 10 µL aqueous droplet with increasing concentration of different paramagnetic salts in the presence of a constant magnetic field (Table 5.2 A, B). The angle at which the droplet rolls off the surface is determined by a combination of the frictional force and the magnetic force applied (total adhesion force, $\overrightarrow{F_a}$) to the droplet:

$$\vec{F_a} = m \cdot g \cdot sin\Theta = (\vec{F_m}) + \vec{F_f} \qquad\qquad Equation\ 5.5$$

where m is the mass of the droplet, g is standard acceleration due to gravity and Θ (in radians) is the roll-off angle. This assumption neglects changes to $\vec{F_f}$ due to magnetowetting (*vide infra*) however it serves as a guide to the relative forces (Table 5.2 A, B) involved with the dissolved salts and magnetic field for the concentrations studied.

As one would expect, larger ROAs are exhibited for salts (at equal concentration) with greater magnetic susceptibility (χ_m) and the ROA increases as the magnetic solution susceptibility of the salt solution (χ_s) increases. In this way the magnetic force ($\vec{F_m}$) exerted on a droplet can be controlled through either the choice of salt or its concentration. Fig. 5.5 indicates that the roll off angle and the corresponding force increase with the increasing concentration and magnetic susceptibility of the salt, as dictated by eqn. 5.1.
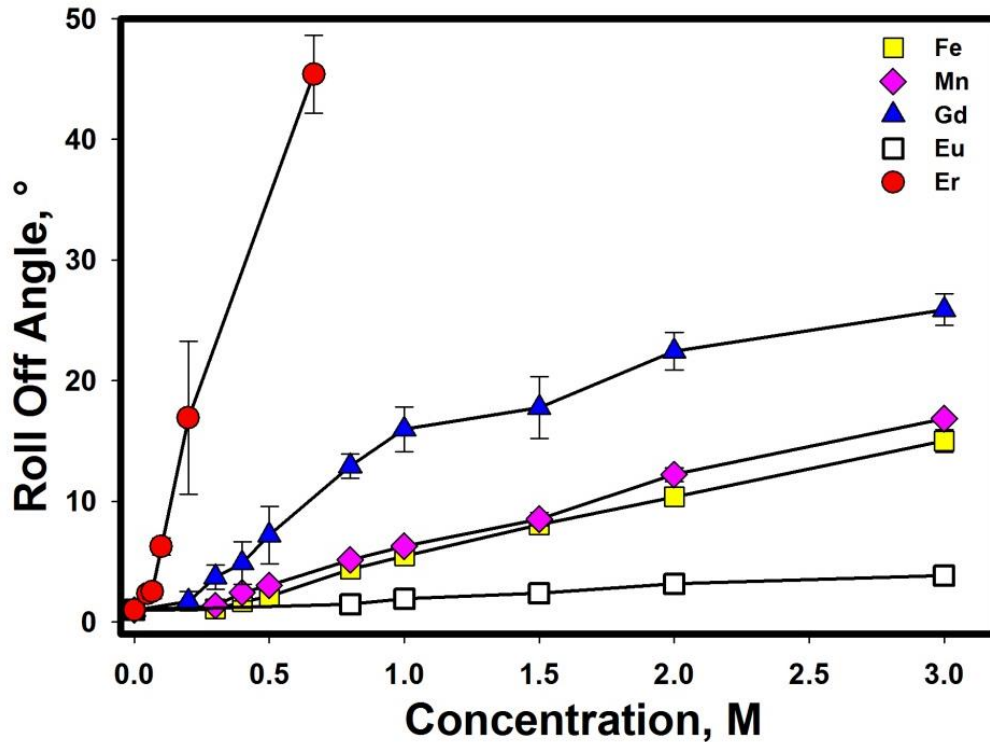

Figure 5.5: Roll-off angles of 10 μL droplets containing different concentrations of paramagnetic salt on a commercial superhydrophobic coating. Error was calculated as an RSD value of 3 measurements.

The upper range of concentrations is ultimately limited by the solubility of the salt; whereas the lower limit is dictated by whether the 10 µL droplet at particular concentration can be actuated. Salts of Mn, Fe, Gd and Eu are soluble to at least 3.0 M, and their roll-off angle/force data is summarized in Table 5.2A. The erbium salt, $Er_2(SO_4)_3 \cdot 8H_2O$, was much less soluble and so was studied to a maximum concentration of 0.67 M which already exceeds its solubility in deionized water (Table 5.2B).

Table 5.2A: Roll-off angle and corresponding $\overrightarrow{F_a}$ for a 10 µL droplet with different concentrations of paramagnetic salts under an applied magnetic field (~ 2.1 kG).

Concentration, (M)	$MnCl_2 \cdot 4H_2O$, ($°/\mu N$)	$FeCl_3 \cdot 6H_2O$, ($°/\mu N$)	$GdCl_3$, ($°/\mu N$)	$EuCl_3 \cdot 6H_2O$, ($°/\mu N$)
0.00	0.6±0.2/ 1.0±0.3			
0.20	CBAL	CBAL	1.7±0.8/ 3.1±1.4	CBAL
0.30	1.3±0.1/ 2.4±0.1	1.0±0.3/ 1.9±0.5	3.7±1.0/ 7.1±1.8	CBAL
0.40	2.4±0.7/ 4.4±1.3	1.6±0.3/ 3.0±0.6	4.9±1.7/ 9.0±3.2	CBAL
0.50	3.0±0.1/ 5.6±0.2	2.1±0.4/ 4.1±0.8	7.2±2.4/ 13.8±4.6	CBAL
0.80	5.1±0.1/ 10.2±0.2	4.4±0.3/ 9.0±0.6	12.9±1.0/ 26.5±2.1	1.4±0.1/ 3.2±0.3
1.00	6.3±0.3/ 12.8±0.6	5.4±0.1/ 11.8±0.3	15.9±1.8/ 34.0±4.0	1.9±0.2/ 4.5±0.4
1.50	8.5±0.5/ 18.8±1.2	8.0±0.4/ 19.3±0.9	17.8±2.6/ 41.7±6.1	2.4±0.6/ 6.2±1.5
2.00	12.2±0.6/ 28.9±1.4	10.3±0.3/ 27.1±0.8	22.4±1.6/ 57.0±4.1	3.1±0.3/ 9.3±0.8
3.00	16.8±0.1/ 45.2±0.4	15.0±1.0/ 45.9±3.0	25.9±1.3/ 76.5±4.0	3.8±0.4/ 13.7±1.4

*CBAL (concentration below actuation limit)-reproducible actuation not possible for this salt at this concentration

Table 5.2B: Roll-off angle and corresponding $\overrightarrow{F_a}$ for a 10 µL droplet with different concentrations of $Er_2(SO_4)_3 \cdot 8H_2O$ under an applied magnetic field (~ 2.1 kG).

Concentration, (M)	$Er_2(SO_4)_3 \cdot 8H_2O$, ($°/\mu N$)
0.00	0.6±0.2/ 1.0±0.3
0.05	2.3±0.6/ 4.1±1.1
0.07	2.5±0.6/ 4.5±1.0
0.10	6.2±0.7/ 11.5±1.3
0.20	16.9±6.3/ 32.8±12.4
0.67	45.4±3.2/105.2±8.3

Although the minimum force to actuate a droplet over a superhydrophobic surface can be approximated to be 1 μN (i.e. ROA in absence of magnetic field), in practice larger magnetic forces are required to overcome an increased adhesive force due to magnetowetting and to exhibit reproducible droplet actuation (~2 μN).

Equation 1 demonstrates a dependence of the magnetic force on the solution magnetic susceptibility, where an increase in solution magnetic susceptibility leads to an increase in force. In this case there is a direct correlation for totally dissolved salts (i.e. Eu, Mn, Fe and Gd) when the values of F_a are plotted against the solution magnetic susceptibility (Fig. 5.6). The exception is again the less soluble $Er_2(SO_4)_3 \cdot 8H_2O$, which due to the insoluble paramagnetic material being concentrated at the bottom of the droplet (i.e. nearer the magnet) results in a higher force at similar concentration. The linearity of the relationship is increased if the droplets containing large amounts of non-dissolved material (Er salt droplets) are excluded, i.e. R^2 value increases from 0.85 to 0.96.
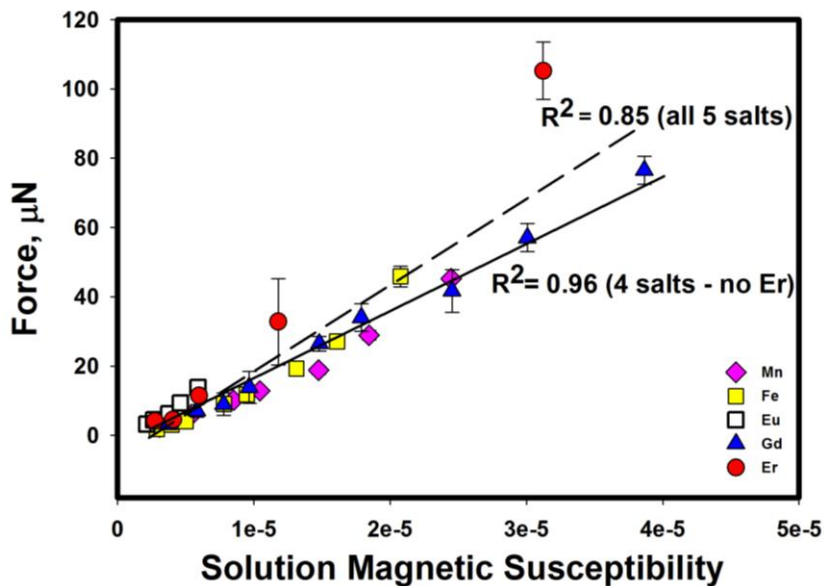

Figure 5.6: The relationship between the F_a and the solution magnetic susceptibility. A co-linear relationship is observed for all the combinations of magnetic susceptibility and the force for each of the soluble salts (i.e. Eu, Mn, Fe and Gd). Error was calculated as an RSD value of 3 measurements.

5.3.2 Magnetowetting Measurement of Droplets Containing Paramagnetic Salts

The application of a magnetic field to droplets impacts the shape and the droplet/surface contact area. The so-called magnetowetting is a phenomenon where droplet shape elongates along the magnetic field direction.[19] A description of this phenomenon has been previously discussed in detail by Nguyen et al., for ferrofluids where overall higher magnetization (i.e. high field strength, larger magnetic susceptibility and/or higher concentration) leads to a larger droplet deformation.[31,32] In applications where large superparamagnetic particles (> 1 μm) are utilized for droplet actuation the particles are pulled to the bottom of the droplet upon the application of the magnetic field. In these cases droplet deformation is reduced as the magnetized material is isolated at the base of the droplet.[17] In cases where the paramagnetic material is suspended or dissolved within the droplet, deformation can be more pronounced as the entire droplet interacts more strongly with the magnet. A series of experiments were conducted that examined the extent of magnetowetting for 10 μL aqueous droplets with different paramagnetic salt concentration. An example is shown in Fig. 5.7 and where a droplet containing two different concentrations of $GdCl_3$ (left) 0.2 M corresponding to the minimum concentration for reproducible actuation and (right) 3.0 M corresponding to the maximum concentration tested (same magnetic field applied). In this case the base of the droplet in contact with the surface is elongated 60% from ~922±16 μm to ~1470±10 μm, corresponding to a ~ 254% increase in contact area from (6.67 ± 0.07) x 10^5 μm^2 to (16.97 ± 0.07) x 10^5 μm^2 due to magnetowetting (assuming symmetrical elongation in x and y).
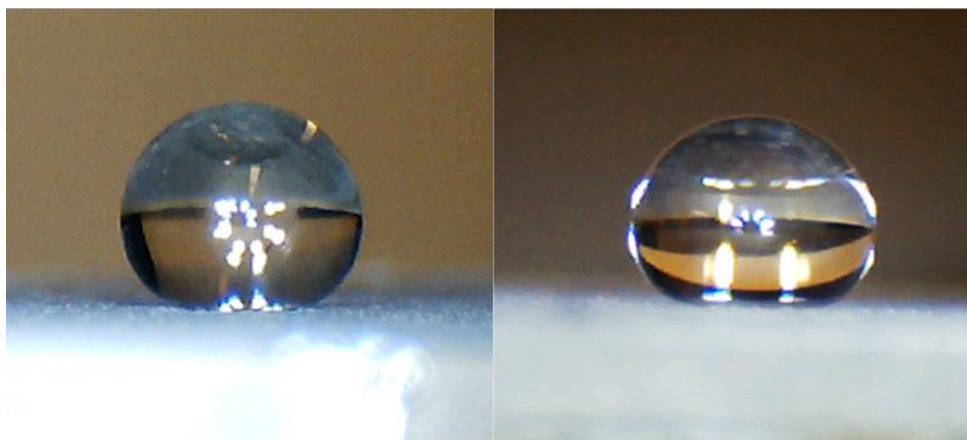
Figure 5.7: An increase in contact area of a 10 µL aqueous droplet containing GdCl₃ salt (left) 0.2 M and (right) 3 M with the same applied magnetic field (2.1 kG) on a superhydrophobic coating.

Magnetowetting is observed for all salts tested, and an increase in concentration leads to more significant droplet elongation and in the increase of droplet-surface contact area. Figure 5.8 shows the trend where larger molar magnetic susceptibility of the salt and increasing concentrations result in droplet base diameter elongation, i.e. higher magnetowetting.
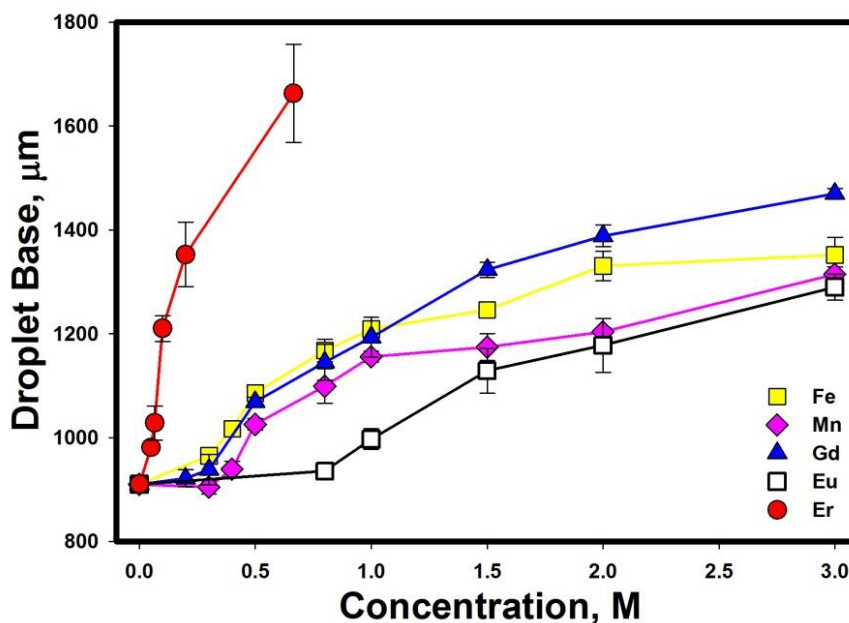
Figure 5.8: Magnetowetting of 10 µL droplets containing increasing concentrations of paramagnetic salt on a commercial superhydrophobic coating as measured by an increase in the droplet/water contact length. Error was calculated as an RSD value of 3 measurements.

153

5.3.3 Velocity of Paramagnetic Salt Containing Droplets

Most reports that have employed magnetic droplet actuation have utilized droplets covered with an oil layer to further reduce surface friction.[33] However low roll-off angles attributed to superhydrophobic surfaces allow for the droplets to be easily actuated in an oil-free open format (i.e. no need for an oil layer covering the droplet).[20,34] Although the effects of evaporation are exacerbated in an oil-free format, higher actuation speeds can be obtained which may be beneficial for applications where rapid droplet movement can significantly increase sample throughput.[18] Three distinct regimes have been demonstrated for particle-based magnetic droplet actuation i.e. steady movement, magnet disengagement and particle removal.[18,35] Particle removal is not observed for droplets containing paramagnetic salts below their solubility limit. Undissolved material is present within the droplet for less soluble salts at concentrations exceeding their solubility limits ($Er_2(SO_4)_3 \cdot 8H_2O$ above 0.1 M). Nevertheless, particle removal is never observed due possibly to the force being applied to both the undissolved and dissolved salt within the droplet. This is contrary to observations using droplets containing superparamagnetic particles where compact bead-clusters formed at the droplet-air (or droplet-oil) interface results in the removal of the bead-cluster. In general, increased salt concentration results in both a higher average and disengagement velocity (Table 5.3), where the highest velocities obtained were for those salts that are readily soluble and possess higher solution magnetic susceptibility.

Table 5.3: Droplet actuation velocity for various salts in a 10 µL droplet. Average velocity refers to reproducible actuation speed, where no magnet disengagement occurred (i.e. 100% actuation n=10).

Paramagnetic Salt	Mean Velocity, mm/s Maximum Conc.	Droplet Disengagement Speed, mm/s	
		Minimum Conc. with Reproducible Actuation	Maximum Conc.
$MnCl_2 \cdot 4H_2O$	111±21	53±4	169±27
$FeCl_3 \cdot 6H_2O$	114±19	51±8	150±17
$GdCl_3$	130±12	63±4	182±8
$EuCl_3 \cdot 6H_2O$	62±7	58±3	88±6
$Er_2(SO_4)_3 \cdot 8H_2O$	118±22	119±37	ND*

* Disengagement was not measured as droplet movement was not possible from undissolved material becoming trapped in the surface structure.

154

The average velocity at maximum concentration is dependent on the salt identity, where salts with higher magnetic susceptibility can achieve higher average velocity. This is consistent with the adhesion force data in Table 5.2A & B and the solution magnetic susceptibility of each salt droplet in Fig. 5.3.

Magnet disengagement speed at minimum concentration is also consistent with the solution magnetic susceptibility, where all salts except $Er_2(SO_4)_3 \cdot 8H_2O$ disengage from the magnet above 50-60 mm/s. $Er_2(SO_4)_3 \cdot 8H_2O$, the salt with the highest magnetic susceptibility, shows somewhat unexpected behaviour, where the droplet motion at higher concentration was not smooth, and the droplet often became "trapped" while being translated over the surface. In this case the significant non-dissolved materials became trapped in the surface structure of the silica nanoparticle coating which impeded droplet movement. This effect became more pronounced with increasing $Er_2(SO_4)_3 \cdot 8H_2O$ salt concentration. Furthermore the magnet disengagement speed could not be measured at higher concentrations, as the droplet would become trapped in the surface, and stop moving. Solubility of the specific salts could be potentially enhanced by altering solution conditions (i.e. pH, temperature etc.) but were beyond the scope if this study.

5.3.4 Droplet-based Fluorescence Measurement with Paramagnetic Salt Actuation

Photoluminescence is a powerful detection method for the selective and sensitive determination of fluorescent analytes. Photoluminescence is one of most commonly employed detection strategies for both continuous and droplet-based microfluidic analysis due to its high sensitivity, low sample requirement, and relative simplicity.[36] As an example application of particle-free droplet actuation, we performed a droplet-based assay for a common cancer drug doxorubicin (DOX). Doxorubicin belongs to the group of anthracycline antibiotics with very effective anticancer properties. Manganese chloride was chosen as the actuation salt due to solubility and cost factors. To evaluate the droplet fluorescence, a control series of droplets containing varying concentrations of DOX but not the salt, were positioned over a marked hydrophilic spot on the UED surface. The

155

hydrophilic spot was necessary to pin droplet without which the salt free droplet would simply roll away from the detection region. Alternatively the droplets containing both salt (either 0.3 or 0.5 M) and DOX were dispensed over a magnet at another location on the substrate and actuated by the magnet to the desired optimized location directly under the detection fibre. For the control series the droplet was always in the same pre-optimized position on the hydrophilic spot, while for the salt-containing droplets the magnet was used to optimize the position of each droplet. Individual droplets were excited by a green laser (532 nm) positioned parallel to the substrate, and fluorescence was collected by a fibre positioned perpendicular to droplet movement (i.e. 90° to excitation) to minimize excitation scatter. Fig. 5.9 presents the fluorescence signal for the DOX in water/methanol mixtures with or without added salt of $MnCl_2 \cdot 4H_2O$.
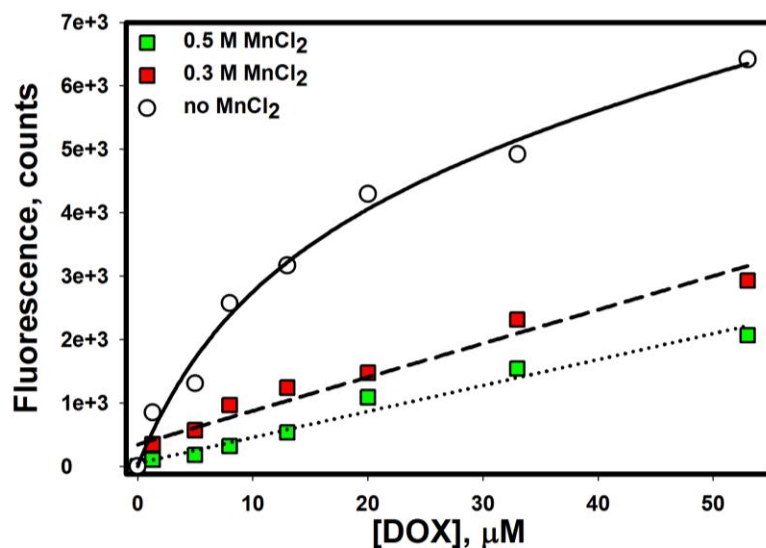
Figure 5.9: Fluorescence signal for different concentrations of DOX in solution of 20 μL water/methanol droplet without (○) and with 0.3M (■) or 0.5 M (■) $MnCl_2 \cdot 4H_2O$ salt.

The fluorescence signal intensity is significantly higher for the droplets with no salt added. It has been previously demonstrated that the fluorescence of DOX can be very complex, where both solution composition and DOX concentrations affect the fluorescence intensity and response tends to be non-linear at DOX concentrations above 15 μg/mL.[37] The linearity is significantly improved for the salt containing solutions, where high linear correlation (R^2=0.9551 for 0.3 M and R^2=0.9741 for 0.5 M vs R^2=0.8962 for the "control" series) is observed at concentrations up to 53.3 μM (30.9 μg/mL),

while DOX in water/methanol (i.e. no salt) is no longer linear above 13.3 μM (7.7 μg/mL). The slope of the line also indicates that overall fluorescence signal is higher for the "control" solution, while added salt decreases the signal. The fluorescence response of DOX with 0.3 M salt added is reduced to 0.47 of the initial value, while 0.5 M salt further reduces fluorescence to 0.36 of the initial intensity. The addition of salts can cause fluorescence quenching, which refers to non-radiative intermolecular energy transfer from the excited fluorogenic species to other molecules. The specifics of the quenching process is beyond the scope of this thesis, however halide anions (i.e. Cl⁻) are known for their collisional quenching properties,[38] while paramagnetic cations have been also demonstrated to induce quenching through multiple mechanisms.[39] The extent of the fluorescence signal decrease due to quenching was probed separately offline with a Varian Cary spectrometer, where bulk solutions were prepared with a constant concentration of DOX (10 μM) and increasing concentrations of manganese salt. The resulting fluorescence signal intensities for salt concentrations ranging from 0-3.0 M are presented in Fig. 5.10. The fluorescence intensity decreases with increasing $MnCl_2$ concentration and the emission maximum (λ_{max}) is red shifted.

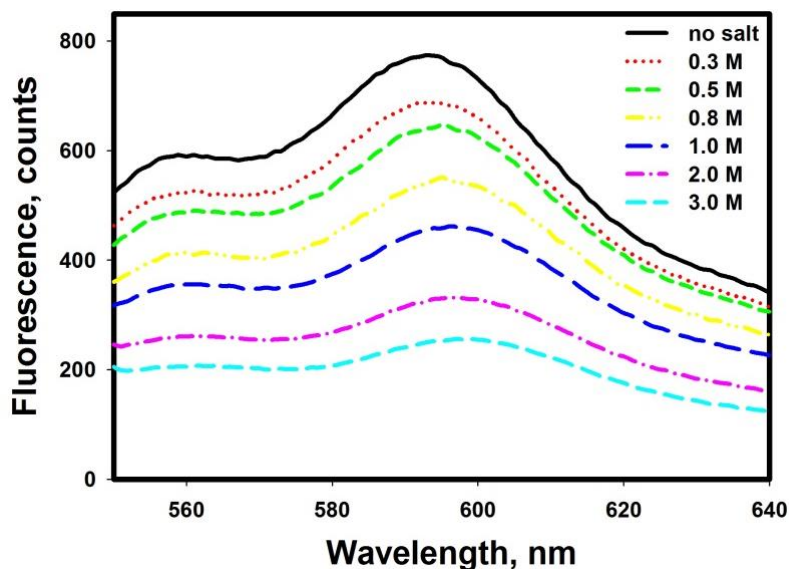**Figure 5.10: The decrease in the DOX (10 μM) fluorescence intensity observed at higher concentrations of $MnCl_2$ in water/methanol solutions @ 532 nm excitation wavelength. At higher salt concentrations the maximum emission wavelength shifts to longer wavelength (red shift), i.e. "blank" solution with no salt added λ_{max} is at ~ 592 nm, while 3.0 M salt solution λ_{max} is at ~ 599 nm.**

DOX is known to be susceptible to quenching, where Stern-Volmer quenching constant can be determined to evaluate the extent of quenching.[40] The Stern-Volmer constant of the MnCl$_2$ salt was found to be ~0.71 M^{-1} (R^2=0.994) is presented in Fig. 5.11. Overall, particle free, paramagnetic salt actuation is compatible with fluorescence-based detection however analyte and fluorophore compatibility need be ascertained.
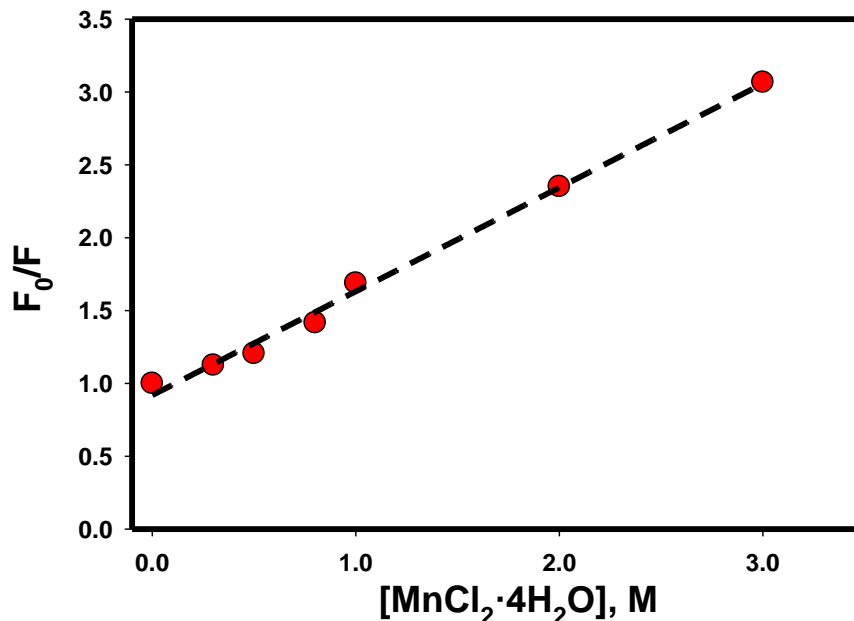
Figure 5.11: The Stern-Volmer quenching constant of the MnCl$_2$ salt determined in bulk solution with Varian Cary spectrometer (@ 592 nm excitation).

5.4 Conclusion

A novel "particle-free" actuation method for magnetic actuation was explored. Droplets of solutions of paramagnetic salts can be actuated by permanent magnets over a superhydrophobic surface. Solutions of five salts (i.e. MnCl$_2$·4H$_2$O, FeCl$_3$·6H$_2$O, GdCl$_3$, EuCl$_3$·6H$_2$O and Er$_2$(SO$_4$)$_3$·8H$_2$O) with magnetic susceptibility (χ_m) ranging from 4 370-73 100 x10^{-6} cm^3 mol^{-1} were successfully employed in magnetic actuation. Salts with lower magnetic susceptibility required higher concentrations to be efficiently actuated and droplets with solution susceptibilities of > 2x10^{-6} could be actuated. The magnetic force exerted on the droplet was determined using roll-off angles and it was determined that a force of ≈ 2 μN is required to actuate a 10 μL droplet on a fluorinated silica

nanoparticle surface. Actuation and disengagement velocity was determined for each salt with average velocities as high 130 mm/sec and disengagement velocities of 180 mm/sec for GdCl$_3$. Interestingly, the less soluble Er$_2$(SO$_4$)$_3$·8H$_2$O salt, demonstrated different actuation properties where it behaved similar to magnetic particle based systems and showed lower actuation velocity due to precipitated salt particles becoming trapped in the structure of the superhydrophobic surface. Online fluorescence detection combined with particle free actuation was used to detect DOX concentration in the droplet. A decrease in fluorescence intensity of DOX was observed with increasing concentration of the paramagnetic salt however the concentration curve showed an increase in linear dynamic range. Although salt induced fluorescence quenching was observed, there are several different paramagnetic salts that can be utilized and alternative detection methods employed that are more tolerant of the presence of paramagnetic salts.

5.5 References

1. F. Mugele and J.-C. Baret, *J. Phys.: Condens. Matter*, 2005, **17**, 705-74.

2. S. K. Cho, H. J. Moon and C. J. Kim, *J. Microelectromech. Syst.*, 2003, **12**, 70-80.

3. S. Ehlert and U. Tallarek, *Anal. Bioanal. Chem.*, 2007, **388**, 517-20.

4. P. Woias, *Sens. Actuat. B-Chem.*, 2005, **105**, 28-38.

5. M. Abdelgawad and A. R. Wheeler, *Microfluid. Nanofluid.*, 2007, **4**, 349-55.

6. A. Egatz-Gómez, S. Melle, A. A. García, S. A. Lindsay, M. Márquez, P. Domínguez-García, M. A. Rubio, S. T. Picraux, J. L. Taraci, T. Clement, D. Yang, M. A. Hayes and D. Gust, *Appl. Phys. Lett.*, 2006, **89**, 034106.

7. M. A. Gijs, F. Lacharme and U. Lehmann, *Chem. Rev.*, 2010, **110**, 1518-63.

8. J. R. Dorvee, M. J. Sailor and G. M. Miskelly, *Dalton Trans.*, 2008, **6**, 721-30.

9. R. Sista, Z. S. Hua, P. Thwar, A. Sudarsan, V. Srinivasan, A. Eckhardt, M. Pollack and V. Pamula, *Lab Chip*, 2008, **8**, 2091-104.

10. D. Kim, Q. Wei, J. E. Kong, A. Ozcan and D. Di Carlo, *Lab Chip*, 2015, **15**, 17-22.

11. N. S. Mei, B. Seale, A. H. C. Ng, A. R. Wheeler and R. Oleschuk, *Anal. Chem.*, 2014, **86**, 8466-72.

12. F. Saeki, J. Baum, H. Moon, J. Y. Yoon, C. J. Kim and R. L. Garrell, *Abstr. Pap. Am. Chem. S.*, 2001, **222**, 341-2.

13. D. Beyssen, L. Le Brizoual, O. Elmazria and P. Alnot, *Sens. Actuat. B-Chem.*, 2006, **118**, 380-5.

14. Y. J. Zhao, U. C. Yi and S. K. Cho, *J. Microelectromech. Syst.*, 2007, **16**, 1472-81.

15. U. Lehmann, S. Hadjidj, V. K. Parashar, C. Vandevyver, A. Rida and M. A. M. Gijs, *Sens. Actuat. B-Chem.*, 2006, **117**, 457-63.

16. E. Bormashenko, R. Pogreb, Y. Bormashenko, A. Musin and T. Stein, *Langmuir*, 2008, **24**, 12119-22.

17. L. Mats, R. Young, G. T. T. Gibson and R. D. Oleschuk, *Sens. Actuat. B-Chem.*, 2015, **220**, 5-12.

18. Z. Long, A. M. Shetty, M. J. Solomon and R. G. Larson, *Lab Chip*, 2009, **9**, 1567-75.

19. N. T. Nguyen, *Microfluid. Nanofluid.*, 2012, **12**, 1-16.

20. A. Egatz-Gomez, J. Schneider, P. Aella, D. Yang, P. Dominguez-Garcia, S. Lindsay, S. T. Picraux, M. A. Rubio, S. Melle, M. Marquez and A. A. Garcia, *Appl. Surf. Sci.*, 2007, **254**, 330-4.

21. Q. A. Pankhurst, N. T. K. Thanh, S. K. Jones and J. Dobson, *J. Phys. D: Appl. Phys.*, 2009, **42**, 224001.

22. L. Vekas, D. Bica and M. V. Adveev, *China Part.*, 2007, **5**, 43-9.

23. D. K. Bwambok, M. M. Thuo, M. B. Atkinson, K. A. Mirica, N. D. Shapiro and G. M. Whitesides, *Anal. Chem.*, 2013, **85**, 8442-7.

24. K. A. Mirica, S. S. Shevkoplyas, S. T. Phillips, M. Gupta and G. M. Whitesides, *J. Am. Chem. Soc.*, 2009, **131**, 10049-58.

25.   J. Zhu, L. Liang and X. Xuan, *Microfluid. Nanofluid.*, 2011, **12**, 65-73.

26.   A. I. Rodriguez-Villarreal, M. D. Tarn, L. A. Madden, J. B. Lutz, J. Greenman, J. Samitier and N. Pamme, *Lab Chip*, 2011, **11**, 1240-8.

27.   T. T. Zhu, R. Cheng and L. D. Mao, *Microfluid. Nanofluid.*, 2011, **11**, 695-701.

28.   J. Woolcock and A. Zafar, *J. Chem. Educ.*, 1992, **69**, 176-9.

29.   Lide, D. R., Ed. CRC Handbook of Chemistry and Physics, 89th ed. [Online]; CRC Press: Boca Raton, FL, 2008.

30.   M. Ma and R. M. Hill, *Curr. Opin. Colloid Interface Sci.*, 2006, **11**, 193-202.

31.   N. T. Nguyen, G. Zhu, Y. C. Chua, V. N. Phan and S. H. Tan, *Langmuir*, 2010, **26**, 12553-9.

32.   N. T. Nguyen, *Langmuir*, 2013, **29**, 13982-9.

33.   J. Pipper, M. Inoue, L. F. P. Ng, P. Neuzil, Y. Zhang and L. Novak, *Nat. Med.*, 2007, **13**, 1259-63.

34.   Z. J. Cheng, L. Feng and L. Jiang, *Adv. Funct. Mater.*, 2008, **18**, 3219-25.

35.   N. Vergauwe, S. Vermeir, J. B. Wacker, F. Ceyssens, M. Cornaglia, R. Puers, M. A. M. Gijs, J. Lammertyn and D. Wittersaabios, *Sens. Actuat. B-Chem.*, 2014, **196**, 282-91.

36.   L. Malic, D. Brassard, T. Veres and M. Tabrizian, *Lab Chip*, 2010, **10**, 418-31.

37.   P. Mohan and N. Rapoport, *Mol. Pharm.*, 2010, **7**, 1959-73.

38.   C. D. Geddes, *Meas. Sci. Technol.*, 2001, **12**, 53-88.

39.   A. W. Varnes, E. L. Wehry and R. B. Dodson, *J. Am. Chem. Soc.*, 1972, **94**, 946-50.

40.   F. Wang, Y. C. Wang, S. Dou, M. H. Xiong, T. M. Sun and J. Wang, *ACS Nano*, 2011, **5**, 3679-92.

Chapter 6

Conclusion and Outlook

6.1 Conclusions

This Ph.D. thesis explored the versatility and merits of the microfluidic field of research with respect to a variety of fluid manipulation methods and applications that can be adapted to the microscale. Two approaches, "continuous-flow" and digital microfluidics (DMF), were studied in detail and utilized to create LOC devices using polymer replication methods or photolithography respectively. Chapter 2 explored the more traditional "continuous flow" approach, where analytes are confined to narrow channels and are operated in bulk. Chapters 3, 4 and 5 provide detailed studies of an alternative DMF method, where discrete droplets of analyte (microlitre sized) can be individually addressed and controlled over hydrophobic and superhydrophobic surfaces. Specifically, Chapter 3 looked in detail at the electrowetting-on-dielectric (EWOD) actuation mechanism on natural, commercial and custom-tailored surfaces with varying degrees of hydrophobicity. Chapters 4 and 5 addressed magnetic actuation approach for DMF, where Chapter 4 explored particle-based actuation, while Chapter 5 introduced a novel "particle-free" approach.

A quick and simple fabrication technique for a cyclic olefin copolymer (COC) microchip based on hot embossing was developed in Chapter 2, where a microstructured fibre (MSF) had a dual role of a chromatography frit and an electrospray ionization mass spectrometry (ESI-MS) emitter. A COC microchip capable of sustaining up to 100 bar packing pressure was developed, where a combination of temperature and solvent bonding allowed for high robustness. The "continuous-flow" nature of this channel-based device was highly compatible with reverse-phase liquid chromatography (LC) and positive mode ESI-MS. Fast separation (under 10 min) of small drug molecules in isocratic mode and large proteins in gradient mode is demonstrated. The silica-based MSF emitter demonstrated robust and stable performance (RSD<5%) in positive ESI mode for all conditions tested, i.e. flow rates

from 10 to 500 nL/min, and various solvent phase compositions, including extreme conditions of 99% organic composition. A protocol for COC-microchip fabrication was implemented, where a robust device for various LC-ESI-MS analysis applications was fabricated.

DMF approaches have been introduced more recently, and have started gaining popularity in the past decade. Although a relatively new technique, a lot of fundamental research has been performed in this field, and optimization of basic parameters is presented on a regular basis. Chapter 3 explores the EWOD method on an open-top style device, where suitability of different surfaces for this approach is determined. Teflon ® AF (water contact angle (WCA) ~ 120°) was used as an industry standard, where it can be easily applied by spin coating and relatively small voltages are required (~ 200V) for droplet actuation. Teflon, however, suffers from robustness issues, where this thin coating (~ 100 nm) is often damaged after a few trials. A natural superhydrophobic material, *Colocasia* leaf (WCA>150), was demonstrated to be compatible with EWOD application method, however it required significantly higher voltages (often over 1 kV) and as natural material it is hard to handle due to drying. Customized and commercial fluorinated silica nanoparticle (FSNP) based surfaces were extensively tested for EWOD performance, where the deposition methods, surface characterization (with SEM), initial WCA and WCA change under applied voltage, compatibility with non-aqueous solvents and longevity were evaluated. Properties and performance ranged significantly depending on the nanoparticle size and degree of fluorination, where particles in range of 85 to 150 nm with fluorination of 75 or 90% "casted" over the substrate demonstrated highest WCA and WCA change as well as the lowest electrowetting voltage requirements. It was determined, however, that most superhydrophobic materials tend to operate in Wenzel wetting mode, where irreversible electrowetting was observed, which limits these materials applications in the microfluidics field.

Chapter 4 explored an alternative DMF actuation method, where a droplet containing magnetically susceptible particles is actuated by an external magnetic field over a (super)hydrophobic surface. Hydrophobic Teflon, superhydrophobic *Colocasia* leaf and a commercial FSNP-based

material (UltraEver Dry (UED)) were evaluated in terms of their suitability for magnetic actuation. Contact and roll-off angles were determined for each material for various combinations of droplet volume/particle concentrations; adhesion force and speed of actuation were also reported. Overall, Teflon, the least hydrophobic material proved to be least suitable for magnetic actuation due to high surface friction; high adhesion force associated with Teflon ($\sim$ 30 μN for 10 μL aqueous droplet) required high particle loading for actuation (>40 mg/mL), and the motion was often irregular. Superhydrophobic surfaces inherently possess much lower surface friction, where both *Colocasia* leaf and UED exhibited much lower adhesion force and produced reproducible actuation at low particle loading. *Colocasia*, however, due to natural surface roughness on the microscale, often exhibited particle entrapment which limited its suitability for magnetic actuation. UED proved to be the most suitable, where smooth motion was observed for large droplet sizes (up to 90 μL) and low particle loading (0.1 mg/mL). The surface was further characterized with SEM-EDX, which revealed that the top layer consisted of fluorinated silica nanoparticles (40~50 μm diameter), which create micro- and nano-structures, responsible for excellent superhydrophobic properties of UED. Surface stability was evaluated with a variety of non-aqueous solvents, and the feasibility of on-chip colorimetric titration was demonstrated. The peak speed of 550 mm/s was achieved for a 10 μL droplet.

The comparison study in Chapter 4 has determined that superhydrophobic surface (UED) is highly compatible with magnetic actuation, as it possesses very low adhesion force below 1 μN. It follows that even weak magnetic attraction could overcome surface adhesion, thus magnetic materials with low concentration or low magnetic susceptibility (χ_m) could be used. To our knowledge, Chapter 5 presented the first report of "particle-free" magnetic actuation, where paramagnetic salts were used as the magnetic entity to drive the aqueous droplet over the superhydrophobic surface. Five salts, $EuCl_3 \cdot 6H_2O$, $MnCl_2 \cdot 4H_2O$, $FeCl_3 \cdot 6H_2O$, $GdCl_3$ and $Er_2(SO_4)_3 \cdot 8H_2O$, with magnetic susceptibility (χ_m) values ranging from 4 370 to 73 100 $\times 10^{-6}$ cm^3 mol^{-1} were successfully employed in magnetic actuation. As expected, salts with lower χ_m required higher concentrations in order to be reproducibly

actuated; this trend was observed for other parameters studied, where higher χ_m resulted in higher magnetowetting, roll-off angles and speed. One notable exception was the speed analysis of $Er_2(SO_4)_3 \cdot 8H_2O$ salt, which due to very low solubility showed that the precipitated salt would often "interact" with the rough surface of UED, and high speeds could not be easily achieved. Chapter 5 also demonstrates feasibility of coupling salt actuation with online fluoresce detection of an anti-cancer drug doxorubicin, where a calibration curve was obtained. $MnCl_2 \cdot 4H_2O$ was used due to cost/solubility reasons, and even though quenching on DOX fluorescence was observed in the presence of the salt, linear response could be obtained over a concentration range of 1.3 to 53.3 μM for DOX.

6.2 Outlook and Future Work

The work outlined in this Ph.D. thesis presents several opportunities for further research. Firstly, as we report the first instance of "particle-free" salt actuation, many in-depth studies can now be conducted. We only looked at aqueous solutions of five salts, but it would be beneficial to look at the performance of non-aqueous droplets of the same salts, and probe additional paramagnetic salts (Ni, Co, other rare-earth elements) for their magnetic actuation performance. A larger range of droplet sizes should be explored, as well as mechanistic studies of the actuation process itself; to our knowledge, no comprehensive comparison between particle-based and particle-free approach has yet been reported.

Secondly, we explored a variety of natural and synthesis surfaces with varying hydrophobic/superhydrophobic properties; the utility of superhydrophobic surfaces for DMF applications is demonstrated beyond doubt. An interesting follow-up would be further modifying surface properties of the coatings, where controlled patterning could be achieved. The concept of hydrophilic patches was presented in Chapter 4 for the extraction of magnetic particles, however better control of hydrophobic/hydrophilic properties and size is required. As a suggestion, mechanical

surface patterning (i.e. laser micromachining) could be employed to create regions of increased hydrophilicity of controlled size/shape on an otherwise superhydrophobic surface.

Thirdly, many applications exploiting traditional in-channel microfluidics have yet to be widely adapted to the DMF format. Early reports of online in-droplet fluorescence detection was presented, however a much more systematic study can now be conducted. The digital format is not commonly employed for ESI-MS analysis due to the "flow" nature of this ionization method; however DMF can be compatible with discrete ionization approaches, such as MALDI or DESI. It would be beneficial to couple traditional "continuous flow" microfluidics techniques with DMF field. Both approaches have their advantages and drawbacks, and by combining the strengths of each technique, a better performing platform can be realized.